GPS-BASED PRECISION APPROACH AND LANDING NAVIGATION

EMPHASIS ON INERTIAL AND PSEUDOLITE AUGMENTATION AND DIFFERENTIAL IONOSPHERE EFFECT

A DISSERTATION
SUBMITTED TO THE DEPARTMENT OF AERONAUTICS AND ASTRONAUTICS
AND THE COMMITTEE ON GRADUATE STUDIES
OF STANFORD UNIVERSITY
IN PARTIAL FULFILLMENT OF THE REQUIREMENTS
FOR THE DEGREE OF
DOCTOR OF PHILOSOPHY

By
Ping-Ya Ko
May 2000

I certify that I have read this dissertation and that in my opinion it is fully adequate, in scope and quality, as a dissertation for the degree of Doctor of Philosophy.

J. David Powell
(Principal Adviser)

I certify that I have read this dissertation and that in my opinion it is fully adequate, in scope and quality, as a dissertation for the degree of Doctor of Philosophy.

Per K. Enge

I certify that I have read this dissertation and that in my opinion it is fully adequate, in scope and quality, as a dissertation for the degree of Doctor of Philosophy.

Jonathan P. How

Approved for the University Committee on Graduate Studies:

Abstract

The Differential Global Positioning System-based precision approach and landing architectures proposed by the Federal Aviation Administration (FAA) include the Wide Area Augmentation System (WAAS) and the Local Area Augmentation System (LAAS) for performing landings in Category (CAT) I and CAT III minima, respectively. The Required Navigation Performance (RNP) for GPS-based satellite navigation systems includes accuracy, continuity, integrity and availability. Previous studies have demonstrated that both the WAAS and the LAAS can provide the required accuracy. Current research focuses on the issues of integrity, continuity and availability. Specifically, pertinent research indicates that both systems are susceptible to possible interference and jamming that could damage their continuity and availability. Additionally, the carrier smoothed code algorithm is the current choice by the FAA for LAAS. The algorithm's influence on the error due to the differential ionosphere remains unexamined. Therefore, this thesis discusses the following topics:

- Inertial backup of GPS-Based precision approach and landing systems. This topic includes
  - Accuracy and continuity evaluation of an integrated WAAS/INS system.
  - Accuracy comparison among various LAAS algorithms and the integrated LAAS/INS system.
  - A backup system based on the integration of three pseudolites (PLs) with INS.
- The impact of the differential ionosphere error on the LAAS. This topic includes

- Evaluation of the threat.
- Seeking solutions and evaluating their costs and benefits.

Experimental data are used to develop the error models for both the WAAS and LAAS and the linear covariance analysis technique is used for the performance analysis. Analysis results indicate the following:

- Integrating an INS with WAAS can provide a temporary backup for GPS outages. This temporary backup is accomplished by using the INS which has been calibrated by the WAAS position update to satisfy the CAT I requirement. GPS outages clearly demonstrate the integration benefit of the WAAS/INS. However, the possibility of extending the integrated system performance to satisfy the CAT II requirement is limited.

- The performance of the integrated LAAS/INS system is comparable to that of the LAAS using a carrier phase algorithm.

- The 3-PLs/INS system can provide touch down performance in the absence of the data link, pseudolite synchronization and GPS signals.

- The differential carrier smoothed ionosphere delay (DCSID) ensures that the ionosphere spatial decorrelation error is not negligible. This research has identified the DCSID as a threat to LAAS availability and an influence on the time constant of the carrier smoothed code.

- The DCSID effect can be controlled via the ionosphere monitoring and calibration algorithm developed herein. However, this will require an increase in the bandwidth of the data link that transmits the ground monitored ionosphere gradients.

Acknowledgements

I would like to thank my advisor, Professor J. David Powell, for introducing me to Inertial Navigation Systems and GPS, and for giving me the opportunity to pursue this research. His clear guidance and comprehensive knowledge made this thesis possible and are highly appreciated. Professors Per K. Enge and Jonathan How are also appreciated for their constructive evaluation and criticism of this manuscript. Furthermore, I also wish to express my gratitude to my defense committee particularly Professor Stephan Monismith, a friend of my son, and Dr. Boris S. Pervan, who was the LAAS group manager and provided me with valuable research suggestions.

I would like to extend thanks to all of the GPS graduate students, particularly the members of the LAAS group, for their assistance during my research. Furthermore, I wish to thank Dr. Y. C. Chao, Dr. Y. J. Tsai for their encouragement and assistance. Special thanks go to Dr. Donghai Dai for our intelligent and constructive discussions. I also gratefully acknowledge Chung Shan Institute of Science and Technology (CSIST) for sponsoring my overseas study at Stanford to conduct this research.

Additionally, I would like to thank my parents, F. C. Ko and L. Y. Ko, for giving me endless love and encouragement during my academic studies. Finally and most importantly, I want to thank my son Shih-Hsien and my daughter Rachel for enduring the absence of their father, and my wife Lisa for her help, advice and encouragement over the course of my studies.

Contents

List of Tables

List of Figures

Chapter 1

Introduction

People have long dreamed to fly high and fast and to land smoothly and precisely. The introduction of the Global Positioning System and the evolution of the related technology have brought the dream to reality. However, to practically implement the Global Positioning System-based precision landing systems safely, we still need to prove that the path we followed and the technology we used match each other.

1.1 The Global Positioning System

The Global Positioning System (GPS), a satellite-based navigation system developed by the U.S. Department of Defense (DoD) in the 1970's, includes the space segment and the ground-based operational control segment (OCS). The minimum space segment has 24 satellites in 6 orbit planes with evenly spaced ascending nodes. (At this writing, there are 28 operational satellites.) Each orbit is nearly circular with a period of 11.97 hours and a 55^o inclination angle. To provide global coverage for the GPS users, satellites in each orbit plane are unevenly spaced to minimize the impact of a single satellite failure [Green]. Figure 1.1 illustrates the space segment. Each space vehicle (SV) has a Cesium atomic clock for precise timing and transmits on frequencies on L1 (1575.42MHz) and L2 (1227.60MHz) coded with an unique pseudorandom noise (PRN) to transmit navigation data.

The OCS includes 5 monitoring stations located at Colorado Springs, Ascension

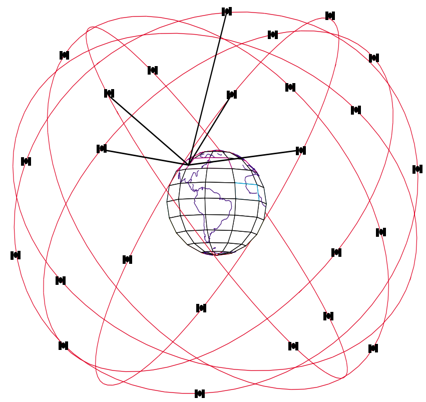

Figure 1.1: The Global Positioning System

Island, Diego Garcia, Kwajalein, and Hawaii to obtain the worldwide monitoring of each satellite in the space constellation. Information gathered by monitor stations is sent to the master control station to generate satellite clock corrections, ephemeris and health condition. This information is then sent to the satellite through three ground antennas distributed worldwide [Sherman]. The user receiver usually is equipped with a less accurate clock such as a quartz oscillator (XO) or a temperature controlled quartz oscillator (TCXO). Therefore, there is a clock bias between the user clock and the SV's clock. For a given SV, range is measured by the user receiver based on the offset between the received PRN code phase and a replica generated internally in the receiver. The received navigation data provide the receiver with the necessary information on SV location [Spilker].

The GPS positioning is to solve for the 3D user's position and the receiver clock bias by measuring ranges from at least 4 SVs with known SV locations. The standard positioning service (SPS) accuracy for the civilian user is limited to 100 meters horizontally and 150 meters vertically (a 2-sigma value) considering the major error source known as Selective Availability (SA) [SPS]. SA is the intentional degradation of the signal by dithering the satellite clock to make hostile usage more difficult. With the cancellation of SA in the future, the accuracy for the stand-alone user could be

Table 1.1: Required Navigation Performance

Item	CAT I	CAT II	CAT III
Decision Height (DH)	200+ ft	100+ ft	0-100 ft
Vertical Accuracy (95%) (A)	5 m	2.5 m	2.5 m
Continuity (C)	10^{-5}/ app	10^{-5}/ app	10^{-7}/ 30 s
Integrity (I)	4×10^{-8}/ app	4×10^{-8}/ app	10^{-9}/ app
Availability (A)	.999	.999	.999
Vertical Alert Limit (VAL)	10 m	5.3 m	5.3 m
Time to Alarm	6 sec	2 sec	2 sec

improved to within 10 meters [Parkinson].

1.2 Required Navigation Performance

For precision approach and landing, the required navigation performance (RNP) includes accuracy (A), continuity (C), integrity (I) and availability (Av) [Kelly].

- Accuracy is the navigation output deviation from truth.
- Integrity is the ability of a system to provide timely warnings to users when the system should not be used for navigation.
- Continuity is the likelihood that the navigation signal-in-space supports accuracy and integrity requirements for the duration of intended operation.
- Availability is the fraction of time the navigation function provides acceptable accuracy, integrity and continuity before the approach is initiated.

In other words, accuracy is how well your navigation system tells where you are. Integrity is the truthfulness of your navigation system when it gives you a position. Continuity is the ability of your navigation system to constantly provide you an accurate position with integrity. Availability is the ability of your navigation system to provide acceptable continuity, accuracy and integrity.

Today's precision approaches and landings based on the minimum weather conditions are classified into 3 categories, Category I, II and III. Decision height (DH) and runway visual range (RVR) are the parameters that characterize these categories. DHs for CAT I, II and III are 200 ft, 100 ft and 50 ft, respectively; and RVRs for CAT I, II and III should be greater than 2400 ft, 1200 ft and 700 ft, respectively. When conducting a CAT X (X is either I, II or III) precision approach, at the DH of that category, the pilot has to have the corresponding RVR, otherwise a missed approach will be initiated [AC120-28C]. The RNP for future precision approach and landing is still evolving. Therefore, the performance requirements considered in this thesis are summarized in Table 1.1 as a function of the category of weather minimums [Enge].

1.3 GPS-Based Precision Landing Systems

Obviously, the performance of the stand-alone GPS (Section 1.1) can not satisfy the requirements specified for the precision approach and landing as listed in Table 1.1. Augmentation systems are required for GPS-based precision approach and landing systems to fulfill the RNP.

Under the direction of the Federal Aviation Administration (FAA), augmentation systems are designed to achieve their specific requirements. The Wide Area Augmentation System (WAAS) is designed to meet the RNP as the primary navigator in oceanic flight, US domestic flight, US terminal areas, non-precision approach and CAT I precision approach. The Local Area Augmentation System (LAAS) is designed to support CAT I, II precision approaches and the most challenging CAT III landing. Additionally, Airport Pseudolites (APL's), a pseudo satellite placed inside the airport property, may become a component of the LAAS at some airports.

1.3.1 Wide Area Augmentation System

The WAAS, as shown in Fig. 1.2 , consists of a ground network and geostationary satellites. These nationwide ground stations at precisely known locations, called wide area reference stations (WRS's), collect and send raw GPS measurements back to wide area master stations (WMS's) to generate corrections, which are the satellite clock, the ephemeris, the ionospheric delay, and the associated integrity information.

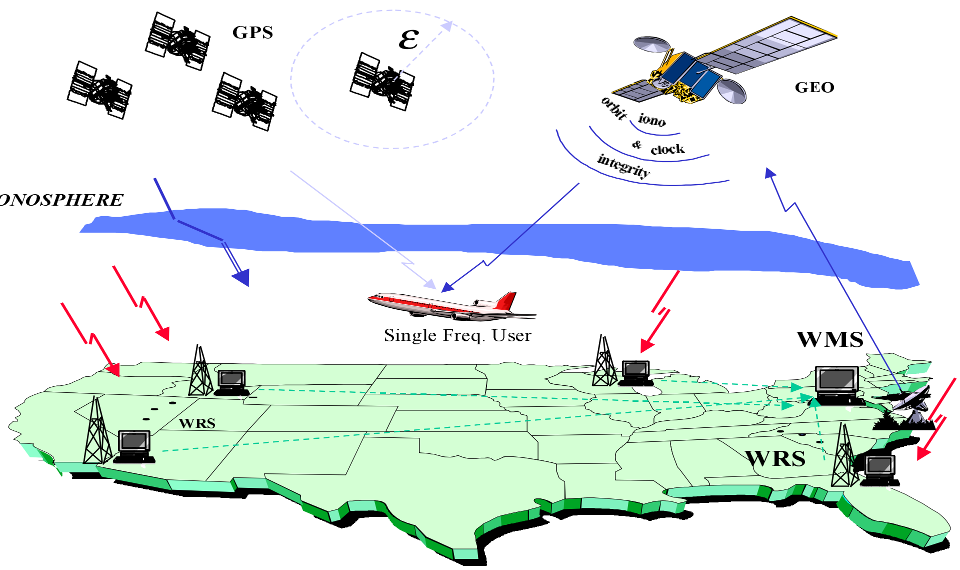

Figure 1.2: The Wide Area Augmentation System

All this information will be uploaded to geostationary satellites and then broadcast to an unlimited number of WAAS users across the nation. WAAS users will benefit from the WAAS system to obtain an improved position from 100 meters of the SPS without integrity information to better than 8 meters with integrity [Enge, a].

1.3.2 Local Area Augmentation System

LAAS, as shown in Fig. 1.3, consists of the space segment, the ground segment and the airborne segment. The space segment includes GPS and WAAS satellites that provide the ground and airborne segments with ranging signals and satellite ephemerides. The ground segment uses multiple high quality GPS receivers and antennas at known, surveyed locations on the airport property to generate differential code and carrier corrections, integrity parameters and precision approach pathpoint data. All this information is sent to the airborne users via a data link. The airborne user first applies the corrections to obtain an accurate position and then uses the accurate position along with the pathpoint data to produce deviation signals to conduct a CAT I, II or III precision approach and landing depending on the facilities of the

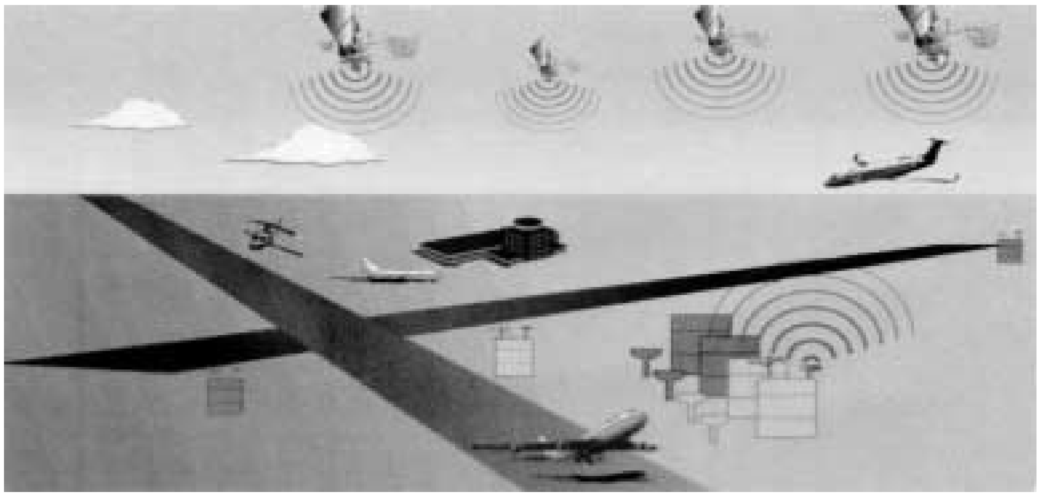

From FAALAAS

Figure 1.3: The Local Area Augmentation System

ground station and the aircraft.

1.3.3 Pseudolites

Beacons placed at or near the airport transmitting signals that are similar to a satellite are called PseudoLites (PLs). One approach PL augmentation system is known as the Integrity Beacon Landing System (IBLS) and uses two PLs placed ahead of the approach end of a runway to provide additional information so that differential carrier tracking could be accomplished. This system has been shown to be capable of centimeter-level accuracy that would enable CAT III landing [Cohen].

1.4 Research Topics and Motivation

1.4.1 Inertial Backup of GPS-Based Precision Approach and Landing Systems

The WAAS and LAAS, as described in the preceding sections, provide performance that satisfies the CAT I and III RNP for precision approach and landing, respectively. There are still disturbances, such as satellite outages, satellite geometry variation and radio frequency interference and/or jamming, that affect the realization of that performance. Additional augmentations to compensate the above disturbances include GPS-dependent augmentation and GPS-independent augmentation. In general, GPS-dependent augmentations, which can handle problems caused by the satellite outages and satellite geometry variation, contain geostationary satellites, the Russian GLObal NAvigation Satellite System (Glonass), approach PseudoLites (PLs), or Airport PseudoLites (APLs). GPS-independent augmentation, which is immune to interference and jamming, usually uses an Inertial Navigation System (INS). Therefore, INS can be a backup when GPS is jammed.

This topic, inertial backup of GPS-Based precision approach and landing systems, includes the integration of the WAAS and INS, the integration of the LAAS and INS, and a backup system based on the integration of 3 PLs with an INS. Motivation of this topic is to

- Evaluate the WAAS/INS performance improvements based on the National Satellite Test Bed (NSTB) WAAS position error data.
- Isolate the LAAS/INS performance improvements over LAAS alone.
- Investigate alternative backup ideas.

1.4.2 Differential Carrier Smoothed Ionosphere Effect on LAAS

Two techniques are applied to the LAAS signal processing algorithm: the carrier phase (CP) technique and the carrier smoothed code (CSC) technique. Research indicates that CSC can provide performance that satisfies the CAT I, II and III requirements [Hundley], [van Graas], [van Graas, a] with an apparently easier implementation. Therefore, the LAAS program has selected the CSC as the official algorithm.

CSC uses the carrier phase to smooth the noisy code phase and uses the code phase to initialize position. CSC is actually a low pass filter that filters out the high frequency content of the code phase measurement. Then, a smooth but delayed code phase is obtained for the differential GPS positioning. This delayed effect will cause problems when the ionosphere gradient between the airborne user and the ground station is strong. In the past, the short distance between the airborne user and the ground station allowed researchers to ignore the influence of the ionosphere gradient on local area DGPS applications. However, the delay effect introduced by the CSC essentially increases the distance between the airborne user and the ground station and makes the decorrelation effect of the differential ionosphere delay on the LAAS to be significant again. This motivates the research of this topic to evaluate the previously ignored differential carrier smoothed ionosphere effect on LAAS.

1.5 Previous Work

1.5.1 Inertial Backup of GPS-Based Precision Approach and Landing Systems

- Interference and jamming

  Interference and jamming are real threats to GPS-based precision approach and landing systems including the WAAS and the LAAS. Interference sources, such as the Mobile Satellite Services (MSS), has been identified as a real threat to the GPS-based precision approach and landing system. Johnson analytically demonstrated that GPS-based landing systems have little margin (0.06 dB) for MSS [Johnson] and Nisner measured radio frequency interference to GPS receivers and identified that MSS is a serious threat to the GPS navigation [Nisner]. Nisner also identified that TV stations are a potential threat to the

GPS navigation by experimental measurements [Nisner]. For WAAS, analytical work done by Schnaufer demonstrated there is little or no performance margin for a WAAS/GPS receiver to satisfy the Word Error Rate (WER) requirement specified in the WAAS MOPS [Schnaufer]. Hegarty also came to the same conclusion [Hegarty]. All of these works motivate the research of inertial backup of the GPS-based precision approach and landing system.

- Integration of the WAAS with an INS

  Intuitively the integration of an INS with GPS-based precision approach and landing systems will not only augment the continuity but also improve the accuracy of the system. For example, Diesel from Litton, using a simplified 1-D example, analytically showed that integration of the WAAS and an INS can provide a better accuracy and meet the CAT II requirement by assuming that most of the GPS error sources are fast with a time constant of less than 10 seconds [Diesel]. However, analysis of experimental WAAS data with an integrated INS has never been done. The results change the conclusion from Diesel. Details will be given in Chapter 2.

- Integration of the LAAS with an INS

  Prior research showed that the integration of Local Area DGPS with an INS could provide RNP for the CAT III precision approach and landing. Paielli et al. from NASA demonstrated that by using loosely coupled integration of a carrier phase DGPS with a navigation grade INS, CAT III requirements could be met even with no DGPS updates after 200 feet height above runway [Paielli]. Similar results were also demonstrated by Meyer-Hilburg and Harder from Daimler-Benz Aerospace AG [Meyer]. However, the performance difference, especially accuracy, between the integrated DGPS/INS system and the DGPS alone using filtering techniques has not been explored or clearly explained. Details will be discussed in Chapter 3.

- Integration of PLs with an INS

  Pseudolites have been shown to improve GPS geometry for mobile users [Klein].

Pseudolites have also been used to help with ambiguity resolution as in the IBLS system demonstrated by Cohen et al. [Cohen, a]. Pervan used ground-based pseudolites for autonomous integrity monitoring during aircraft precision approach and landing [Pervan]. Later, Lawrence brought the approach PLs into the airport property [Lawrence] and Pervan et al. demonstrated that in-track APLs could also provide the performance required by CAT III landing [Pervan, a]. All of the above researches were focused on using PLs to augment a DGPS-based precision approach and landing system. However, using PLs as the main body of a precision approach and landing system as a backup when the DGPS-based system fails has not been developed yet. I developed a PL-based backup system by integrating three PLs with an INS. Performance analysis and integration details will be given in Chapter 4.

1.5.2 Differential Carrier Smoothed Ionosphere Effect on LAAS

The effects of differential ionosphere delay on DGPS users are small in the local area application as pointed out by Klobuchar [Klobuchar]. However, for precision applications such as LAAS, the ionosphere decorrelation is still an issue. Therefore, Pervan considered the differential ionosphere delay as an error source in the carrier phase-based algorithm of the IBLS system. Based on [Klobuchar, a], a vertical ionosphere delay of 3 mm/km (3ppm, 1σ) was used in the IBLS system [Pervan, b]. Some other researches documented that the spatial decorrelation of the ionosphere is much larger then the value that [Klobuchar, a] presented. For example, Goad measured a decorrelation of 50 cm over a 9 kilometers baseline (55.6ppm) in Antarctica [Goad]. Wanninger recorded a 5 meters gradient of the ionosphere over a 100 km baseline (50ppm) in Brazil during the last solar maximum period [Wanninger]. Doherty reported a 12 mm/sec temporal vertical ionosphere gradient in the evening at Fairbanks, AK, in a solar moderate period [Doherty]. Warnant discussed the potential impact of Travelling Ionospheric Disturbances (TID) and the resulting severe ionosphere gradient over a 15 to 20 km baseline on the limitations for geodetic applications of DGPS [Warnant]. These observed ionosphere gradients are quite alarming since they are certainly not the worst possible points but the observed worst in the limited observations. In light of the above alarming data, the combined effect of the carrier smoothed code and the differential ionosphere delay on LAAS has not been investigated yet. In Chapter 5, I will discuss the influence of the differential carrier smoothed ionosphere delay on LAAS and how to cope with it.

1.6 Contributions

Contributions made in this dissertation can be summarized in the following.

1.6.1 Inertial Backup of GPS-Based Precision Approach and Landing Systems

- WAAS/INS integration

  First analysis to establish that INS augmentation of WAAS yields no significant improvement in accuracy.

- LAAS/INS integration

  Isolation of important INS features for Differential GPS (DGPS)/INS system performance. LAAS/INS is comparable to the performance of the LAAS alone using carrier phase algorithm.

- Integration of PLs with an INS

  Provides an alternative backup idea using PLs and INS only to accomplish touchdown landings.

1.6.2 Differential Carrier Smoothed Ionosphere Effect on LAAS

- Discovered an error source, previously ignored, that significantly affects the availability of a LAAS-based landing system in a worst case analysis. This analysis showed that the differential carrier smoothed ionosphere delay is not negligible in the precision CAT II/III application of DGPS such as the LAAS.

- Provided an analytical expression of the differential carrier smoothed ionosphere delay. In the analytical expression, it shows that

  – using different carrier smoothing time constants for the mobile user and the ground station and

  – using a longer carrier smoothing time constant for the mobile user

  will worsen the differential ionosphere effect on LAAS. The first point was ignored in previous research and the second point, to use a larger carrier smoothing time constant, is a common idea in the LAAS community to further reduce the code phase noise. Both points are harmful to the LAAS and this fact is first identified in this research.

  The analytical expression itself is an excellent tool for further understanding of the effect of the carrier smoothed differential ionosphere delay on LAAS.

- Characterized the effect of the differential carrier smoothed ionosphere delay on the availability of LAAS in the worst geometry case. The result shows that the impact of the differential carrier smoothed ionosphere delay on the availability of LAAS is significant.

- Provided a Single Frequency Ionosphere Monitoring and Correction algorithm.

  After the effect of the differential carrier smoothed ionosphere delay on LAAS has been characterized, a monitoring and correction algorithm for single frequency users has also been provided to monitor the presence of the ionosphere gradient in real-time and correct for the differential ionosphere effect onboard.

Benefit and cost of applying the single frequency monitoring and correction algorithm have also been characterized. Results showed the benefit is significant and the cost is reasonable.

Chapter 2

Integration of the WAAS with an INS

2.1 Inertial Backup of GPS-Based Precision Approach and Landing Systems

Inertial Navigation System (INS) can provide the attitude and three-dimensional position and velocity of the vehicle it is carried on. INS consists of an inertial measurement unit (IMU) and a computer unit (CU). The IMU includes inertial sensors, which are accelerometers and gyros, and electronics. It measures the acceleration and angular rates of the vehicle and then converts the measurements into a digital format. CU uses the measured accelerations and angular rates to compute (basically through coordinate transformation and integration) the carrying vehicle's attitude, three-dimensional position, and velocity.

Measurement uncertainty of the inertial sensors leads to errors in the computed attitude and position. Measurement uncertainty generally includes bias, temperature effect, noise and scale factor, as well as other factors. Due to the integration process, these error terms will accumulate over time. Therefore, the errors of computed attitude and position increase progressively and smoothly. Figure 2.1 illustrates the typical position error of an INS. According to this figure, although the long-term error

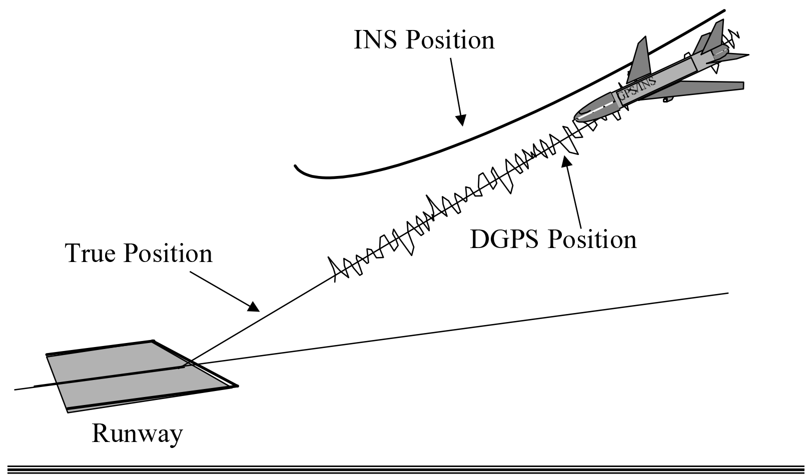

Figure 2.1: Illustration of Position Error Characteristics of the INS and DGPS

of the INS is poor, the short-term error of the INS is smooth and good.

DGPS is adequate for precision approach and landing applications. The fundamental mathematics of the DGPS uses at least four differential pseudorange measurements and knowledge of the satellite location and the reference station to determine the relative position of the roving user. Error sources include the pseudorange measurement noise, modeling uncertainties, and satellite geometry. Since no integration process is involved in the DGPS algorithm, the position error of the DGPS does not increase with time.

Restated, DGPS is accurate in the long term, despite noisiness in the short term. An illustration is also shown in Fig. 2.1. Besides the above error sources, disturbances such as interference and jamming threats, satellite outages, may also disrupt the availability and continuity of the accuracy of DGPS-based systems.

The above two systems appear to complement each other perfectly. Specifically, the short-term stability of the INS can be employed to smooth the noisy position of the DGPS, while the long-term stability of the DGPS can be used to confine the drifting

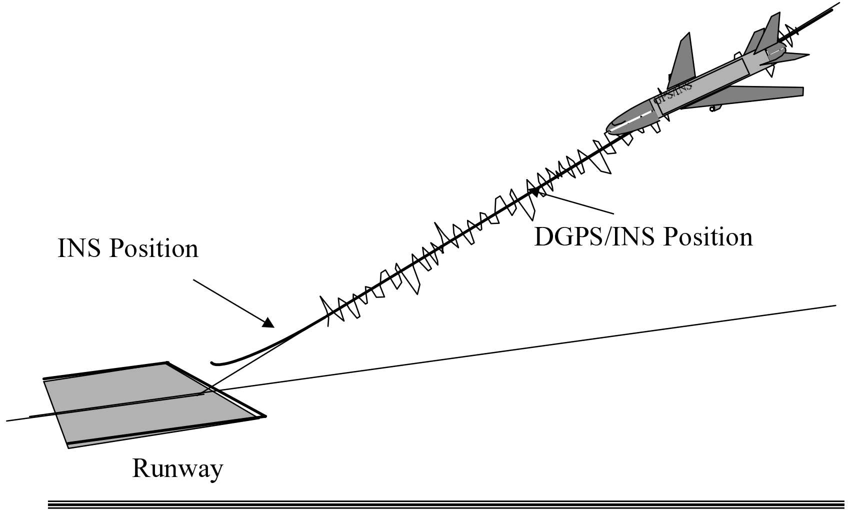

Figure 2.2: Illustration of Position Error Characteristics of the Integrated DGPS/INS

INS. When the DGPS is available, the error sources of the INS can be calibrated. Meanwhile, when DGPS disturbances occur, the calibrated INS can be used to carry through the disturbed period [Eissfeler], [Mayer], [Vieweg]. Figure 2.2 illustrates the notion of complementary filtering.

To integrate the two navigation systems, the error model of both systems must be developed and calibrated by measurements. The Kalman Filter technique is used to integrate DGPS and INS. The Kalman Filter estimates the major errors of the INS and continuously calibrates the INS in flight. Theoretically, the integrated navigation system should provide a smoother and more accurate position since the DGPS position has been low-pass filtered to eliminate the noise and the INS position has been high-pass filtered to eliminate the long-term error. Consequently, when DGPS disturbances occur, the integrated system navigates based on the corrected INS. The integration performance will be evaluated using the covariance of the estimation error. In addition to developing the WAAS position error model based on experimental data, this chapter describes the structure of integrating the WAAS with an INS and

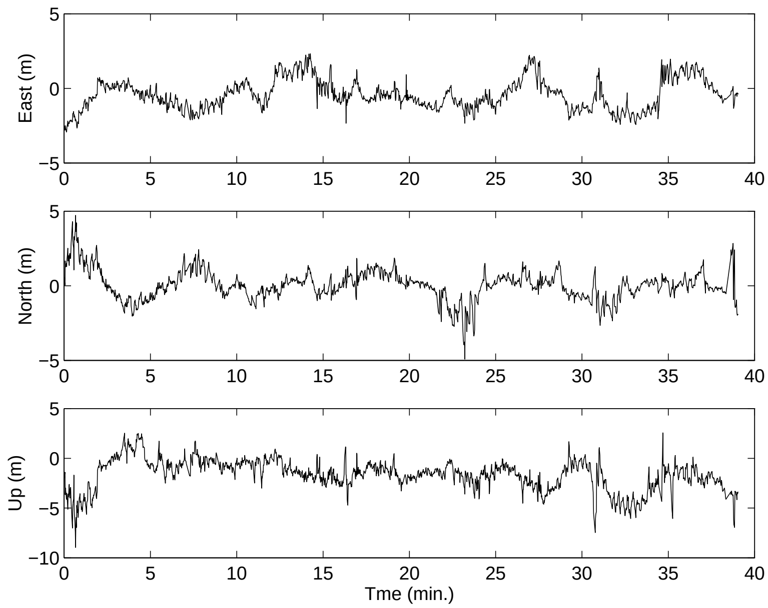

Figure 2.3: Dynamic User WAAS Position Error in the ENU Frame Using a Single Frequency Receiver without CSC, Obtained from 09/11/97 Moffett Flight Test - Courtesy of Dr. D. Dai

evaluates the performance of the WAAS/INS.

2.2 The WAAS Position Error Model

The WAAS position error model used in this study is derived from experimental data sets generated by subtracting the WAAS position, which uses the National Satellite Test Bed (NSTB) WAAS corrections, from the truth position for both dynamic and static users. The truth position for a static user is the presurveyed position while that for a dynamic user is the reference trajectory derived by the IBLS system, which provides centimeter level accuracy. These WAAS position error data sets are currently the most representative for future operational WAAS.

Figure 2.3 presents the east (E), the north (N) and the up (U) direction position errors, respectively, in the ENU frame of a single frequency dynamic user without

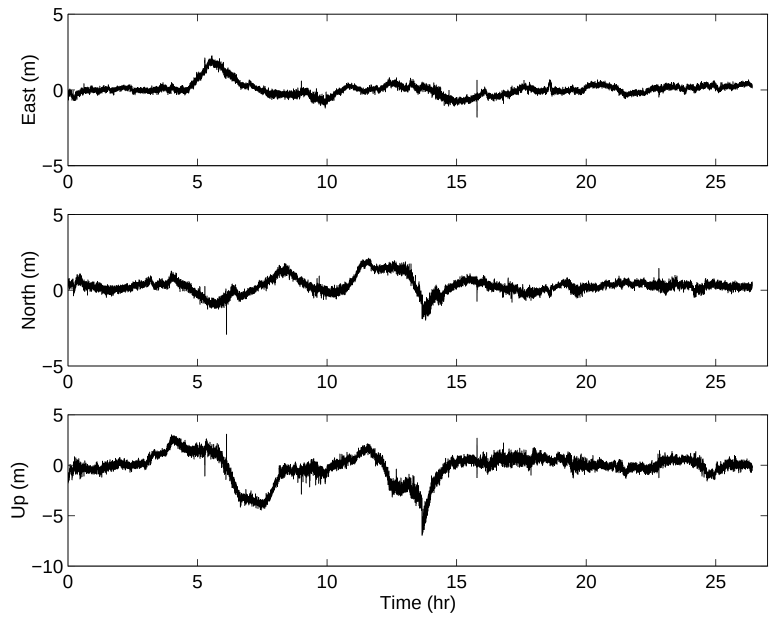

Figure 2.4: Static User WAAS Position Error in the ENU Frame Using a Dual Frequency Receiver with CSC, Obtained from FAA T.C. Static Test - Courtesy of Dr. Y. J. Tsai

using Carrier Smoothed Code (CSC) for approximately 40 minutes. The flight test was conducted on 09/11/97 at Moffett airport, Mountain View, California. Figure 2.3 indicates that the airborne position error includes not only a fast variation but also a slow drift (apparent in the UP direction). Obviously, the time constant of the slow drift is substantially longer than the flight test duration and it will be too expensive and time consuming to conduct a flight test that is sufficiently long to characterize the slow drift. For this purpose, a static test result is used.

Figure 2.4 Static User WAAS Position Error in the ENU Frame presents the E, N and U direction position errors, respectively, in the ENU frame of a dual frequency static user at the FAA Technical Center (FAA T.C.) with CSC applied for over 24 hours. For a dual-frequency user, the applied CSC eliminates the local environment effect, the multipath [Tsai]. Therefore, the position error typically depends on the local geometry, number of available WAAS corrections and accuracy of these corrections. Since the number of WAAS corrections and the position error are not highly correlated and the local geometry changes randomly with location, they will be treated as a part of the WAAS inherent error and contribute to the slow variation part of the position error. Figure 2.4 reveals that with the CSC applied, the random noise is negligible and the slow variation dominates the position error variation.

Based on the observation of the WAAS position errors (Figs. 2.3 and 2.4), it was judged that the airborne WAAS position error can be modeled as a combination of a fast and slow stochastic process. The fast variation part of the airborne position can be modeled with the detrended flight test data, while the slow drifting part of the dynamic position error can be approximated and modeled using the static user position error.

In addition to describing the identified slow variation model and the fast variation model, the following sections summarize the WAAS position error modeling in detail.

2.2.1 Slow Variation Model

Applying the above procedure, the square root of the spectrum of the slow variation part of the position error is shown in Fig. 2.5

The modeling procedures of the slow component are outlined below

- Establish the relationship between the power spectrum and the magnitude part of the Bode plot. This relationship then provides an idea of the model type, for example AR or ARMA, and the model order.
- Use time domain regression to obtain the parameters of the model.
- Compare the magnitude part of the Bode plot of the identified model with the power spectrum.
- Compare the simulated time series with the data.

Applying the above procedure, the square root of the spectrum of the slow variation part of the position error is shown in Fig. 2.5 . The data set used to generate these spectra is the same as that used in Fig. 2.4, but down-sampled at one data

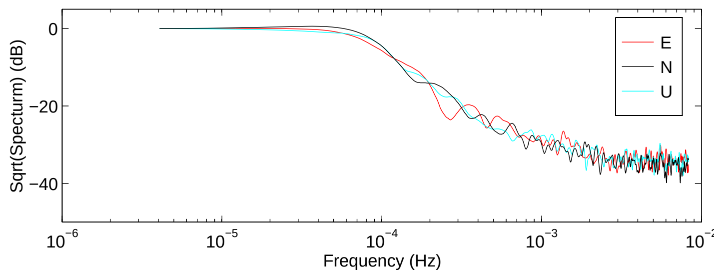

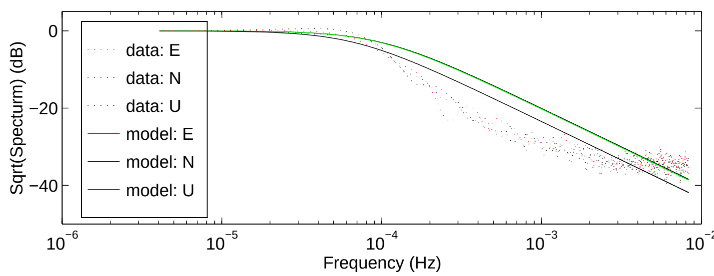

Figure 2.5: Power Spectrum of the WAAS Error - Slow Component. Top: Square roots of the normalized position error power spectra. Bottom: Square roots of the normalized power spectra of the data and the first order GMP.

point per minute. The top plot of Fig. 2.5 implies that, in each direction, the slowly changing process can be modeled as a simple first order Gauss-Markov Process (GMP) with a time constant approximately three hours without losing any generality. For a first order GMP, two parameters must be specified, the time constant and the driving noise. The time constant can be identified by applying time series analysis [Pandit], [Eykhoff] to the data set. Meanwhile, the driving noise is equal to the standard deviation of the data set.

Applying time series analysis theory to these data sets and using the ARX model of MATLAB, the discrete time GMP parameter can be identified. Then, transforming the discrete time parameter to the continuous time domain, the time constant, τ_{slow}, of the GMP can be obtained. The bottom plot of Fig. 2.5 displays the parameter identification results. The dotted lines depict the square root spectrum of the measured data and the solid lines present the magnitude part of the Bode plot of the identified first order GMP. The agreement between the data and the models indicates the goodness-of-fit. Although there is as much as a 10 dB error, the models are considered acceptable, as discussed in Section 2.5.1. Figure 2.6 presents the time

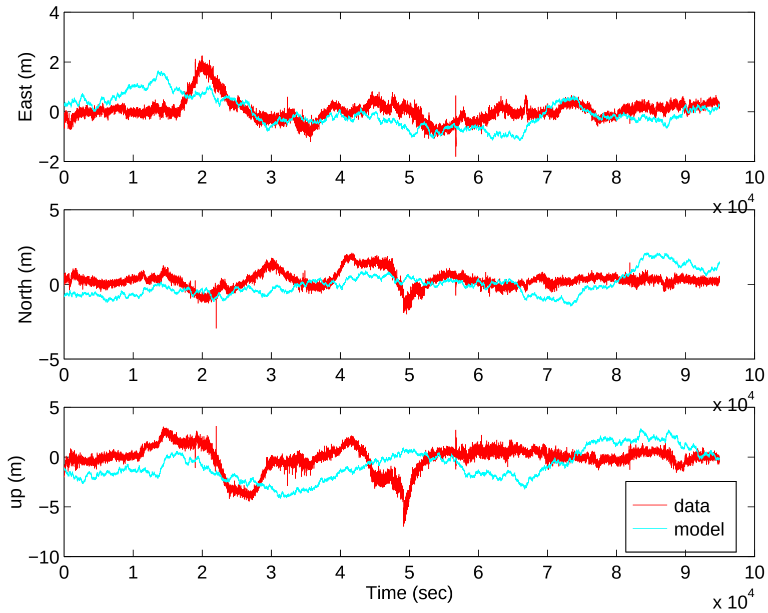

Figure 2.6: Slow Component Model Evaluation: Comparison between the static test data and the 1st order GMP model in the E , N and U directions, respectively.

Table 2.1: Parameters of the Slow Component of the WAAS Error

Direction	East	North	Up
Time Constant τ (min.)	167	167	248
Driving Noise σ (m)	0.437	0.612	1.337

domain simulation of the identified model. The driving noise is based on the standard deviation of the data set. Except for the peak in the data at 5000 seconds, the identified GMP model is adequate.

Table 2.1 presents the identified parameters of the slow component in the E, N and U directions, respectively.

The position errors are not independent of each other because the GPS position is a WLS solution of the pseudorange normal equation. The independent noises are the pseudorange noises. The position error is a linear combination of all the independent pseudorange noises. However, the modeling method used herein treats the position error in each direction as an independent error, thus producing an optimistic covariance analysis result. Considering the actual situation, the cross-coupling components in the covariance matrix of the initial condition must be included to resolve the

Table 2.2: Parameters of the Fast Component of the WAAS Error

Direction	East	North	Up
Time Constant τ (min.)	2.9	3.0	2.8
Driving Noise σ (m)	0.972	0.996	1.449

non-independent effect. Although the cross-coupling components are time-variant, depending on the satellite geometry, it is assumed that a lumped cross-coupling noise matrix can accurately represent a system-level covariance analysis. For a detailed system design, the WAAS system must provide these cross-coupling components.

The covariance matrix of the initial condition in ENU frame is obtained via MATLAB's cross-correlation function of the 3 data sets (the east, north and up directions) in Fig. 2.6 and is listed below.

$$\mathrm{P}_{0,slow} = \begin{bmatrix} 0.1913 & -0.0563 & 0.0195 \\ -0.0563 & 0.3745 & 0.0266 \\ 0.0195 & 0.0266 & 1.7866 \end{bmatrix} \tag{2.1}$$

2.2.2 Fast Variation Model

This section considers a heuristic means of model identification by observing the normalized power spectra of the E, N and U position errors. The top figure of Fig. 2.7 indicates that the square roots of power spectra (essentially, the magnitude part of the Bode plot) of the position errors in E, N and U directions resembles a first order causal system. Therefore, the stochastic model that can describe these position errors is also a first order Gauss-Markov process, which requires a time constant and a driving noise for specification. The time constant can be read from the power spectrum, while the driving noise can be found by referring to the standard deviation of the position error. Table 2.2 lists the time constants and driving noises of the identified first order GMPs.

The bottom figure of Fig. 2.7 presents both power spectra of the data and the models. Evidently, these first order GMPs are a good representation of the fast component of the WAAS position error.

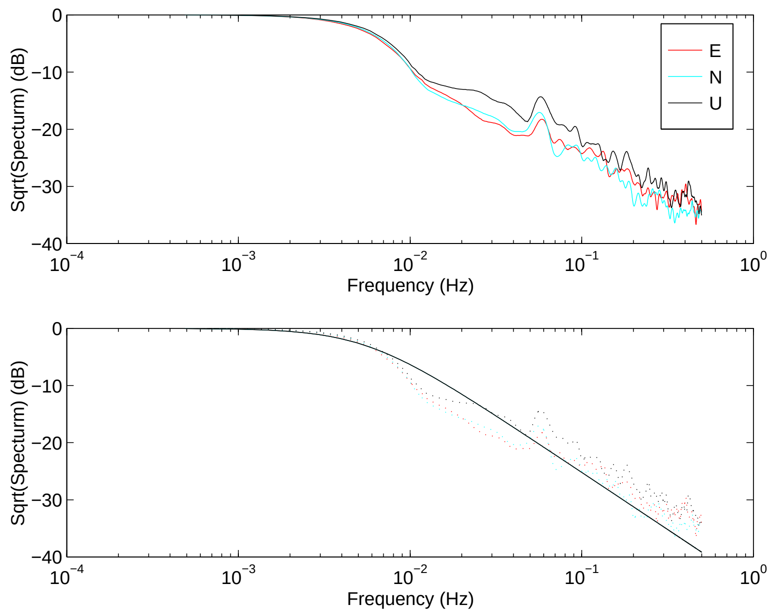

Figure 2.7: Power Spectrum of the WAAS Error - Fast Component. Top: Square roots of the normalized position error power spectra. Bottom: Square roots of the normalized power spectra of the data (dotted curves) and the first order GMP (lines).

Figure 2.8 presents the model evaluation result of the time domain simulation. The simulated position errors can reflect the low frequency characteristics. Meanwhile, for the high frequency parts, the simulated position errors are unimportant because they will be smoothed out by either the CSC or the integration filter. Some spikes in the position solution are shown in Fig. 2.8. They are due to WAAS signal outages caused by intermittent ground-based data link drop outs. For the operational WAAS, the satellite-based data link should provide more stable service and, therefore, these spikes in the position solution should not be a concern.

As discussed for Eqn. 2.1, the covariance matrix of the initial condition in ENU frame is obtained by performing the cross-correlation of the data sets in Fig. 2.3 and is listed below.

$$\mathrm{P}_{0,fast} = \begin{bmatrix} 0.9919 & 0.0317 & 0.4464 \\ 0.0317 & 0.9445 & -0.4833 \\ 0.4464 & -0.4833 & 2.0999 \end{bmatrix} \tag{2.2}$$

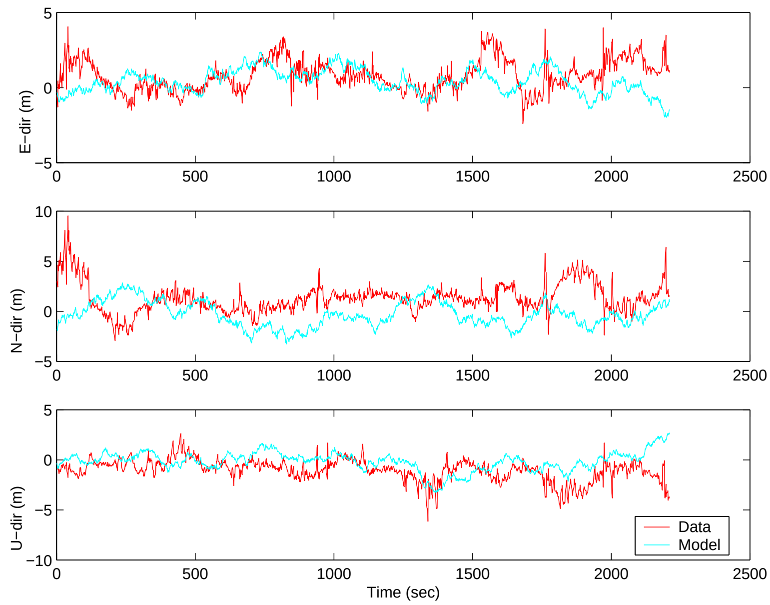

Figure 2.8: Fast Component Model Evaluation: Comparison between the flight test data and the 1st order GMP model in the E , N and U directions, respectively.

2.2.3 Summary of the WAAS Position Error Model

The WAAS error models and their identified parameters are summarized below for further reference.

- WAAS error model:

$$\begin{aligned} \delta \mathbf{x}_{WAAS} &= \delta \mathbf{x}_{fast} + \delta \mathbf{x}_{slow} \\ \delta \dot{x}_{fast,i} &= \frac{-1}{\tau_{fast,i}} \delta x_{fast,i} + \frac{1}{\tau_{fast,i}} \nu_{fast,i} \\ \delta \dot{x}_{slow,i} &= \frac{-1}{\tau_{slow,i}} \delta x_{slow,i} + \frac{1}{\tau_{slow,i}} \nu_{slow,i} \end{aligned} \tag{2.3}$$

where subscript i denotes the E, the N and the U direction, respectively, and ν represents the driving noise of the first order GMP with zero mean and a sigma value specified below.

- The identified parameters:

Model	Fast			Slow		
Direction	East	North	Up	East	North	Up
Time Constant τ (min .)	2.9	3.0	2.8	167	167	248
Driving Noise σ (m)	0.972	0.996	1.449	0.437	0.612	1.337

2.3 The INS Error Model

The INS error model considered herein is based on an Earth-Centered, Earth-Fixed (ECEF) coordinate frame (e-frame). This frame is convenient since satellite position and velocity, computed from GPS satellite ephemeris parameters, are given in ECEF coordinates. Appendix A presents a detailed derivation of the INS error equations mechanized in ECEF. The equations are summarized as follows.

States included in the INS error model include the navigation error states and sensor error states. Navigation error states are defined as

$$\mathbf{x}_{nav} = \begin{bmatrix} \varepsilon \\ \delta\mathbf{x} \\ \delta\mathbf{v} \end{bmatrix} \tag{2.4}$$

where ε is the tilt error vector, which is defined as the misalignment errors of the transformation between the body frame (b) and the e-frame, and $\delta\mathbf{x}$ and $\delta\mathbf{v}$ are the position error vector and velocity error vector coordinatized in the e-frame. Sensor error states generally considered in the INS error model include

$$\mathbf{x}_{sensor} = \begin{bmatrix} \mathbf{b} \\ \mathbf{d} \\ \mathbf{K}_a \\ \mathbf{K}_g \end{bmatrix} \tag{2.5}$$

where $\mathbf{b}$ is the accelerometer bias vector, $\mathbf{d}$ is the gyro drift vector, $\mathbf{K}_a$ is the scale factor vector of the accelerometers, and $\mathbf{K}_g$ is the scale factor vector of the gyros.

The state equation of the INS error model can therefore be expressed as

$$\begin{bmatrix} \dot{\mathbf{x}}_{nav} \\ \dot{\mathbf{x}}_{sensor} \end{bmatrix} = \begin{bmatrix} \mathbf{F}_{nav} & \mathbf{F}_{ns} \\ \mathbf{0} & \mathbf{F}_{sensor} \end{bmatrix} \begin{bmatrix} \mathbf{x}_{nav} \\ \mathbf{x}_{sensor} \end{bmatrix} + \begin{bmatrix} \mathbf{G}_{nav} \\ \mathbf{G}_{sensor} \end{bmatrix} \upsilon_{sensor} \tag{2.6}$$

where $\mathbf{F}_{nav}$ is the state transition matrix of the navigation error states derived from the equation of motion of the INS and detailed in Appendix A; $\mathbf{F}_{sensor}$ is the state transition matrix of the sensor error states that include the first order Gauss-Markov processes of the accelerometer bias $\mathbf{b}$ and gyro drift $\mathbf{d}$, and also constant biases of scale factors ($\mathbf{K}_a$, $\mathbf{K}_g$) of the accelerometers and gyros; $\mathbf{F}_{ns}$ is the cross-coupling effect that links the dynamics between the sensor error states and the navigation error states; $\mathbf{G}_{nav}$ is the process noise, which is the measurement noise of the INS sensors, input matrix of the navigation error state equation; $\mathbf{G}_{sensor}$ is the driving noise input matrix of the sensor error states. Expressions of these matrices are given below.

$$\begin{aligned}
\mathbf{F}_{nav} &= \begin{bmatrix} -\omega_{ie}^{e}\times & \mathbf{0} & \mathbf{0} \\ \mathbf{0} & \mathbf{I} & \mathbf{0} \\ -\mathbf{F}^{e} & \mathbf{N} & -2\omega_{ie}^{e}\times \end{bmatrix} \\
\mathbf{F}_{ns} &= \begin{bmatrix} \mathbf{C}_b^e & \mathbf{0} & diag(\omega^b) & \mathbf{0} \\ \mathbf{0} & \mathbf{0} & \mathbf{0} & \mathbf{0} \\ \mathbf{0} & \mathbf{C}_b^e & \mathbf{0} & diag(\mathbf{f}^b) \end{bmatrix} \\
\mathbf{F}_{sensor} &= diag\left(\tfrac{-1}{\tau_a}[1\ 1\ 1] \quad \tfrac{-1}{\tau_g}[1\ 1\ 1] \quad [0\ 0\ 0] \quad [0\ 0\ 0] \right) \\
\mathbf{G}_{nav} &= \begin{bmatrix} \mathbf{C}_b^e & \mathbf{0} & \mathbf{0} & \mathbf{0} \\ \mathbf{0} & \mathbf{0} & \mathbf{0} & \mathbf{0} \\ \mathbf{0} & \mathbf{C}_b^e & \mathbf{0} & \mathbf{0} \end{bmatrix} \\
\mathbf{G}_{sensor} &= \begin{bmatrix} \mathbf{0} & \mathbf{0} & diag(\frac{\mathbf{1}}{\tau_a}[1\ 1\ 1]) & \mathbf{0} \\ \mathbf{0} & \mathbf{0} & \mathbf{0} & diag(\frac{\mathbf{1}}{\tau_g}[1\ 1\ 1]) \\ \mathbf{0} & \mathbf{0} & \mathbf{0} & \mathbf{0} \\ \mathbf{0} & \mathbf{0} & \mathbf{0} & \mathbf{0} \end{bmatrix} \\
\upsilon_{sensor} &= \begin{bmatrix} \upsilon_a^* & \upsilon_g^* & \upsilon_b^* & \upsilon_d^* \end{bmatrix}^*.
\end{aligned} \tag{2.7}$$

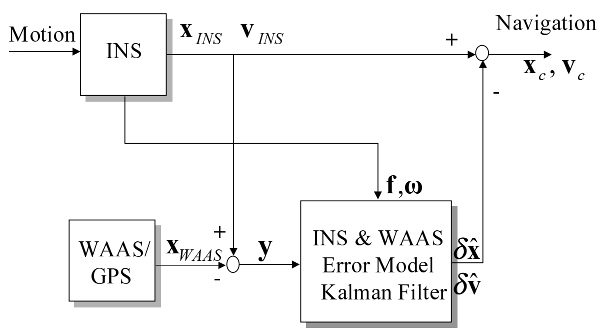

Figure 2.9: WAAS/INS Integration Structure

In Eqn. 2.7, $\omega_{ie}^e\times$ is the skew-symmetric matrix of the rotation rate of the earth in e-frame; $\mathbf{I}$ is the unity matrix; $\mathbf{F}^e$ is the skew-symmetric matrix of the specific force in the e-frame; $\mathbf{N}$ is the Jacobian of the gravity model in the e-frame; $\mathbf{C}_b^e$ is the coordinate transformation matrix from the b-frame to the e-frame; ω^b is the measured angular rate vector in the b-frame; $\mathbf{f}^b$ is the specific force vector in the b-frame; τ_a is the correlation time constant of the accelerometer bias; τ_g is the correlation time constant of the gyro drift; υ_a is the measurement noise vector of the accelerometer; υ_g is the measurement noise vector of the gyro; υ_b is the driving noise vector of the accelerometer bias; υ_d is the driving noise vector of the gyro drift; and superscript * represents the transpose of a matrix.

2.4 The Integration Filter

This section considers an open-loop feedforward integration structure (Fig. 2.9) of the WAAS and a navigation grade INS that has been proved feasible to LAAS applications by R. Paielli et al. [Paielli]. Two independent systems are integrated by making the difference of the output of these two systems the input to the integration filter. Consequently, estimates of the position error and velocity error are fed forward and subtracted from the inertial output to obtain a better position solution.

The state equation of the integration filter is a collection of the state equation of the two independent systems, i.e. Eqn. 2.6 of the INS error model and Eqn. 2.3 of the WAAS error model. Presenting these two equations in the state-space form, the state equation of the integration filter can be expressed as below.

$$\begin{bmatrix} \dot{\mathbf{x}}_{nav} \\ \dot{\mathbf{x}}_{sensor} \\ \delta\dot{\mathbf{x}}_{fast} \\ \delta\dot{\mathbf{x}}_{slow} \end{bmatrix} = \begin{bmatrix} \mathbf{F}_{nav} & \mathbf{F}_{ns} & \mathbf{0} & \mathbf{0} \\ \mathbf{0} & \mathbf{F}_{sensor} & \mathbf{0} & \mathbf{0} \\ \mathbf{0} & \mathbf{0} & \mathbf{F}_{fast} & \mathbf{0} \\ \mathbf{0} & \mathbf{0} & \mathbf{0} & \mathbf{F}_{slow} \end{bmatrix} \begin{bmatrix} \mathbf{x}_{nav} \\ \mathbf{x}_{sensor} \\ \delta\mathbf{x}_{fast} \\ \delta\mathbf{x}_{slow} \end{bmatrix} + \begin{bmatrix} \mathbf{G}_{nav} & \mathbf{0} & \mathbf{0} \\ \mathbf{G}_{sensor} & \mathbf{0} & \mathbf{0} \\ \mathbf{0} & \mathbf{G}_{fast} & \mathbf{0} \\ \mathbf{0} & \mathbf{0} & \mathbf{G}_{slow} \end{bmatrix} \begin{bmatrix} \upsilon_{sensor} \\ \upsilon_{fast} \\ \upsilon_{slow} \end{bmatrix} \tag{2.8}$$

where $\mathbf{F}_{fast}$ and $\mathbf{F}_{slow}$ are the state transition matrices of the fast and slow components of the WAAS error, respectively; $\mathbf{G}_{fast}$ and $\mathbf{G}_{slow}$ are the noise input matrices, respectively. These matrices are given as follows.

$$\begin{aligned} \mathbf{F}_{fast} &= diag(\begin{bmatrix} \frac{-1}{\tau_{fast,E}} & \frac{-1}{\tau_{fast,N}} & \frac{-1}{\tau_{fast,U}} \end{bmatrix}) \\ \mathbf{F}_{slow} &= diag(\begin{bmatrix} \frac{-1}{\tau_{slow,E}} & \frac{-1}{\tau_{slow,N}} & \frac{-1}{\tau_{slow,U}} \end{bmatrix}) \\ \mathbf{G}_{fast} &= -\mathbf{F}_{fast} \\ \mathbf{G}_{slow} &= -\mathbf{F}_{slow}. \end{aligned} \tag{2.9}$$

The measurement of the integration filter is the difference between the INS position error ($\delta\mathbf{x}$ in Eqn. 2.4) and the WAAS position error ($\delta\mathbf{x}_{WAAS}$ in Eqn. 2.3.) Therefore, the measurement equation is expressed as

$$\mathbf{y} = \begin{bmatrix} \mathbf{H}_{nav} & \mathbf{0} & -\mathbf{I} & -\mathbf{I} \end{bmatrix} \begin{bmatrix} \mathbf{x}_{nav} \\ \mathbf{x}_{sensor} \\ \delta\mathbf{x}_{fast} \\ \delta\mathbf{x}_{slow} \end{bmatrix} \tag{2.10}$$

where $\mathbf{H}_{nav} = \begin{bmatrix} \mathbf{0} & \mathbf{I} & \mathbf{0} \end{bmatrix}$. Obviously, two independent systems are coupled by the measurement equation.

With the state and measurement equations of the integration filter, the standard Kalman filter can be applied to estimate the states of interest and also the covariance of the integration filter can be obtained.

2.5 Performance Analysis of the Integrated System

This study seeks accuracy improvement and continuity improvement. Based on the error characteristics of the WAAS, a simplified 1-D WAAS/INS example is first analyzed to obtain a general idea of the integration. A jamming and interference model for the analysis of continuity improvement is also described. Then, the performance improvement of the integrated WAAS/INS system is investigated.

2.5.1 Simplified 1-D WAAS/INS Example

This section considers a simplified WAAS/INS integrated system to obtain a complete picture of the effectiveness of the integration.

Consider a simplified one dimensional integrated system using an open-loop feed-forward structure, as presented in Fig. 2.10 . The simplified inertial system considered herein has a constant bias b ($25\mu G$, typical accelerometer bias value) for a navigation grade INS. Its state equation is shown as follows

$$\begin{bmatrix} \dot{x} \\ \dot{v} \\ \dot{b} \end{bmatrix} = \begin{bmatrix} 0 & 1 & 0 \\ 0 & 0 & 1 \\ 0 & 0 & 0 \end{bmatrix} \begin{bmatrix} x \\ v \\ b \end{bmatrix} \tag{2.11}$$

where x is the INS position error, and v is the INS velocity error.

The assumed WAAS measurement error comprises of a slow variation component x_{slow} and a fast variation component x_{fast}. The assumed WAAS error model and the

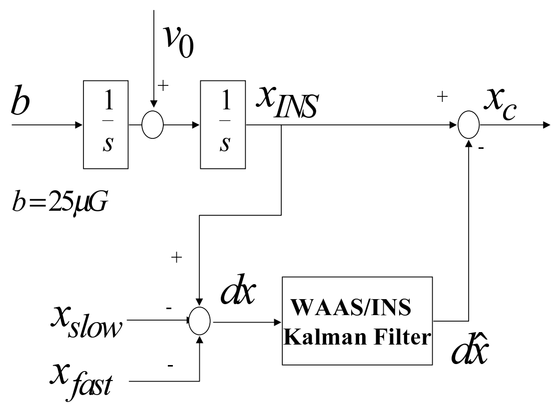

Figure 2.10: The Simplified 1-D WAAS/INS Error Integration System

derived WAAS error model share the same parameters in the East (E) direction. The WAAS error model is shown below.

$$x_{WAAS} = x_{slow} + x_{fast} \tag{2.12}$$

$$\begin{bmatrix} \dot{x}_{slow} \\ \dot{x}_{fast} \end{bmatrix} = \begin{bmatrix} \frac{-1}{\tau_{slow}} & 0 \\ 0 & \frac{-1}{\tau_{fast}} \end{bmatrix} \begin{bmatrix} x_{slow} \\ x_{fast} \end{bmatrix} + \begin{bmatrix} \frac{1}{\tau_{slow}} & 0 \\ 0 & \frac{1}{\tau_{fast}} \end{bmatrix} \begin{bmatrix} \nu_{slow} \\ \nu_{fast} \end{bmatrix} \tag{2.13}$$

where τ_{slow} is the time constant and ν_{slow} is the driving noise of the slow component; τ_{fast} is the time constant and ν_{fast} is the driving noise of the fast component.

For the integrated system, the independent dynamic equations of both the INS error and WAAS position error are combined into an augmented state equation and the measurement equation is derived by subtracting one from the other. The state equation and the measurement equation of the integrated system are shown below.

$$\begin{bmatrix} \dot{x} \\ \dot{v} \\ \dot{b} \\ \dot{x}_{slow} \\ \dot{x}_{fast} \end{bmatrix} = \begin{bmatrix} 0 & 1 & 0 & 0 & 0 \\ 0 & 0 & 1 & 0 & 0 \\ 0 & 0 & 0 & 0 & 0 \\ 0 & 0 & 0 & \frac{-1}{\tau_{slow}} & 0 \\ 0 & 0 & 0 & 0 & \frac{-1}{\tau_{fast}} \end{bmatrix} \begin{bmatrix} x \\ v \\ b \\ x_{slow} \\ x_{fast} \end{bmatrix} + \begin{bmatrix} 0 & 0 \\ 0 & 0 \\ 0 & 0 \\ \frac{1}{\tau_{slow}} & 0 \\ 0 & \frac{1}{\tau_{fast}} \end{bmatrix} \begin{bmatrix} \nu_{slow} \\ \nu_{fast} \end{bmatrix} \tag{2.14}$$

$$y = \begin{bmatrix} 1 & 0 & 0 & -1 & -1 \end{bmatrix} \begin{bmatrix} x \\ v \\ b \\ x_{slow} \\ x_{fast} \end{bmatrix} \tag{2.15}$$

Sensitivity analysis is conducted to analyze the performance improvement of the integrated system in relation to the time constant of the slow and fast components of the WAAS error. An optimal filter is considered to show the limitations of the integration and the linear covariance method is applied to evaluate the extent to which performance is improved. The performance improvement index defined herein is the percentage improvement of the standard deviation over the WAAS position error standard deviation as presented below.

$$\text{Improvement} = \frac{\sigma_{WAAS} - \sigma_{WAAS/INS}}{\sigma_{WAAS}} \times 100 \tag{2.16}$$

$$\sigma_{WAAS} = \sqrt{\sigma_{slow}^2 + \sigma_{fast}^2} \tag{2.17}$$

Parameters included in the sensitivity analysis are the time constants of the WAAS position error. Since, according to Eqn. 2.16, the magnitude of the driving noises has been normalized. Figure 2.11 summarizes the results of the sensitivity analysis. According to this figure, the vertical axis is the percentage improvement of the integrated system over the WAAS system. Two horizontal axes exist, the dotted line and the solid line. The dotted line denotes the variation of the time constant of the slow component, it ranges from 50 minutes to 400 minutes. Meanwhile, the solid line signifies the variation of the time constant of the fast component and it covers 25 minutes. Figure 2.11 depicts the corresponding performance improvement of the integrated system as below:

- Improvement versus the time constant of the *slow* component (dotted line): For the nominal time constant of the fast component, the accuracy improvement versus the variation of the time constant of the slow component is minimal (under 4%) and is insensitive to the variation of the time constant of the slow

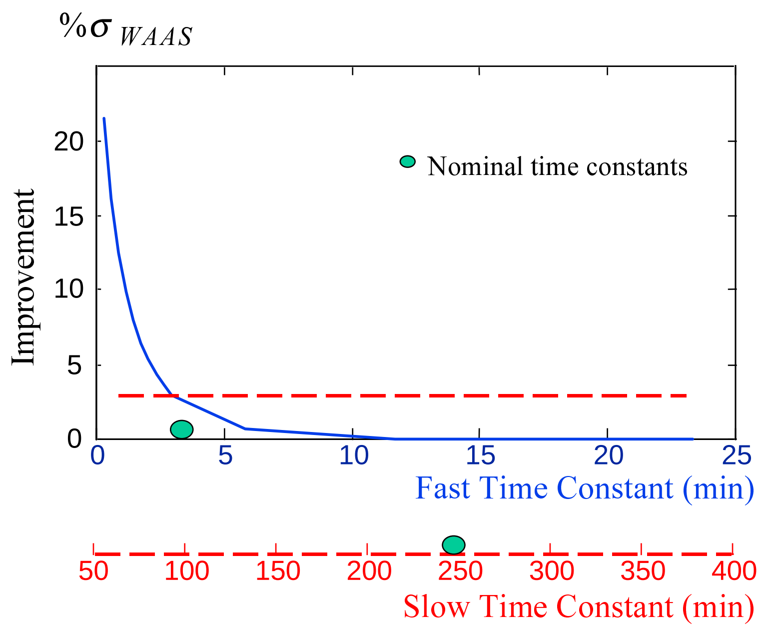

Figure 2.11: Effectiveness of the 1-D WAAS/INS Integration System

component.

- Improvement versus the time constant of the *fast* component (solid line): For the nominal time constant of the slow component, the accuracy improvement versus the variation of the time constant of the fast component becomes apparent when the time constant is small, e.g. under 2 minutes. Meanwhile, accuracy does not improve when the time constant of the fast component becomes larger, e.g. over 10 minutes.

Theses results are obtained using $b = 25\mu G$; therefore they are valid for typical navigation grade INS. The key results of the simplified 1-D WAAS/INS example are:

- Accuracy improvement becomes insignificant when the time constant of the fast component becomes larger, thus turning the fast component into a part of the slow component.

- The integration filter improves accuracy only minimally when the measurement has a very slow position error component like WAAS does.

Given the insight of the integration filter, when the identified WAAS position error model is applied to the integration filter below, only the variation of the fast component is considered.

2.5.2 The Interference and Jamming Model

The Minimum Operational Performance Standards (MOPS) for GPS/Wide-Area Augmentation System (WAAS) airborne equipment [WAASMOPS] specify an interference mask and minimum signal conditions that are valid for all phases of flight. Additionally, demodulated WAAS Word Error Rate (WER) requirements are also specified. Previous research [Schnaufer], [Hegarty], [Johnson] demonstrates that for both the specified in-band and out-of-band interference requirements, the WAAS MOPS compatible receiver has little or no performance margin for further interference sources, to say nothing of jamming sources. Such results create a need for modifying the receiver and/or interference requirements or aiding the WAAS with other navigation systems to provide a reasonable and achievable performance margin.

This chapter employs a replacement of WAAS outages to denote the presence of interference and/or jamming rather than employing an interference and jamming model. The allowable outage time with respect to the RNP for CAT I and II is investigated, with the integration of the WAAS and a navigation grade INS.

2.5.3 Simulation Setup

Sensitivity Analysis

Performance of the WAAS/INS integration filter is evaluated using the sensitivity analysis method. Sensitivity analysis is an efficient means of evaluating the performance of a suboptimal filter. A suboptimal filter does not include all the error source states but the major error states in the filter state [Nash], [Brown]. The integration filter specified in Section 2.4 is a suboptimal filter since it does not include all the

Table 2.3: Parameters of the Navigation Grade INS, LN-100

Accelerometer		Gyro	
Constant bias Bias stability Bias correlation time	25 μG 10 μG 1 hr	Constant drift Drift stability Drift correlation time	.0015 $°/hr$ .003 $°/hr$ 1 hr
Scale factor stability	50 ppm	Scale factor stability	1 ppm
Scale factor asymmetry	20 ppm	-	-
Misalignment	10 $\mu G/G$	Misalignment	1.5 $arc\ sec$
Nonlinearity	8 $\mu G/G^2$	-	-
Noise	5 $\mu G/\sqrt{Hz}$	Noise	.0008 $°/\sqrt{hr}$

error states of the inertial sensors and gravity anomaly. Also, the covariance of the integration filter does not represent the actual error statistics between the filter estimate and the true state. Because the Kalman gain, which is used to interact with the real-world systems, of the integration filter is computed using major error states (suboptimal states) instead of using all error states (true states.) To incorporate this effect, sensitivity analysis uses a truth model to describe the real-world system and then combines both the truth model and the filter to provide an actual covariance which describes the error statistics between the estimated state and the true state of the integrated system. Appendix B provides a detailed derivation of sensitivity analysis. Additionally, sensitivity analysis can provide the performance over a single error source. In the following WAAS/INS performance evaluation, the actual covariance is used.

The Truth Model

The truth model mathematically represents a real-world system. The truth model states include navigation states, inertial sensor states, gravity disturbance states and WAAS position error states. The inertial sensor states of the truth model include all the available error sources of the sensor. The navigation grade INS considered herein is the Litton LN-100. Table 2.3 summarizes parameters of the LN-100 obtained via phone request from Litton, where G denotes the nominal gravity.

With all the available sensor information, the sensor error states and their state equations can be expressed as follows

$$\begin{aligned}
\mathbf{x}_{sensor,t} &= \begin{bmatrix} \mathbf{x}^*_{sensor} & \mathbf{K1}^*_a & \alpha^*_a & \alpha^*_g & \mathbf{c}^*_a \end{bmatrix} \\
\dot{\mathbf{K1}}_a &= \mathbf{0} \\
\dot{\alpha}_a &= \mathbf{0} \\
\dot{\alpha}_g &= \mathbf{0} \\
\dot{\mathbf{c}}_a &= \mathbf{0}
\end{aligned} \tag{2.18}$$

where $\mathbf{K1}_a$ is the scale factor asymmetry vector of the accelerometer, α_a is the misalignment vector of the accelerometer, α_g is the misalignment vector of the gyro, and $\mathbf{c}_a$ is the nonlinearity vector of the accelerometer.

Gravity disturbance includes the gravity anomaly and the vertical deflection, both caused by the uneven distribution of the mass of the earth surface. The deviation of the actual gravity magnitude from the model is called the gravity anomaly while the deviation of the gravity vector direction from the normal to the geoid is the vertical deflection. The gravity disturbance states are

$$\delta\mathbf{g} = \begin{bmatrix} \delta g_N \\ \delta g_E \\ \delta g_D \end{bmatrix} = \begin{bmatrix} \xi G \\ -\eta G \\ \delta G \end{bmatrix} \tag{2.19}$$

where N, E and D denote the north, east and down components, respectively; ξ is the meridian deflection of the vertical, positive regarding east; η is the prime deflection of the vertical, positive regarding north; and δg is the gravity anomaly.

According to Levine [Levine], the meridian and the prime deflections can be modeled as a first order Gauss-Markov process with correlation distance of 25 NM (D_ξ) and 19 NM (D_η) and driving noise of 5.2 arc sec (σ_ξ) and 5.0 arc sec (σ_η) , respectively. The gravity anomaly can also be modeled as a first order Gauss-Markov process with a correlation distance of 20 NM ($D_{\delta G}$) and a driving noise of 25 μG ($\sigma_{\delta G}$). To incorporate the above two effects in the truth model, the spatial correlation (correlation distance) is transformed to a time correlation (time constant) by dividing by the vehicle's speed. The driving noise of the gravity disturbance in the north and the east direction is 25 μG and 24 μG, respectively, obtained by unit transformation. In sum, the gravity disturbance model can be expressed as

$$\delta\dot{\mathbf{g}} = \mathbf{F}_g \delta\mathbf{g} + \mathbf{G}_g \nu_g \tag{2.20}$$

where $\mathbf{F}_g = diag([\ \frac{-1}{\tau_N}\ \ \frac{-1}{\tau_E}\ \ \frac{-1}{\tau_D}\ ])$, $\tau_N = \frac{D_\xi}{v_N}$, $\tau_E = \frac{D_\eta}{v_E}$, $\tau_D = \frac{D_{\delta G}}{\sqrt{v_N^2+v_E^2}}$ and v_N, v_E are the vehicle's velocity in the north and the east direction; $\mathbf{G}_g = -\mathbf{F}_g$; ν_g is the driving noise vector of the gravity disturbance.

Incorporating the above effects, the truth model of the INS can be expressed as follows:

$$\begin{bmatrix} \dot{\mathbf{x}}_{nav} \\ \dot{\mathbf{x}}_{sensor,t} \\ \delta\dot{\mathbf{g}} \end{bmatrix} = \begin{bmatrix} \mathbf{F}_{nav} & \mathbf{F}_{ns,t} & \mathbf{F}_{ng} \\ \mathbf{0} & \mathbf{F}_{sensor,t} & \mathbf{0} \\ \mathbf{0} & \mathbf{0} & \mathbf{F}_g \end{bmatrix} \begin{bmatrix} \mathbf{x}_{nav} \\ \mathbf{x}_{sensor,t} \\ \delta\mathbf{g} \end{bmatrix} + \begin{bmatrix} \mathbf{G}_{nav} & \mathbf{0} \\ \mathbf{G}_{sensor,t} & \mathbf{0} \\ \mathbf{0} & \mathbf{G}_g \end{bmatrix} \begin{bmatrix} \upsilon_{sensor} \\ \nu_g \end{bmatrix} \tag{2.21}$$

where

$$\begin{aligned} \mathbf{F}_{ns,t} &= \begin{bmatrix} \mathbf{F}_{ns} & \begin{bmatrix} \mathbf{0} & \mathbf{0} & \mathbf{C}_b^e\mathbf{F}_{misa,g} & \mathbf{0} \\ \mathbf{0} & \mathbf{0} & \mathbf{0} & \mathbf{0} \\ \mathbf{C}_b^e\mathbf{F}_{K1,a} & \mathbf{C}_b^e\mathbf{F}_{misa,a} & \mathbf{0} & \mathbf{C}_b^e\mathbf{F}_{nonl,a} \end{bmatrix} \end{bmatrix} \\ \mathbf{F}_{ng} &= \begin{bmatrix} \mathbf{0} \\ \mathbf{0} \\ \mathbf{C}_l^e \end{bmatrix} \\ \mathbf{F}_{sensor,t} &= \begin{bmatrix} \mathbf{F}_{sensor} & \mathbf{0} \\ \mathbf{0} & \mathbf{0} \end{bmatrix} \\ \mathbf{G}_{sensor,t} &= \begin{bmatrix} \mathbf{G}_{sensor} \\ \mathbf{0} \end{bmatrix} \end{aligned} \tag{2.22}$$

and $\mathbf{F}_{misa,g}$=[ω_y $-\omega_z$ 0 0 0 0; 0 0 $-\omega_x$ ω_z 0 0;0 0 0 0 ω_x $-\omega_y$] is the corresponding body angular rate matrix to the gyro misalignment angles; $\mathbf{F}_{K1,a} = diag\left(sgn\left(\mathbf{f}^b\right)\right)$; $\mathbf{F}_{misa,a} = [f_y \ -f_z \ 0 \ 0 \ 0 \ 0; \ 0 \ 0 \ -f_x \ f_z \ 0 \ 0; \ 0 \ 0 \ 0 \ 0 \ f_x \ -f_y]$, is the corresponding body force matrix to the accelerometer misalignment angles; $\mathbf{F}_{nonl,a} = diag([\ f_x f_y \ f_y f_x \ f_z f_y])$ is the corresponding nonlinear force matrix to the accelerometer nonlinear effect; $\mathbf{C}_l^e$ is the transformation matrix from the local level frame to the e-frame.

Combining the truth model of the INS and the WAAS, the truth model of the integration filter is organized as follows

$$\begin{bmatrix} \dot{\mathbf{x}}_{nav} \\ \dot{\mathbf{x}}_{sensor,t} \\ \delta\dot{\mathbf{g}} \\ \delta\dot{\mathbf{x}}_{fast} \\ \delta\dot{\mathbf{x}}_{slow} \end{bmatrix} = \begin{bmatrix} \mathbf{F}_{nav} & \mathbf{F}_{ns,t} & \mathbf{F}_{ng} & \mathbf{0} & \mathbf{0} \\ \mathbf{0} & \mathbf{F}_{sensor,t} & \mathbf{0} & \mathbf{0} & \mathbf{0} \\ \mathbf{0} & \mathbf{0} & \mathbf{F}_g & \mathbf{0} & \mathbf{0} \\ \mathbf{0} & \mathbf{0} & \mathbf{0} & \mathbf{F}_{fast} & \mathbf{0} \\ \mathbf{0} & \mathbf{0} & \mathbf{0} & \mathbf{0} & \mathbf{F}_{slow} \end{bmatrix} \begin{bmatrix} \mathbf{x}_{nav} \\ \mathbf{x}_{sensor,t} \\ \delta\mathbf{g} \\ \delta\mathbf{x}_{fast} \\ \delta\mathbf{x}_{slow} \end{bmatrix} + \begin{bmatrix} \mathbf{G}_{nav} & \mathbf{0} & \mathbf{0} & \mathbf{0} \\ \mathbf{G}_{sensor,t} & \mathbf{0} & \mathbf{0} & \mathbf{0} \\ \mathbf{0} & \mathbf{G}_g & \mathbf{0} & \mathbf{0} \\ \mathbf{0} & \mathbf{0} & \mathbf{G}_{fast} & \mathbf{0} \\ \mathbf{0} & \mathbf{0} & \mathbf{0} & \mathbf{G}_{slow} \end{bmatrix} \begin{bmatrix} \upsilon_{sensor} \\ \nu_g \\ \nu_{fast} \\ \nu_{slow} \end{bmatrix} \tag{2.23}$$

Parameter Variations

To understand how the WAAS affects the performance of the integrated system , parameter variations of the WAAS position error model are considered. According to the conclusion of Section 2.5.1, only variations of the time constant and the driving noise of the fast component of the WAAS position error are investigated, and are listed in Table 2.4. Table 2.4 is designed to present a wide range of each parameter of the WAAS error. It covers the possible imperfect modeling and also can indicate the favorite or desired WAAS performance.

Table 2.4: Parameter Variations of the WAAS/INS Performance Evaluation

Parameter	**Variation**			
Time constant	$.25\tau_{fast}$	$.5\tau_{fast}$	$1\tau_{fast}$	$1.5\tau_{fast}$
Driving noise	$.25\sigma_{fast}$	$.5\sigma_{fast}$	$1\sigma_{fast}$	$1.5\sigma_{fast}$

2.5.4 WAAS/INS Performance

The performance of the WAAS/INS for the precision approach is evaluated by considering the trajectory of the last 10 minutes of an approach. According to Table 2.4, covariance of the WAAS/INS of 16 combinations of the time constant and driving noise is computed. In each case the covariance of the WAAS/INS integration is computed following the sensitivity analysis equations provided in Appendix B with the truth model and the filter model defined in Sections 2.5.3 and 2.4.

For the sensitivity of accuracy, discussed in the following, the extent to which accuracy is improved for each case is evaluated by comparing the position error standard deviation of the WAAS/INS with the WAAS position error itself at the end of the simulation. Results of all sixteen cases are presented in Fig. 2.12.

For the sensitivity of continuity, discussed in the following, the continuity improvement is evaluated by turning off the WAAS measurement update for 80 seconds at the end of the simulation, which uses the propagation equations as derived in Appendix B. Then, the allowable time for which the covariance of the system still satisfies the specified accuracy requirement is the improvement of the continuity. Results of all sixteen cases are presented in Fig. 2.13.

Detail explanations of Figs. 2.12 and 2.13 are given below.

Sensitivity of Accuracy

Figure 2.12 displays the sensitivity of the vertical error of the integrated WAAS/INS system with respect to the time constant and the driving noise of the fast component of the WAAS position error. The horizontal axis is the total WAAS position error σ_{WAAS} which is the root-sum-square of the driving noise of the slow and fast components. The variation of the σ_{WAAS} is attributed to the variation of the driving noise of the fast component. Each line denotes the simulation result of the variation of the time constant. Obviously, as shown in the top plot, the accuracy of the WAAS itself determines the accuracy of the WAAS/INS. A smaller time constant implies a more significant improvement. However, the accuracy improvement due to the smaller time constant of the fast component is only secondary, namely less than 10%, as displayed in the bottom plot of Fig. 2.12. For the nominal WAAS error, as the circle marked in Fig. 2.12, the accuracy improvement (less than 4%) is insignificant.

The results are explained as follows.

- Since the accuracy improvement of the integrated WAAS/INS is compared to the WAAS, the WAAS position error should be considered first. The WAAS uses the carrier smoothed code, with a carrier smoothing time constant of 100 seconds or more, as its signal processing algorithm to filter out the non-correlated noise (termed white noise) and provide a smooth but biased position.

- Furthermore, the known benefits of the integrated WAAS/INS system are as follows:

  - Filtering can smooth out the noisy measurements and obtain a smoother position output.
  - Meanwhile, proper modeling can estimate the biases of the INS and the WAAS error, thus improving the accuracy.

- In light of the above, since the WAAS alone is not noisy, the advantage of the integration filter to smooth out the noisy measurement is not apparent.
  The WAAS has both slow and fast errors; however, even the fast component is still too slow for the filter to estimate. Generally, the estimation becomes inefficient when the correlation time constant is above 2 minutes [Diesel]. For the nominal WAAS, the time constant of the fast component is about 3 minutes. Therefore, the efficiency of the WAAS bias estimation is not apparent.

Sensitivity of Continuity

The improvement of continuity is defined as the duration for which the position error continues to satisfy the required accuracy during WAAS outages while the integrated

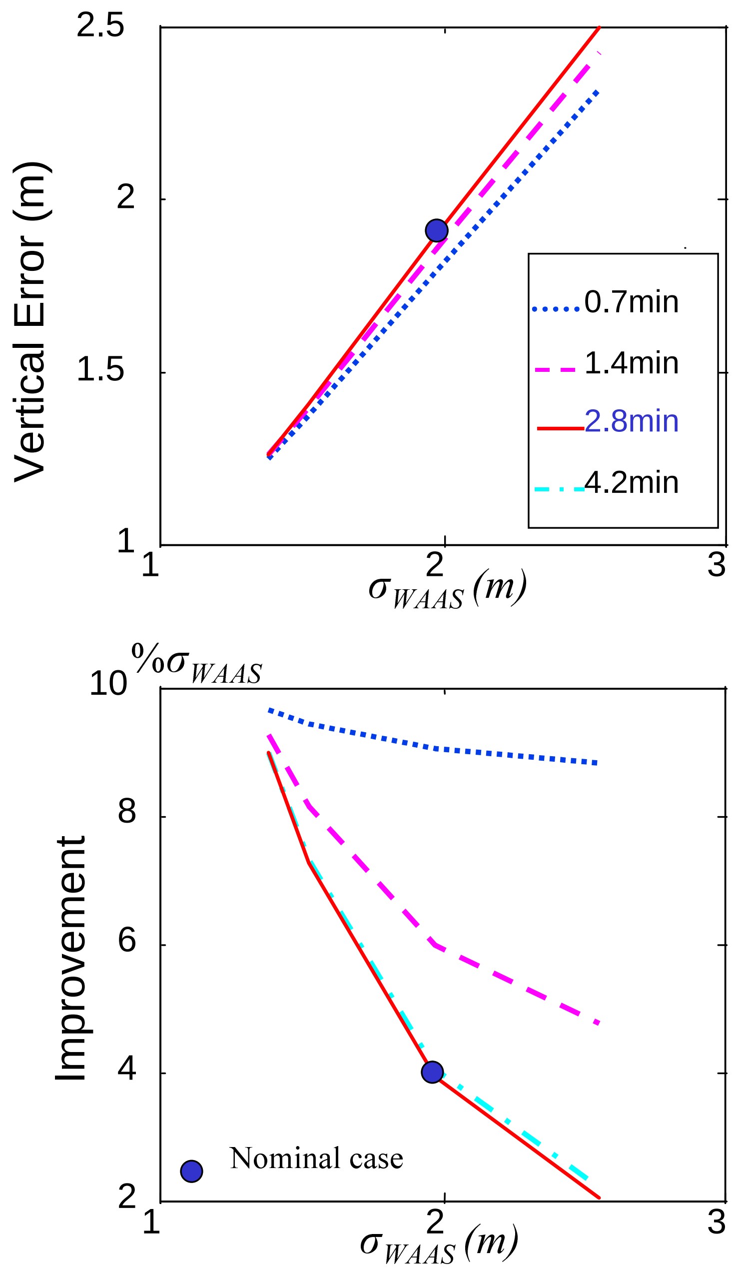

Figure 2.12: Sensitivity of Accuracy with respect to the Time Constant and the Driving Noise of the Fast Component

system navigates on the calibrated INS only. After the WAAS outage occurs, the INS alone performance is calculated using the propagation equations given in Appendix B and then examined by the 95% accuracy requirement of the CAT I and II to determine the improvement of continuity. Figure 2.13 displays the sensitivity of continuity of the integrated WAAS/INS system with respect to the time constant and the driving noise of the fast component of the WAAS position error. The horizontal axis is the total WAAS position error σ_{WAAS} which is the root-sum-square of the driving noise of the slow and fast components. The top plot of Fig. 2.13 shows the continuity improvement in relation to the CAT I requirement. The plot displays that, to comply with the CAT I accuracy requirement, the allowable WAAS outage time is dominated by the σ_{WAAS} and is insensitive to the time constant of the fast component. A smaller σ_{WAAS} implies a longer allowable outage time. This is explained as follows.

- Fig. 2.12 shows that, for a given σ_{WAAS} with 4 different time constants, the integrated position errors before the WAAS outage are nearly the same. This means that the position error at the starting point of INS alone is about the same. Then, for the same drifting property of the INS, the drifted position error is also insensitive to the variation of the time constant of the fast component. This explains why 4 lines in Fig. 2.13 are close to each other.

For the nominal WAAS, integrating the WAAS with a navigation grade INS can allow 40 seconds of WAAS outage. The time gained from the improved continuity is valuable to the pilot to handle WAAS outage situations and may be helpful to the airport administration to isolate the local interference and/or jamming sources.

It is interesting to know the potential of the integrated WAAS/INS system to achieve the CAT II 95% accuracy and the possible continuity improvement suggested by J. Diesel, though WAAS alone is not a CAT II system yet (partially because of the time to alarm requirement). The bottom plot of Fig. 2.13 shows the result of all sixteen cases examined by the CAT II 95% accuracy requirement. It displays that, for the nominal WAAS position error, the integrated WAAS/INS system does not satisfy the CAT II requirement. Therefore, no WAAS outage is allowed. Simultaneously, WAAS/INS are known to be capable of satisfying the CAT II requirements only if

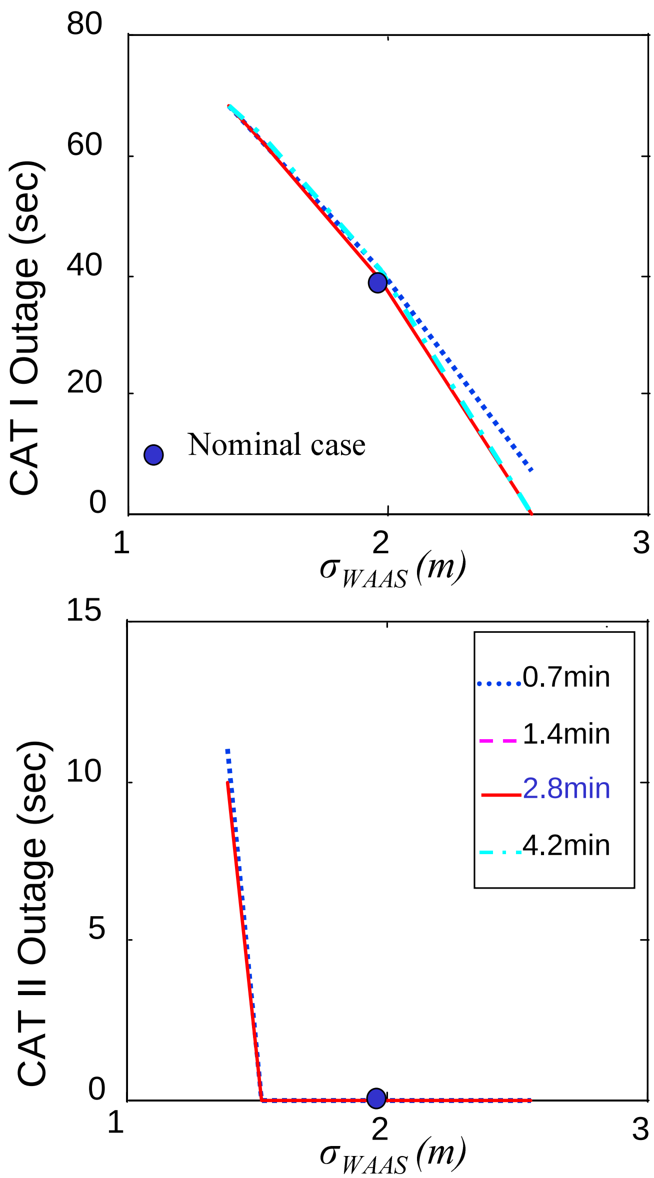

Figure 2.13: Sensitivity of Continuity with respect to the Time Constant and the Driving Noise of the Fast Component

the WAAS alone fulfills the CAT II requirements.

2.6 Summary

Using the WAAS error model derived from the NSTB WAAS data, this study provides new performance limitations of the WAAS/INS. The following summarizes the discovery from the performance investigation of the integrated WAAS/INS system.

- Due to the slow component of the WAAS position error, the accuracy of the WAAS/INS system over the WAAS system is not significantly improved.
- Due to the calibration of the INS sensor error, the integrated system provides continuity (up to 40 seconds) for the CAT I precision approach when WAAS outages occur. The time gained from the improved continuity is valuable to the pilot to handle WAAS outage situations.
- The integrated WAAS/INS system cannot extend the accuracy to meet the CAT II 95% vertical accuracy requirement, since the accuracy is dominated by the WAAS position error. Restated, the WAAS/INS system can meet the CAT II 95% vertical accuracy requirement only if the WAAS itself satisfies the CAT II requirement.

Chapter 3

Integration of the LAAS with an INS

Integrating the DGPS with an INS to enhance accuracy and continuity during GPS outage or masking is a common practice in the integration field. However, the accuracies of the integrated system and LAAS using the carrier phase algorithm have not been compared. This chapter focuses on the differences in accuracy between the LAAS/INS and LAAS using different algorithms during GPS outage or masking. A tightly coupled integration structure is considered for the LAAS/INS integration [Bose]. Herein, tightly coupled implies that the integration is in the pseudorange and/or carrier phase domain as opposed to in the position domain. Investigated LAAS algorithms include the CSC, the Code and Carrier Update (CCU) method [Lawrence, a], and the Carrier Phase Riding (CPR) [Hwang] method which uses the incremental carrier phase to propagate position.

LAAS uses the reference station to generate carrier smoothed pseudorange corrections. Even though it is not required for CAT I approaches (may also not be required for CAT III in the future), carrier phase corrections can also be available. In this chapter, it is assumed that both corrections are available. Then LAAS uplinks these corrections to the roving user to eliminate the common mode errors. These corrections significantly improve the position of the airborne user. However, the position still incurs residual errors caused by the time and/or spatial decorrelations and by local environmental reflections (multipaths). According to Parkinson [Parkinson, a], a conservative estimate of the filtered DGPS range error, which is dominated by the multipath, for users within 50 km of the reference station is about 1.1 m. Considering this effect, the following analysis treats the multipath as the main error source and includes experimental data based multipath models of both the reference station and the airborne user.

Below, the related equations for the DGPS/INS integration are given, error equations for the CSC, the CCU and the CPR are derived, the multipath model of both the reference station and the user is described, the simulation setup is discussed, and the performance comparison is conducted.

In terms of the integration, DGPS and LAAS do not differ significantly. Both approaches provide differential corrections to the user. Therefore, this chapter uses the two terms interchangeably.

3.1 Integration of the Differential GPS and an INS

To develop the equation of the integrated system, it is easier to start with the DGPS measurement, then move on to the integration.

3.1.1 DGPS Measurements

Figure 3.1 depicts the geometry of the DPGS problem where $\mathbf{x}_{ref}$ denotes the position vector of the reference station; $\mathbf{r}_{ins}$ denotes the position output of the INS; $\mathbf{x}_{sv}$ denotes the position vector of the satellite; $\mathbf{x}$ is the true position of the aircraft in the local area coordinate system; $\mathbf{x}_{ins}$ is the position vector of the INS with respect to the local area coordinate system; $\delta\mathbf{x}_{ins}$ denotes the position error of the INS; S_j^i is the range between the j^{th} satellite and the i^{th} user; i denotes either the ground (g) receiver or the airborne user (a) receiver; R_j is the range difference of the j^{th} satellite between the airborne user and the ground reference station; and $\mathbf{e}_j$ is the line-of-sight vector to the j^{th} satellite.

The pseudorange (ρ) and the carrier phase (ϕ) measurements for the jth satellite

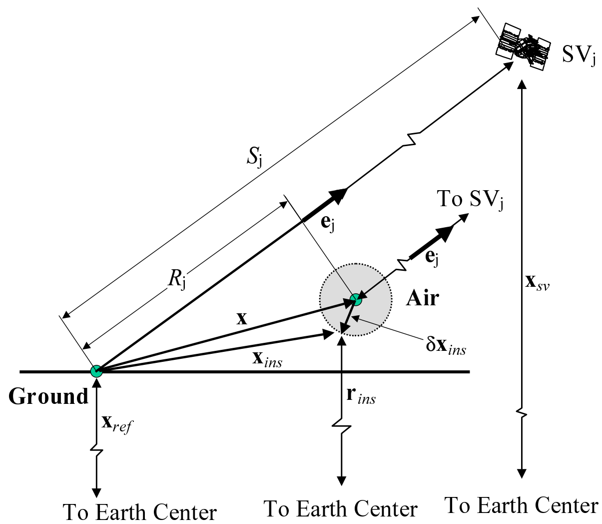

Figure 3.1: Geometric Relation of the DGPS

of the ith receiver at the kth epoch are given by

$$\rho^i_{j,k} = S^i_{j,k} + b^i_k - B_{j,k} + I^i_{j,k} + T^i_{j,k} + m^i_{j,k} + \nu^i_{j,k} \quad (3.1)$$

$$\phi^i_{j,k} = S^i_{j,k} + b^i_k - B_{j,k} - I^i_{j,k} + T^i_{j,k} + N^i_j + m^{\phi i}_{j,k} + \nu^{\phi i}_{j,k} \quad (3.2)$$

where b is the receiver clock; B denotes the satellite clock; I represents the ionosphere delay; T is the troposphere delay; m denotes the multipath; ν is the receiver thermal noise; and N represents the integer cycle ambiguity of the carrier phase.

Differential measurements are obtained by subtracting the ground measurements from the airborne measurements:

$$\rho_{j,k} = R_{j,k} + b_{uk} + \left(m^a_{j,k} - m^g_{j,k}\right) + \left(\nu^a_{j,k} - \nu^g_{j,k}\right) \quad (3.3)$$

$$\phi_{j,k} = R_{j,k} + b_{uk} + N_j + \left(m^{\phi a}_{j,k} - m^{\phi g}_{j,k}\right) + \left(\nu^{\phi a}_{j,k} - \nu^{\phi g}_{j,k}\right) \quad (3.4)$$

where

$$\rho_{j,k} \triangleq \rho^a_{j,k} - \rho^g_{j,k} = \text{The differential pseudorange measurement.}$$

$$R_{j,k} \triangleq R^a_{j,k} - R^g_{j,k} = \text{The range difference between the two receivers from the satellite.}$$

$$b_{uk} \triangleq b^a_k - b^g_k = \text{The difference between the receiver clock biases, plus the difference between receiver line biases.}$$

$$\phi_{j,k} \triangleq \phi^a_{j,k} - \phi^g_{j,k} = \text{The differential carrier phase measurement.}$$

$$N_j \triangleq N^a_j - N^g_j = \text{The difference between the receiver integer cycle ambiguities.}$$

Since the multipath of the differential carrier phase is considerably smaller than that of the differential code phase, its contribution to the position error can be ignored without affecting the accuracy of the comparison of all the algorithms. Therefore, the differential multipath term in Eqn. 3.4 is neglected in the following, and Eqn. 3.4 can be rewritten as

$$\phi_{j,k} = R_{j,k} + b_{uk} + N_j + \left(\nu^{\phi a}_{j,k} - \nu^{\phi g}_{j,k}\right). \tag{3.5}$$

Geometry (as shown in Fig. 3.1) is a relatively easy means of showing that the range difference is

$$R_{j,k} = -\mathbf{e}^*_{j,k}\mathbf{x}_k \tag{3.6}$$

where $\mathbf{e}_{j,k}$ is the line-of-sight vector toward the jth satellite; and $\mathbf{x}_k$ is the aircraft position with respect to the local reference station.

Define the four-dimensional state (position and clock bias) of the airborne user as

$$\mathbf{X}_k \triangleq \begin{bmatrix} \mathbf{x}_k \\ b_{uk} \end{bmatrix}.$$

The vector form of Eqns. 3.3 and 3.5 can be written in the normal equation form as

$$\begin{aligned} \rho_k &= \mathbf{H}_k\mathbf{X}_k + (\mathbf{m}^a_k - \mathbf{m}^g_k) + (\nu^a_k - \nu^g_k) &(3.7)\\ \phi_k &= \mathbf{H}_k\mathbf{X}_k + \mathbf{N} + \left(\nu^{\phi a}_k - \nu^{\phi g}_k\right) &(3.8) \end{aligned}$$

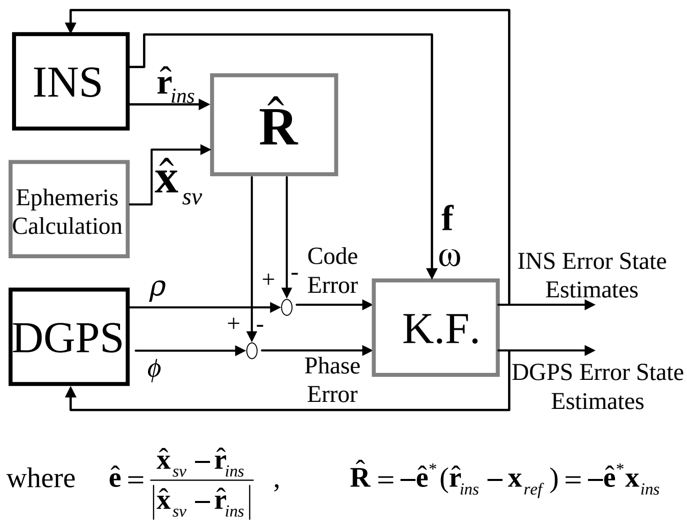

Figure 3.2: Block Diagram of a Tightly Coupled DGPS/INS Integration. $\frown$ means the estimate of that variable.

where

$$\mathbf{H}_k = \begin{bmatrix} -\mathbf{e}^*_{1,k} & 1 \\ \vdots & \vdots \\ -\mathbf{e}^*_{n,k} & 1 \end{bmatrix}$$

is the geometry matrix and n is the number of satellites; $\mathbf{m}$ and ν are the vector form of the multipath and the noise.

3.1.2 The Integration

A tightly coupled integration structure [Bose] used is shown in Fig. 3.2, where symbol $\frown$ means the estimate of that variable. Figure 3.2 Figure 3.2 indicates that the estimate of range $\left(\widehat{R}_{j,k}\right)$ can be written as

$$\begin{aligned}
\widehat{R}_{j,k} &= -\widehat{\mathbf{e}}^*_{j,k}\mathbf{x}_{ins,k} && (3.9)\\
&= -\mathbf{e}^*_{j,k}\mathbf{x}_k - \tilde{\mathbf{e}}^*_{j,k}\mathbf{x}_k - \mathbf{e}^*_{j,k}\delta\mathbf{x}_{ins,k} - \tilde{\mathbf{e}}^*_{j,k}\delta\mathbf{x}_{ins,k} && (3.10)\\
&\cong -\mathbf{e}^*_{j,k}\mathbf{x}_k - \tilde{\mathbf{e}}^*_{j,k}\mathbf{x}_k - \mathbf{e}^*_{j,k}\delta\mathbf{x}_{ins,k} && (3.11)\\
&\cong R_{j,k} - \tilde{\mathbf{e}}^*_{j,k}\mathbf{x}_k - \mathbf{e}^*_{j,k}\delta\mathbf{x}_{ins,k} && (3.12)
\end{aligned}$$

where

$$\begin{aligned}
\widehat{\mathbf{e}}_{j,k} &= \mathbf{e}_{j,k} + \tilde{\mathbf{e}}_{j,k} && (3.13)\\
\mathbf{x}_{ins,k} &= \mathbf{x}_k + \delta\mathbf{x}_{ins,k}. && (3.14)
\end{aligned}$$

The maximum order of magnitude of $\tilde{\mathbf{e}}^*_{j,k}\mathbf{x}_{ins,k} \approx 10^{-7} \times 10^4 \sim 1mm$. This magnitude decreases as the aircraft approaches the airport, making it negligible in this application.

Differential observables of the filter can be written as

$$\begin{aligned}
y^{\rho}_{j,k} &= \rho_{j,k} - \widehat{R}_{j,k} && (3.15)\\
&= \mathbf{e}^*_{j,k}\delta\mathbf{x}_{ins,k} + b_{uk} + \left(m^a_{j,k} - m^g_{j,k}\right) + \left(\nu^a_{j,k} - \nu^g_{j,k}\right) && (3.16)\\
y^{\phi}_{j,k} &= \phi_{j,k} - \widehat{R}_{j,k} && (3.17)\\
&= \mathbf{e}^*_{j,k}\delta\mathbf{x}_{ins,k} + b_{uk} + N_j + \left(\nu^{\phi a}_{j,k} - \nu^{\phi g}_{j,k}\right). && (3.18)
\end{aligned}$$

where $j = 1 \cdots n$ and n is the number of in-view satellites.

In Eqns. 3.16 and 3.18, the user clock error b_{uk} is common to all measurements. Generally, it can be modeled as a 2-state Kalman filter model [van Dierendonck]. However, precise clock parameters for each individual receiver to propagate during GPS satellite outage are unavailable. One way of eliminating the differential user clock b_{uk} is to use the double difference implementation (DDI) of the satellite measurements which is the difference among satellites. The drawback of the DDI is the increased measurement noise, implying that the integration filter may take longer to smooth out the noise. However, within the time frame of an approach, sufficient time is available for the integration filter to smooth out the increased measurement noise. Hence, DDI is considered herein.

The normal equation form of the observable equation can be formed by defining

$$\delta \mathbf{y}_k \triangleq \begin{bmatrix} \delta y_{l,k}^{\rho} \\ \delta y_{l,k}^{\phi} \end{bmatrix}_{l=1\cdots n-1} \tag{3.19}$$

$$= \begin{bmatrix} y_{2,k}^{\rho} - y_{1,k}^{\rho} & \cdots & y_{n,k}^{\rho} - y_{1,k}^{\rho} & y_{2,k}^{\phi} - y_{1,k}^{\phi} & \cdots & y_{nSV,k}^{\phi} - y_{1,k}^{\phi} \end{bmatrix}^T \tag{3.20}$$

$$\Delta \mathbf{e}_{l,k} \triangleq (\mathbf{e}_{j,k} - \mathbf{e}_{1,k})_{j=2\cdots n} \tag{3.21}$$

$$\Delta N_l \triangleq (N_j - N_1)_{j=2\cdots n}. \tag{3.22}$$

Note: $l = 1 \cdots n - 1$. Because of the double difference, following the above definition obtains

$$\delta \mathbf{y}_k = \begin{bmatrix} \Delta \mathbf{e}_{1,k}^{*} \delta \mathbf{x}_{ins,k} + (m_2^a - m_2^g)_k - (m_1^a - m_1^g)_k + (\nu_2^a - \nu_2^g)_k - (\nu_1^a - \nu_1^g)_k \\ \vdots \\ \Delta \mathbf{e}_{1,k}^{*} \delta \mathbf{x}_{ins,k} + \Delta N_l + \left(\nu_{2,k}^{\phi a} - \nu_{2,k}^{\phi g}\right) - \left(\nu_{1,k}^{\phi a} - \nu_{1,k}^{\phi g}\right) \\ \vdots \end{bmatrix}. \tag{3.23}$$

Therefore, the normal equation of the differential observables can be written as

$$\delta \mathbf{y}_k = \mathbf{H}_{insgps,k} \mathbf{X}_{insgps,k} + \mathbf{J}_{insgps,k} \mathbf{v}_{insgps,k} \tag{3.24}$$

where

$$\mathbf{H}_{insgps,k} = \begin{bmatrix} \mathbf{H}_k^i & \mathbf{H}^\rho & \mathbf{0} \\ \mathbf{H}_k^i & \mathbf{0} & \mathbf{H}^{\Delta N} \end{bmatrix} \tag{3.25}$$

$$\mathbf{X}_{insgps,k} = \begin{bmatrix} \mathbf{X}_k^i \\ \mathbf{X}_k^\rho \\ \mathbf{X}_k^{\Delta N} \end{bmatrix} \tag{3.26}$$

$$\mathbf{J}_{insgps,k} = \begin{bmatrix} \mathbf{J}^\rho & \mathbf{0} \\ \mathbf{0} & \mathbf{J}^{\Delta N} \end{bmatrix} \tag{3.27}$$

$$\mathbf{v}_{insgps,k} = \begin{bmatrix} \mathbf{v}_k^\rho \\ \mathbf{v}_k^\phi \end{bmatrix} \tag{3.28}$$

$$
\begin{aligned}
\mathbf{H}_k^i &= \begin{bmatrix} \mathbf{0} & (\mathbf{e}_{2,k}-\mathbf{e}_{1,k})^T & \mathbf{0} & \mathbf{0} & \mathbf{0} \\ \vdots & \vdots & \vdots & \vdots & \vdots \\ \mathbf{0} & (\mathbf{e}_{n,k}-\mathbf{e}_{1,k})^T & \mathbf{0} & \mathbf{0} & \mathbf{0} \end{bmatrix}_{n-1\times n_{INS}} && (3.29) \\
\mathbf{H}^\rho &= \begin{bmatrix} -1 & 1 & 1 & -1 & 0 & 0 & \cdots & \cdots & 0 & 0 \\ -1 & 1 & 0 & 0 & 1 & -1 & & & \vdots & \vdots \\ \vdots & \vdots & \vdots & \vdots & & & \ddots & \ddots & 0 & 0 \\ -1 & 1 & 0 & 0 & \cdots & \cdots & 0 & 0 & 1 & -1 \end{bmatrix}_{n-1\times 2n} && (3.30) \\
\mathbf{H}^{\Delta N} &= \begin{bmatrix} 1 & 0 & \cdots & 0 \\ 0 & 1 & \ddots & \vdots \\ \vdots & \ddots & \ddots & 0 \\ 0 & \cdots & 0 & 1 \end{bmatrix}_{n-1\times n-1} && (3.31) \\
\mathbf{X}_k^i &= \begin{bmatrix} \varepsilon_k^T & \delta\mathbf{x}_{ins,k}^T & \delta\mathbf{v}_k^T & \mathbf{b}_k^T & \mathbf{d}_k^T \end{bmatrix}_{n_{INS}\times 1}^T && (3.32) \\
\mathbf{X}_k^\rho &= \begin{bmatrix} m_{1,k}^a & m_{1,k}^g & m_{2,k}^a & m_{2,k}^g & \cdots & \cdots & m_{n,k}^a & m_{n,k}^g \end{bmatrix}_{2n\times 1}^T && (3.33) \\
\mathbf{X}^{\Delta N} &= \begin{bmatrix} \Delta N_{1,k} & \cdots & \Delta N_{n-1,k} \end{bmatrix}_{n-1\times 1}^T && (3.34) \\
\mathbf{J}^\rho &= \begin{bmatrix} -1 & 1 & 0 & \cdots & 0 \\ -1 & 0 & 1 & \ddots & \vdots \\ \vdots & \vdots & \ddots & \ddots & 0 \\ -1 & 0 & \cdots & 0 & 1 \end{bmatrix}_{n-1\times n} && (3.35) \\
\mathbf{J}^{\Delta N} &= \mathbf{J}^\rho && (3.36) \\
\mathbf{v}_k^\rho &= \begin{bmatrix} v_{1,k}^a - v_{1,k}^g & \cdots & v_{n,k}^a - v_{n,k}^g \end{bmatrix}_{n\times 1}^T && (3.37) \\
\mathbf{v}_k^\phi &= \begin{bmatrix} v_{1,k}^{\phi a} - v_{1,k}^{\phi g} & \cdots & v_{n,k}^{\phi a} - v_{n,k}^{\phi g} \end{bmatrix}_{n\times 1}^T . && (3.38)
\end{aligned}
$$

Notably, in Eqn. 3.24, all terms are coordinate independent, except for the $\Delta\mathbf{e}_{1,k}\delta\mathbf{x}_{ins,k}$ term which is coordinate related. Restated, only the consistence of the coordinate frame between $\Delta\mathbf{e}_{1,k}$ and $\delta\mathbf{x}_{ins,k}$ must be considered.

3.2 DGPS Algorithms

3.2.1 Carrier Smoothed Code

As the code phase measurement is noisy, the carrier phase can be used to smooth the code phase measurement and thus obtain a smoother position. The Hatch filter [Hatch] for the carrier smoothing is given by

$$\hat{\rho}_{j,k} = \frac{L-1}{L}\left(\hat{\rho}_{j,k-1} + \phi_{j,k} - \phi_{j,k-1}\right) + \frac{1}{L}\rho_{j,k} \tag{3.39}$$

where $\hat{\rho}$ is the filtered pseudorange; L is the carrier smoothing time constant usually 100 or 200 seconds. The Weighted Least Squares (WLS) position [Kailath] of Eqn. 3.7 with the carrier smoothed code $\hat{\rho}_k$ can be expressed as

$$\hat{\mathbf{X}}_k = \left(\hat{\mathbf{H}}_k^* \mathbf{W}_k \hat{\mathbf{H}}_k\right)^{-1} \hat{\mathbf{H}}_k^* \mathbf{W}_k \hat{\rho}_k \tag{3.40}$$

where $\hat{\mathbf{X}}_k$ is the estimate of $\mathbf{X}_k$; $\hat{\mathbf{H}}_k$ is the estimate of $\mathbf{H}_k$ with estimated LOS $\hat{\mathbf{e}}_{j,k}$ inside; $\mathbf{W}_k$ is a diagonal weighting matrix. In this case, the diagonal entry of $\mathbf{W}_k$ is the inverse of the sum of the variance of the carrier smoothed multipaths, including the ground and air. With the known weighting matrix (either from the carrier smoothed multipaths or the lumped pseudorange versus the elevation relation, which is discussed in Section 3.3), the estimation error covariance of the position and the clock can be expressed as [Kailath]

$$E\left(\tilde{\mathbf{X}}_k \tilde{\mathbf{X}}_k^*\right) = \left(\hat{\mathbf{H}}_k^* \mathbf{W}_k \hat{\mathbf{H}}_k\right)^{-1}. \tag{3.41}$$

To calculate the $\mathbf{W}_k$, a model-based carrier smoothed multipath can be derived as follows.

- Assume that the multipath is a first order Gauss-Markov process as

$$m_{i+1} = c m_i + \upsilon_i^m \tag{3.42}$$

where m represents the multipath, c is the coefficient and υ^m is the driving noise of the first order Gauss-Markov process.

- The carrier smoothed multipath can be expressed as

$$x_{i+1} = a(x_i + \upsilon^{\phi}_{i+1} - \upsilon^{\phi}_i) + b(m_{i+1} + \upsilon^{\rho}_{i+1}) \tag{3.43}$$

where x is the smoothed multipath; υ^{ϕ} is the carrier phase noise and υ^{ρ} is the code phase noise.

- State space form:

Combining the above two equations, the state space form is obtained as

$$\begin{bmatrix} \upsilon^{\phi}_{i+1} \\ m_{i+1} \\ x_{i+1} \end{bmatrix} = \begin{bmatrix} 0 & 0 & 0 \\ 0 & c & 0 \\ -a & bc & a \end{bmatrix} \begin{bmatrix} \upsilon^{\phi}_{i} \\ m_{i} \\ x_{i} \end{bmatrix} + \begin{bmatrix} 1 & 0 & 0 \\ 0 & 1 & 0 \\ a & b & b \end{bmatrix} \begin{bmatrix} \upsilon^{\phi}_{i+1} \\ \upsilon^{m}_{i} \\ \upsilon^{\rho}_{i+1} \end{bmatrix} \tag{3.44}$$

or in short,

$$X_{i+1} = FX_i + GU_i.$$

Therefore, the covariance of the carrier smoothed multipath can be expressed as

$$P_{i+1} = FP_iF^* + GE(U_iU_i^*)G^* \tag{3.45}$$

where

$$E(U_iU_i^*) = \begin{bmatrix} \sigma^2_{\upsilon^{\phi}} & 0 & 0 \\ 0 & \sigma^2_{\upsilon^{m}} & 0 \\ 0 & 0 & \sigma^2_{\upsilon^{\rho}} \end{bmatrix}. \tag{3.46}$$

Applying Eqn. 3.45 to both the ground and the air multipaths and taking the

(3,3) element of the P_{i+1} matrix for each satellite, the diagonal entry of the weighting matrix $\mathbf{W}_k$ can be determined and, with it, the estimation error of the position and clock bias.

3.2.2 Code and Carrier Update (CCU)

As the carrier phase has an integer cycle ambiguity, which causes a very poor initial position, the code phase measurement can be used to initialize N. The carrier phase is much cleaner than the code phase. Thus, when more than four satellites are in view, the satellite motion may improve the estimate of the N and thus obtain a better position [Lawrence, a]. Equations of the CCU are given below.

Positioning

- State equation:
  - Knowing that $\mathbf{N}$ will not change if the phase lock of the receiver holds.
  - Modeling the multipath of the code phase and the carrier phase properly (usually uses the Gauss-Markov process.)

  Therefore, these equations can be organized as follows.

$$\begin{aligned} \mathbf{N}_{k+1} &= \mathbf{N}_k \\ \mathbf{m}^a_{k+1} &= \mathbf{F}^a_{mlt,k}\mathbf{m}^a_k + \mathbf{G}^a_{mlt,k}\mathbf{u}^a_k \\ \mathbf{m}^g_{k+1} &= \mathbf{F}^g_{mlt,k}\mathbf{m}^g_k + \mathbf{G}^a_{mlt,k}\mathbf{u}^g_k \end{aligned} \tag{3.47}$$

- Update equations:
  - Referring to Eqns. 3.8 and 3.7, the code phase update can be written as below:

$$\phi_k - \rho_k = \mathbf{N} - (\mathbf{m}^a_k - \mathbf{m}^g_k) + \left(\nu^{\phi a}_k - \nu^{\phi g}_k\right) - (\nu^a_k - \nu^g_k)\,. \tag{3.48}$$

    The dominant error source is the code phase multipath $\mathbf{m}_k$ and noise ν_k.

– Carrier phase update equation, Eqn. 3.8, can be modified by

$$\begin{aligned} \mathbf{L}_k\phi_k &= \mathbf{L}_k\mathbf{H}_k\mathbf{X}_k + \mathbf{L}_k\mathbf{N} + \mathbf{L}_k\left(\nu_k^{\phi a} - \nu_k^{\phi g}\right) && (3.49)\\ &= \mathbf{L}_k\mathbf{N} + \mathbf{L}_k\left(\nu_k^{\phi a} - \nu_k^{\phi g}\right) && (3.50)\end{aligned}$$

where $\mathbf{L}_k$ is the left null space of the satellite geometry matrix $\mathbf{H}_k$, so $\mathbf{L}_k\mathbf{H}_k = \mathbf{0}$. The carrier phase update uses the variation of the satellite geometry, i.e. the time variant $\mathbf{L}_k$, to estimate $\mathbf{N}$.

Combining the code update (Eqn. 3.48) and the carrier update (Eqn. 3.50), the integer cycle ambiguity can be estimated by

$$\begin{aligned} \mathbf{y}_k &= \begin{bmatrix} \mathbf{L}_k\phi_k \\ \phi_k - \rho_k \end{bmatrix} \\ &= \begin{bmatrix} \mathbf{L}_k\mathbf{N} + \mathbf{L}_k\left(\nu_k^{\phi a} - \nu_k^{\phi g}\right) \\ \mathbf{N} - \left(\mathbf{m}_k^a - \mathbf{m}_k^g\right) + \left(\nu_k^{\phi a} - \nu_k^{\phi g}\right) - \left(\nu_k^a - \nu_k^g\right) \end{bmatrix}. && (3.51)\end{aligned}$$

- CCU positioning:

  Rearranging the state equation and the update equation into the state-space form and using the standard Kalman filter obtains $\hat{\mathbf{N}}$, the estimate of $\mathbf{N}$, and its covariance $\mathbf{P}_{\mathbf{N}}$. With the $\hat{\mathbf{N}}$, the position can be estimated by

$$\phi_k - \hat{\mathbf{N}} = \hat{\mathbf{H}}_k\hat{\mathbf{X}}_k. \tag{3.52}$$

  Therefore, the CCU positioning can be expressed as

$$\hat{\mathbf{X}}_k = \left(\hat{\mathbf{H}}_k^*\mathbf{W}_k\hat{\mathbf{H}}_k\right)^{-1}\hat{\mathbf{H}}_k^*\mathbf{W}_k\left(\phi_k - \hat{\mathbf{N}}\right). \tag{3.53}$$

  The next section will give $\mathbf{W}_k$.

- Notably, with respect to the CSC and the CCU: For the CCU, code phase update alone essentially provides the same accuracy as the CSC. For the code phase update, Kalman filter estimates the $\mathbf{N}$ by averaging the multipaths and noises in the code phase update. According to [Gazit], in this case, the Kalman gain is $\frac{1}{k}$, where k represents the number of the epochs of the running filter. Therefore, when $k = L$ the code phase only update provides the same result as the CSC. When $k > L$ the code phase update appears to have a longer averaging time, which should provide better accuracy. However, since the multipath is a gradually changing process, the results of these two methods only slightly differ when L is large, e.g. 100 or 200.

CCU Positioning Error

Plugging Eqn. 3.8 into Eqn. 3.52, produces:

$$\mathbf{H}_k\mathbf{X}_k + \mathbf{N} + \left(\nu_k^{\phi a} - \nu_k^{\phi g}\right) - \hat{\mathbf{N}} = \hat{\mathbf{H}}_k\hat{\mathbf{X}}_k. \tag{3.54}$$

Reorganizing Eqn. 3.54, the error of the position estimate can be expressed as:

$$\tilde{\mathbf{X}}_k = \left(\hat{\mathbf{H}}_k^*\mathbf{W}_k\hat{\mathbf{H}}_k\right)^{-1}\hat{\mathbf{H}}_k^*\mathbf{W}_k\left(\left(\nu_k^{\phi a} - \nu_k^{\phi g}\right) - \tilde{\mathbf{N}}\right) \tag{3.55}$$

where $\tilde{\mathbf{x}}_k = \hat{\mathbf{x}}_k - \mathbf{x}_k$, $\tilde{b}_{uk} = \hat{b}_{uk} - b_{uk}$, $\tilde{\mathbf{N}}_k = \hat{\mathbf{N}} - \mathbf{N}$.

The covariance matrix of the position error is $\Sigma_{\tilde{\mathbf{x}}} = E\left(\tilde{\mathbf{X}}_k\tilde{\mathbf{X}}_k^*\right) = \left(\hat{\mathbf{H}}_k^*\mathbf{W}_k\hat{\mathbf{H}}_k\right)^{-1}$, where

$$\mathbf{W}_k = \left[\Sigma_{\nu^{\phi a}} + \Sigma_{\nu^{\phi g}} + \mathbf{P}_{\mathbf{N}}\right]^{-1} \tag{3.56}$$

and $\Sigma_{\nu^{\phi a}} = E\left(\nu^{\phi a}\nu^{\phi a *}\right)$, $\Sigma_{\nu^{\phi g}} = E\left(\nu^{\phi g}\nu^{\phi g *}\right)$, $\mathbf{P}_{\mathbf{N}} = E\left(\tilde{\mathbf{N}}\tilde{\mathbf{N}}^*\right)$.

3.2.3 Carrier Phase Riding (CPR)

Carrier phase measurement is cleaner than the code phase and has an unknown initial integer. If the initial position is known, the incremental differential carrier phase measurement can be used to calculate the incremental position of each epoch. Moreover, summing up the previous incremental position and the initial position allows us to obtain the current position. Except for the initial position, only carrier phase information is used to propagate the position estimate. Therefore, this is called CPR because it resembles the riding on the carrier. As a result, the position estimate is smooth. This smooth position estimate is similar to the one provided by an inertial system [Hwang]. Actually, the initial position is initialized by the code phase measurement.

The CPR has a very useful property which maintains the position accuracy when the aircraft is experiencing satellite geometry changes caused by the satellite setting or the aircraft maneuvering. The following gives the derivation of the CPR equations. First, the CPR positioning equation is derived. Next, the error equation of the CPR positioning is derived. Finally, the equation of the integration of the CPR and the differential observables is given, i.e., the state-space form equation of the integration filter, implying that the standard covariance analysis method can be applied to investigate the CPR performance.

Carrier Phase Riding Positioning

- Incremental differential carrier phase, i.e. the double-differenced (in time) carrier phase, measurement:

  Referring to Eqn. 3.8, the double-differenced carrier phase vector $\Delta\phi_k$ and its noise vector $\mathbf{w}_k^{\Delta\phi}$ can be defined as follows.

$$\Delta\phi_k \triangleq \phi_k - \phi_{k-1} = \mathbf{H}_k\mathbf{X}_k - \mathbf{H}_{k-1}\mathbf{X}_{k-1} + \mathbf{w}_k^{\Delta\phi} \tag{3.57}$$

  where

$$\mathbf{w}_k^{\phi} \triangleq \left(\nu_k^{\phi a} - \nu_k^{\phi g}\right) \tag{3.58}$$

$$\mathbf{w}_k^{\Delta\phi} \triangleq \mathbf{w}_k^{\phi} - \mathbf{w}_{k-1}^{\phi}. \tag{3.59}$$

- Position estimate using double-differenced carrier phase measurement:

  Let $\hat{\mathbf{X}}_k$ be the estimated position and substitute it into Eqn. 3.57. After rearrangement, the normal equation is obtained as

$$\hat{\mathbf{H}}_k\hat{\mathbf{X}}_k = \Delta\phi_k + \hat{\mathbf{H}}_{k-1}\hat{\mathbf{X}}_{k-1}. \tag{3.60}$$

Therefore, the WLS position of the CPR can be expressed as

$$\hat{\mathbf{X}}_k = \left(\hat{\mathbf{H}}_k^*\mathbf{W_k}\hat{\mathbf{H}}_k\right)^{-1}\hat{\mathbf{H}}_k^*\mathbf{W_k}\left(\Delta\phi_k + \hat{\mathbf{H}}_{k-1}\hat{\mathbf{X}}_{k-1}\right). \tag{3.61}$$

Or, to be explicit, as

$$\hat{\mathbf{X}}_k = \underbrace{\left(\hat{\mathbf{H}}_k^*\mathbf{W_k}\hat{\mathbf{H}}_k\right)^{-1}\hat{\mathbf{H}}_k^*\mathbf{W_k}\hat{\mathbf{H}}_{k-1}\hat{\mathbf{X}}_{k-1}}_{\text{Initial position}} + \underbrace{\left(\hat{\mathbf{H}}_k^*\mathbf{W_k}\hat{\mathbf{H}}_k\right)^{-1}\hat{\mathbf{H}}_k^*\mathbf{W_k}\left(\Delta\phi_k\right)}_{\text{Incremental position}}. \tag{3.62}$$

The first term in Eqn. 3.62 is the initial condition which is originally initialized by the differential code phase measurement. Meanwhile, the second term is the incremental position derived from the incremental differential carrier phase measurement. For ease of further derivation, $\mathbf{W_k}$ is set to equal $E\left(\mathbf{w}_k^{\Delta\phi}\mathbf{w}_k^{\Delta\phi *}\right)^{-1}$.

Error Equation of The Carrier Phase Riding

The error equation can be derived from Eqn. 3.60. In Eqn. 3.60, both $\hat{\mathbf{H}}_k$ and $\hat{\mathbf{X}}_k$ are position error dependent. The error in $\hat{\mathbf{H}}_k$ is the line-of-sight error caused by the imperfect estimate of the aircraft position. Theoretically, the line-of-sight error is small in the order of $O(-7)$ and can be ignored. However, due to the integration nature of the CPR, the integration time is in the order of $O(2)$, and when the line-of-sight error is coupled with the position of the aircraft, in the order of $O(4)$, the line-of-sight error is significant.

First, the following definitions are made:

$$\begin{aligned}\hat{\mathbf{H}}_k &= \mathbf{H}_k + \tilde{\mathbf{H}}_k \\ \widehat{\mathbf{X}}_k &= \mathbf{X}_k + \tilde{\mathbf{X}}_k\end{aligned} \tag{3.63}$$

where

$$\tilde{\mathbf{H}}_k = \delta \begin{bmatrix} -\mathbf{e}^*_{j,k} & 1 \\ \vdots & \end{bmatrix}_{j=1\cdots n} = \begin{bmatrix} \frac{\tilde{\mathbf{x}}^*_k}{S_{j,k}} & 0 \\ \vdots & \end{bmatrix}_{j=1\cdots n} \tag{3.64}$$

$$\tilde{\mathbf{X}}_k = \begin{bmatrix} \tilde{\mathbf{x}}_k \\ \tilde{b}_{uk} \end{bmatrix}. \tag{3.65}$$

Expanding the $\hat{\mathbf{H}}_k\hat{\mathbf{X}}_k$ term in Eqn. 3.60 produces

$$\hat{\mathbf{H}}_k\hat{\mathbf{X}}_k = \mathbf{H}_k\mathbf{X}_k + \tilde{\mathbf{H}}_k\mathbf{X}_k + \mathbf{H}_k\tilde{\mathbf{X}}_k + \tilde{\mathbf{H}}_k\tilde{\mathbf{X}}_k. \tag{3.66}$$

The $\tilde{\mathbf{H}}_k\mathbf{X}_k$ term is coupled with the aircraft's position and can be rewritten as

$$\tilde{\mathbf{H}}_k\mathbf{X}_k = \begin{bmatrix} \frac{\tilde{\mathbf{x}}^*_k}{S_{j,k}} & 0 \\ \vdots & \end{bmatrix} \begin{bmatrix} \mathbf{x}_k \\ b_{uk} \end{bmatrix} = \begin{bmatrix} \frac{\mathbf{x}^*_k}{S_{j,k}} & 0 \\ \vdots & \end{bmatrix} \begin{bmatrix} \tilde{\mathbf{x}}_k \\ \tilde{b}_{uk} \end{bmatrix} = \mathcal{H}_k\tilde{\mathbf{X}}_k \tag{3.67}$$

where

$$\mathcal{H}_k = \begin{bmatrix} \frac{\mathbf{x}^*_k}{S_{j,k}} & 0 \\ \vdots & \end{bmatrix}_{j=1\cdots n}. \tag{3.68}$$

Substituting Eqn. 3.67 into Eqn. 3.66 and neglecting the second order term produces

$$\hat{\mathbf{H}}_k\hat{\mathbf{X}}_k = \mathbf{H}_k\mathbf{X}_k + (\mathbf{H}_k + \mathcal{H}_k)\,\tilde{\mathbf{X}}_k. \tag{3.69}$$

Substituting Eqns. 3.69 and 3.57 into Eqn. 3.60, and after rearrangement, we have

$$(\mathbf{H}_k + \mathcal{H}_k)\,\tilde{\mathbf{X}}_k = \mathbf{w}_k^{\Delta\phi} + (\mathbf{H}_{k-1} + \mathcal{H}_{k-1})\,\tilde{\mathbf{X}}_{k-1}. \tag{3.70}$$

Define

$$\mathbb{H}_k = (\mathbf{H}_k + \mathcal{H}_k) \tag{3.71}$$

and substitute into Eqn. 3.70, the error equation of the CPR can be expressed as

$$\tilde{\mathbf{X}}_k = \left(\mathbb{H}_k^* \mathbf{W}_k \mathbb{H}_k\right)^{-1} \mathbb{H}_k^* \mathbf{W}_k \mathbb{H}_{k-1} \tilde{\mathbf{X}}_{k-1} + \left(\mathbb{H}_k^* \mathbf{W}_k \mathbb{H}_k\right)^{-1} \mathbb{H}_k^* \mathbf{W}_k \mathbf{w}_k^{\Delta\phi} \tag{3.72}$$

or

$$\tilde{\mathbf{X}}_k = \underbrace{\mathbf{F}_{cpr,k} \tilde{\mathbf{X}}_{k-1}}_{\text{Initial position error}} + \underbrace{\mathbf{G}_{cpr,k} \mathbf{w}_k^{\Delta\phi}}_{\text{Incremental position error}} \tag{3.73}$$

where

$$\begin{aligned}
\mathbf{W}_k &= E\left(\mathbf{w}_k^{\Delta\phi} \mathbf{w}_k^{\Delta\phi *}\right)^{-1}; \mathbf{G}_{cpr,k} = \left(\mathbb{H}_k^* \mathbf{W}_k \mathbb{H}_k\right)^{-1} \mathbb{H}_k^* \mathbf{W}_k; \\
\mathbf{F}_{cpr,k} &= \left(\mathbb{H}_k^* \mathbf{W}_k \mathbb{H}_k\right)^{-1} \mathbb{H}_k^* \mathbf{W}_k \mathbb{H}_{k-1} = \mathbf{G}_{cpr,k} \mathbb{H}_{k-1}; \\
\mathbf{W}_k &= E\left(\mathbf{w}_k^{\Delta\phi} \mathbf{w}_k^{\Delta\phi *}\right)^{-1}; \\
\mathbf{G}_{cpr,k} &= \left(\mathbb{H}_k^* \mathbf{W}_k \mathbb{H}_k\right)^{-1} \mathbb{H}_k^* \mathbf{W}_k; \\
\mathbf{F}_{cpr,k} &= \left(\mathbb{H}_k^* \mathbf{W}_k \mathbb{H}_k\right)^{-1} \mathbb{H}_k^* \mathbf{W}_k \mathbb{H}_{k-1} = \mathbf{G}_{cpr,k} \mathbb{H}_{k-1}.
\end{aligned}$$

Integration of the CPR and the Differential Observables

Following the idea of the LAAS/INS integration, the CPR can be treated as a navigation system and integrated with the differential code and the differential carrier phase observables as shown in Fig. 3.3 . Using estimation theory, the CPR position error can be estimated, thus improving the position accuracy. This section derives the required state-space form for the integration algorithm.

State Equation Eqn. 3.73 is not a standard state-space equation. Combining the above equation with Eqn. 3.59, Eqn. 3.73 can be organized as

$$\begin{bmatrix} \tilde{\mathbf{X}}_k \\ \mathbf{w}_k^{\phi} \end{bmatrix} = \begin{bmatrix} \mathbf{F}_{cpr,k} & -\mathbf{G}_{cpr,k} \\ 0 & 0 \end{bmatrix} \begin{bmatrix} \tilde{\mathbf{X}}_{k-1} \\ \mathbf{w}_{k-1}^{\phi} \end{bmatrix} + \begin{bmatrix} \mathbf{G}_{cpr,k} \\ \mathbf{I} \end{bmatrix} \mathbf{w}_k^{\phi} \tag{3.74}$$

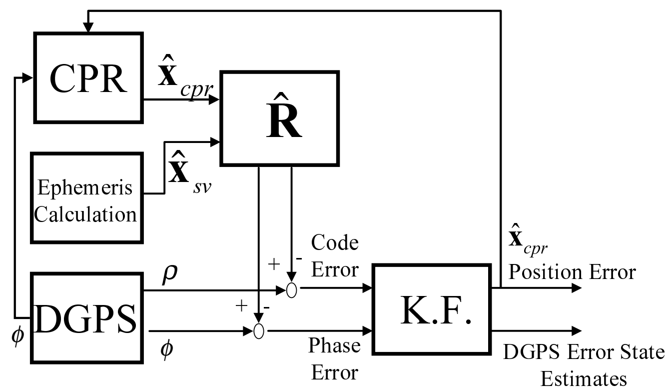

Figure 3.3: Block Diagram of the CPR Algorithm

or in the standard state-space form as

$$\mathcal{X}_{cpr,k+1} = \mathbf{F}_{cpr,k}\mathcal{X}_{cpr,k} + \mathbf{G}_{cpr,k}\mathbf{w}_k^{\phi} \tag{3.75}$$

where

$$\mathcal{X}_{cpr,k} = \begin{bmatrix} \tilde{\mathbf{X}}_{k-1} \\ w_{k-1}^{\phi} \end{bmatrix} \tag{3.76}$$

$$\mathbf{F}_{cpr,k} = \begin{bmatrix} \mathcal{F}_{cpr,k} & -\mathcal{G}_{cpr,k} \\ \mathbf{0} & \mathbf{0} \end{bmatrix} \tag{3.77}$$

$$\mathbf{G}_{cpr,k} = \begin{bmatrix} \mathcal{G}_{cpr,k} \\ \mathbf{I} \end{bmatrix}. \tag{3.78}$$

Measurement Update Equation To comply with the states as defined in Eqn. 3.76, the previous measurements can be used to update the dynamic equation. According to Eqn. 3.23, by shifting the epoch k to the epoch k-1 and following definition

$$\mathbf{H}_{ddi,k-1} = \begin{bmatrix} \Delta e_{1,k-1}^{*} & 0 \\ \vdots & \vdots \end{bmatrix},$$

the carrier phase update equation of the jth satellite can be expressed as:

$$\delta y^{\phi}_{j,k-1} = \left[\begin{array}{cc} \Delta \mathbf{e}^{*}_{j,k-1} & 0 \end{array} \right] \tilde{\mathbf{X}}_{k-1} + \Delta N_j + \left(m^{\phi a}_{j,k-1} - m^{\phi g}_{j,k-1} \right) + \left(\nu^{\phi a}_{j,k-1} - \nu^{\phi g}_{j,k-1} \right). \tag{3.79}$$

Therefore, the vector form of the double difference code and carrier phase measurement update equation is given as follows:

$$\mathbf{Y} = \left[\begin{array}{c} \delta y^{\rho}_{j,k-1} \\ \delta y^{\phi}_{j,k-1} \end{array} \right] \tag{3.80}$$

$$= \left[\begin{array}{cccc} \mathbf{H}_{ddi,k-1} & \mathbf{0} & \mathbf{H}^{\rho} & \mathbf{0} \\ \mathbf{H}_{ddi,k-1} & \mathbf{J}^{\Delta N} & \mathbf{0} & \mathbf{H}^{\Delta \mathbf{N}} \end{array} \right] \left[\begin{array}{c} \tilde{\mathbf{X}}_{k-1} \\ \mathbf{w}^{\phi}_{k-1} \\ \mathbf{X}^{\rho}_{k-1} \\ \Delta N_{k-1} \end{array} \right] + \left[\begin{array}{c} \mathbf{J}^{\rho} \\ \mathbf{0} \end{array} \right] \nu^{\phi \rho}_{j,k-1}$$

Eqns. 3.74 and 3.80 can be used to analyze the error covariance of the CPR algorithm using the standard Kalman filter [Brown].

3.3 The Multipath Model

The multipath model developed in this section provides a common base for comparing algorithms as described in the preceding sections where the multipath is assumed as a first order Gauss-Markov process. Therefore, the modeling process focuses on the code phase error versus the elevation angle and average time correlation, rather than on a detailed model.

The cause of the code multipath is briefly reviewed below. Ground multipath comes from the nearby reflection surfaces around the reference antenna. Previous research [Enge], [Braasch], [Dai] has demonstrated that the ground multipath is related to the elevation angle, the motion (Doppler) of the satellite and the height of the reference antenna [Enge]. Additionally, the ground multipath is not only satellite specific but also receiver and antenna technology dependent. For example, the narrow correlator receiver can reduce the multipath, and the choke ring antenna can cut off the low elevation reflections, also reducing the multipath. The airborne multipath originates from the local airplane reflection and the ground reflection. Since the reflection surface of the airplane is quite limited and the reflection from the ground changes rapidly, theoretically, the airborne multipath should be smaller and whiter. However, experimental data show a slow varying trend in the airborne multipath, as the following shows.

The experimental data were collected at 1 Hz at Moffett airport, Mountain View, California during the Queen Air flight test. The single frequency narrow correlator receiver, known as the Novatel GPS Card, was used in both the ground system and the airborne system. The ground system used the choke ring antenna to eliminate the low elevation angle reflections and the airborne system was equipped with two patch antennas, one installed at the top of the fuselage and the other installed at the top of the T-tail.

For a single frequency receiver, according to Eqns. 3.1 and 3.2, the measured multipath can be obtained by forming a code and carrier difference as listed below

$$\rho_k^i - \phi_k^i = 2I_k^i - N^i + m_k^i - m_k^{\phi i} + \nu_k^i - \nu_k^{\phi i} \tag{3.81}$$

where i denotes either the ground or the airborne user. Using the observations that the ionosphere delay I_k varies slowly, the integer cycle ambiguity N is a constant and the carrier phase multipath m_k^ϕ and noise ν_k^ϕ are negligible, the $2I_k - N$ can be accurately approximated by a polynomial fit in the postprocessing. Then, the measured multipath can be obtained by removing the polynomial fit from the code and carrier difference. Figure 3.4 shows the measured ground multipath and Fig. 3.5 shows the measured airborne multipath. There are data drop outs in Fig. 3.5 due to aircraft maneuvering. These drop outs are less than 5% of the total data set and, therefore, it is judged that this data set is still a reasonable representation of the pseudorange errors. By carefully inspecting the top and middle plots of Figs. 3.4 and 3.5, one can see that the ground multipath is larger than the airborne multipath. If one inspects

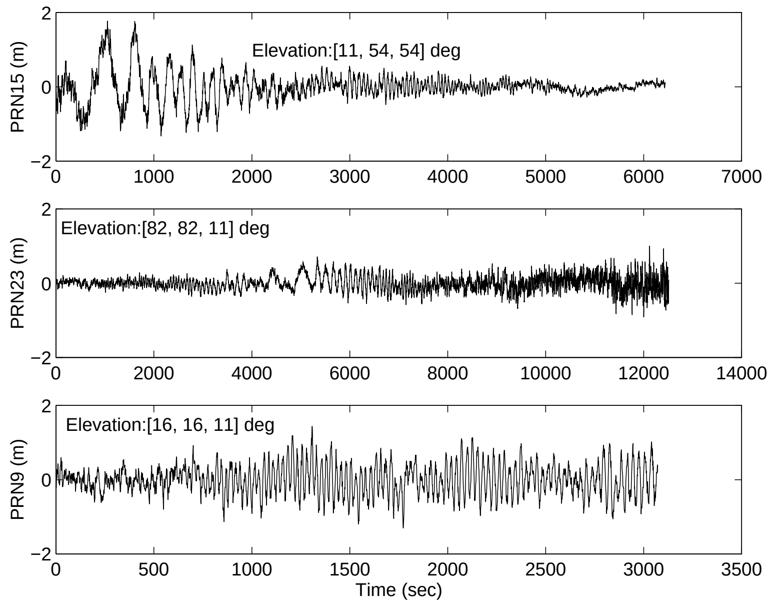

Figure 3.4: Measured Ground Code Phase Multipath. [a, b, c] means a=the initial elevation angle; b=the highest elevation angle; c=the final elevation angle

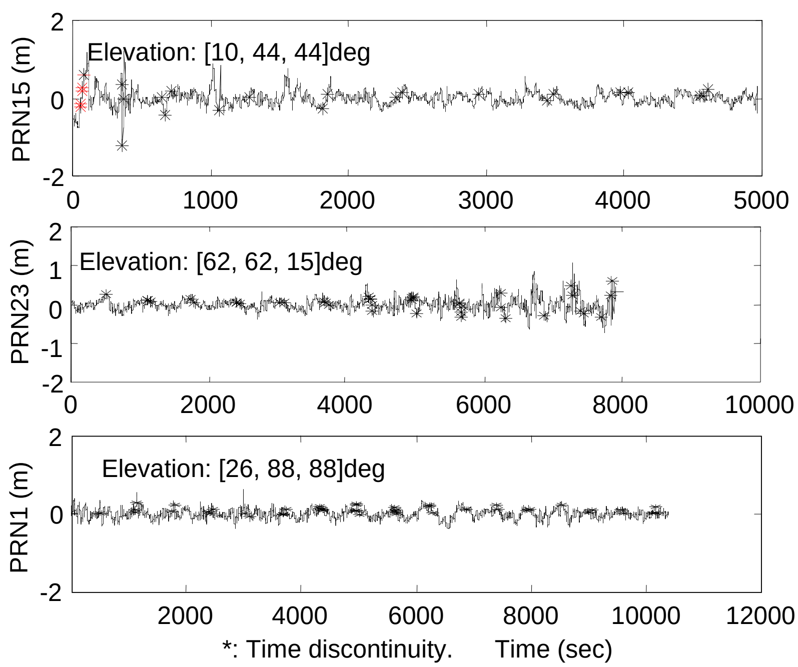

Figure 3.5: Measured Airborne Code Phase Multipath

the multipath as a function of elevation angle for both the ground and airborne multipaths, the magnitude of the multipath is larger at low elevation angles and smaller at high elevations.

To establish a relationship between the multipath and the elevation angle, the mean bias and standard deviation of each 500 points segment and the corresponding mean elevation angle are computed for the whole set of data. Then linear regression is applied to obtain the relationship between the standard deviation of the mean bias (σ_{bias}) and the mean elevation, as well as the relationship between the standard deviation (σ_v) and the mean elevation. In order to simplify the following performance comparison, the overall multipath model is set to be the root-sum-square of σ_{bias} and σ_v. The obtained ground (σ_{ground}) and airborne (σ_{air}) multipath models are listed below.

- The ground multipath:

$$\begin{aligned} \sigma_v &= e^{-0.0303*el-0.1734} \quad m \\ \sigma_{bias} &= -0.0004el + 0.0659 \quad m \\ \sigma_{ground} &= \sqrt{\sigma_v^2 + \sigma_{bias}^2} \quad m \end{aligned}$$

- The airborne multipath:

$$\begin{aligned} \sigma_v &= e^{-0.0135*el-1.5296} \quad m \\ \sigma_{bias} &= 0.03 \quad m \\ \sigma_{air} &= \sqrt{\sigma_v^2 + \sigma_{bias}^2} \quad m \end{aligned}$$

  where σ_v is the standard deviation of the time-variant multipath in meters, σ_{bias} is the standard deviation of the mean bias of the multipath in meters, and el is the elevation angle of the satellite in degrees.

Figures 3.6 and 3.7 display the standard deviation (σ_v) of the code phase multipath versus the elevation angle of the measured ground and the airborne multipath. Each

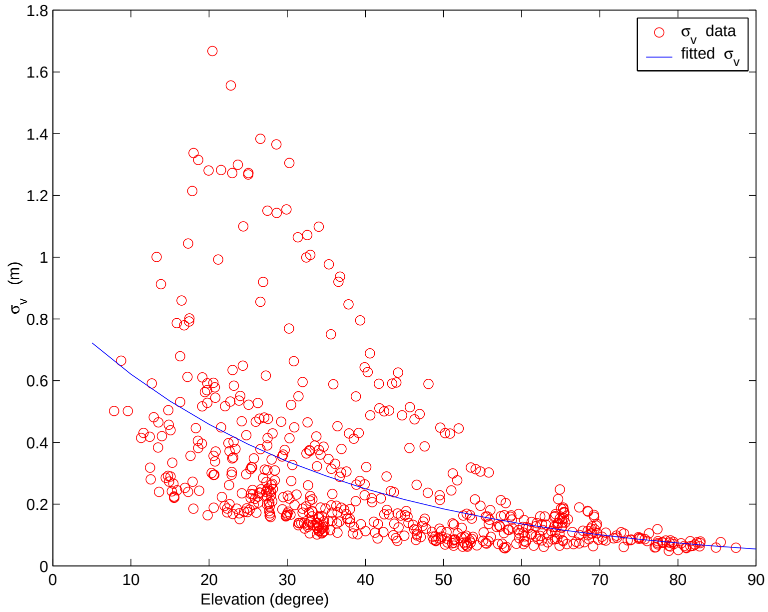

Figure 3.6: Statistics of the Ground Multipath: The standard deviation of the code phase multipath versus the elevation angle of the measured ground multipath.

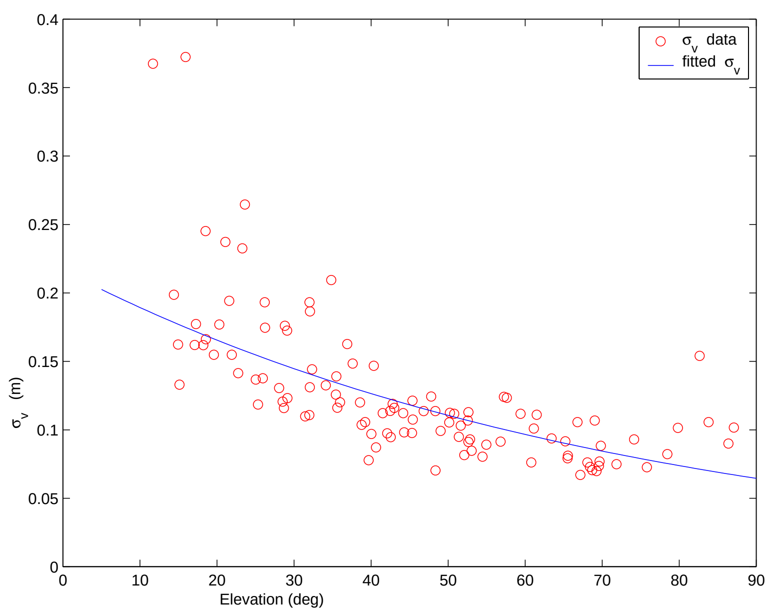

Figure 3.7: Statistics of the Airborne Multipath: The standard deviation of the code phase multipath versus the elevation angle of the measured airborne multipath

circle (o) denotes a σ_v of 500 data points as mentioned previously. The solid lines present the fitted models are appropriate.

Regarding the time relation, the whole set of data was roughly estimated for both the ground and the airborne multipaths, giving a time constant of two minutes for the ground multipath and 1.4 minutes for the airborne multipath. In the following simulation, the above parameters are used.

3.4 Simulation Setup

3.4.1 The Environment

The environment of this simulation is designed to include a live satellite constellation, which is calculated using a real almanac, to include the satellite motion for algorithm comparisons. The airport location is set at Moffett Airport. The in-view satellites of both the airborne user and ground station are calculated separately with a masking angle of 7.5 degrees. The common viewed satellites are then selected for the differential corrections. The trajectory of the aircraft in this simulation is taken from the Queen Air flight test and lasts for 450 seconds. The final approach followed the 3-degree glide slope as specified by the FAA. For the DGPS/INS integration, the INS considered in this simulation is the navigation grade Litton LN-100 as mentioned in Chapter 2.

3.4.2 The Cases Considered

The starting time of the approach was randomly selected as 36000 seconds of the GPS time and Fig. 3.8presents the sky plot of the common view satellites between the airborne user and the reference station during the approach. The numbers in Fig. 3.8 are the unique pseudorandom number (PRN) of the viewed satellites. To illustrate the effect of satellite drop out, two satellite drop outs that cause the worst geometry degradations were introduced at 2 minutes before touch down (T=330”) and 1 minute before touch down (T=390”), respectively. At T=330”, PRN 26 was

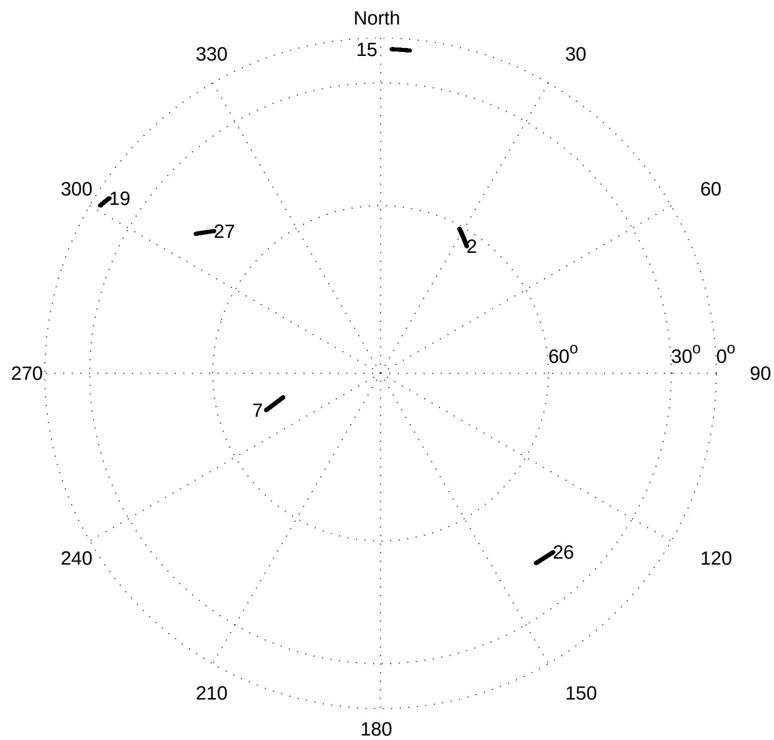

Figure 3.8: Sky Plot of the Common View Satellites Between the Airborne User and the Reference Station

dropped and the VDOP increased from 1.7 to 3.8. At T=390", PRN 15 was also dropped and the VDOP increased from 3.8 to 4.3.

3.5 Performance Comparison

Algorithms for comparison include CSC, CCU, CPR and the DGPS/INS integration. First, the DGPS only algorithms are compared.

The top plot of Fig. 3.9 presents the simulation results of CSC (the dash-dot line), CPR (the dash line) and CCU (the solid line). The horizontal axis is the approach time, and 0 represents the start of the approach. The vertical axis represents the 2-sigma value of the vertical error covariance. Three significant results can be obtained from Fig. 3.9 when satellite outages occurs:

- For the CSC user, the vertical error covariance is very sensitive to the satellite

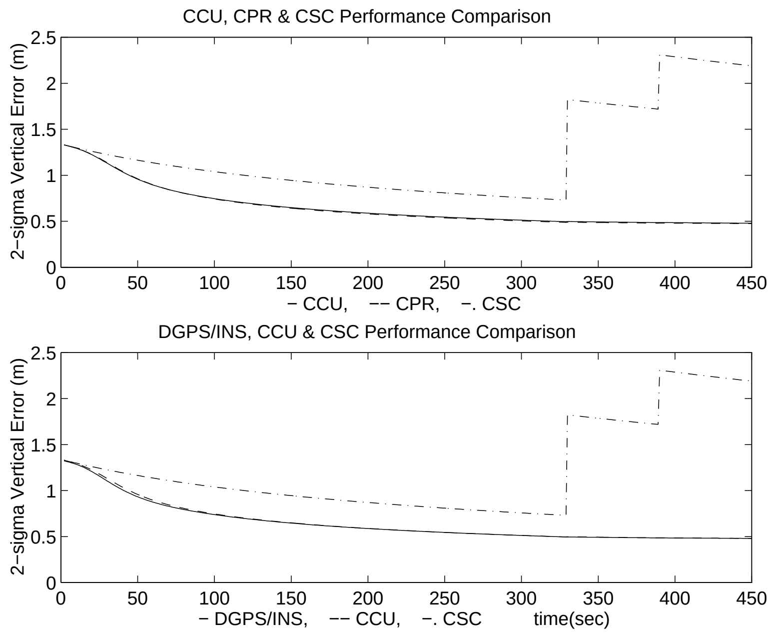

Figure 3.9: Performance Comparison of DGPS Algorithms and DGPS/INS. Top: Performance comparison of the GPS algorithms – CSC, CPR and CCU. Bottom: Performance comparison of the DGPS/INS and CCU.

geometry variation.

- For the carrier phase algorithm (CCU or CPR) user, only a slight effect can be observed compared to the CSC user.

- For the carrier phase algorithms, both CCU and CPR provide identical accuracy but different implementations.

Second, the DGPS/INS can be compared to the carrier phase algorithm CCU. The bottom plot of Fig. 3.9 displays the vertical error covariance of the DGPS/INS, CCU and CSC. The DGPS/INS is obviously as accurate as the DGPS carrier phase algorithm when more than four satellites are in view.

The above results can be explained as follows.

- Two mechanisms are behind the DGPS algorithms: (1) the carrier smoothing effect, (2) the satellite motion effect. The carrier smoothing effect uses the less noisy carrier phase to smooth out the noise in the code phase signal. Meanwhile, the satellite motion effect is unique to those carrier phase algorithms with an unknown integer cycle ambiguity. The satellite motion effect provides the observability of the integer cycle ambiguity. Therefore, the longer the satellite motion is observed the more accurate the integers are resolved.

The CSC only uses the carrier smoothing effect and its performance is based only on the code phase error and satellite geometry. Therefore, the variation of the satellite geometry directly influences the accuracy of the CSC as shown in Fig. 3.9.

The carrier phase algorithms are initialized by the code phase position. Specifically, the initial integer cycle ambiguity is obtained by setting the carrier phase solution equal to the code phase. Then, the positions can be propagated by transforming the measured incremental carrier phase into the incremental position. Meanwhile, a better position can be obtained using the satellite motion effect to improve the accuracy of the integer cycle ambiguity, as shown in Fig. 3.9. For example, Eqn. 3.73 presents CPR's error equation which includes two parts: the initial position error and the incremental position error. The initial position error, $\mathbf{F}_{cpr,k}\tilde{\mathbf{X}}_{k-1}$, is actually the position error at epoch k-1, since $\mathbf{F}_{cpr,k}$ is an unity matrix examined by numerical computation. It depends on the estimate of the integer cycle ambiguity, therefore, a better estimate of the integer cycle ambiguity implies a more accurate initial position. The incremental position error depends on the satellite geometry and carrier phase error at epoch k, because the carrier phase algorithms propagate on the carrier phase-based incremental position.

When a satellite sets (or drops out for any reason) at epoch k, it does not affect the position error at epoch k-1 which is the initial position error for the CPR positioning at epoch k. However, it does affect the satellite geometry for the incremental position at epoch k and also the estimation efficiency of the integer cycle ambiguity. Since the carrier phase error is significantly smaller than the code phase error, the effect of satellite geometry changes on the incremental

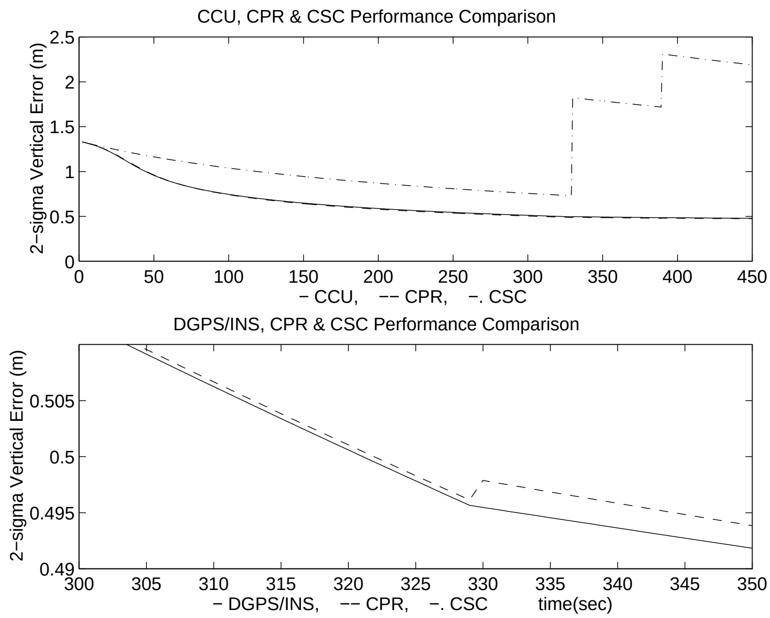

Figure 3.10: Magnified View of the Effect of the DGPS/INS and the CPR

position error at epoch k is also small. The total error is the root-sum-square of both errors mentioned above. Since the incremental position error at epoch k due to a satellite setting is small, the total error at epoch k is dominated by the initial position error, which is not affected by the satellite setting, therefore, slight position error change will be seen. This answers the question of why the position error covariance of the carrier phase algorithms is almost negligible when satellite geometry changes. The bottom plot of Fig. 3.10 displays the magnified vertical error covariance of the carrier phase algorithm around the first satellite drop (T=330 sec.) As one can observe, there is a slight increase of the covariance, which is much smaller than that of the CSC as shown in the top plot of Fig. 3.10. The bottom plot of Fig. 3.10 also displays the decrease of the position error converging rate caused by a satellite drop, because less satellite motion effect can be used to estimate the integer cycle ambiguity.

- For the DGPS/INS integration: According to the complementary filtering [Brown], the integration can be characterized as follows,

- The INS smoothes the data and provides excellent short-term stability. Meanwhile, due to the drift, the integration has an inaccurate initial position.
- The differential code phase measurements provide range information which includes multipath errors. For the integration, this range information can be used to obtain the initial position.
- The differential carrier phase measurements provide range information with an unknown integer cycle ambiguity. However, the incremental differential carrier phase is very precise. For the integration, this information can be used to provide precise incremental positions.

The above characterization implies that the integration filter will use the differential code phase measurements to initialize the filter, then follow the precise differential carrier phase measurements to update the integrated position. Simultaneously, the integration filter will use the short-term stability of the INS to smooth the differential carrier phase measurement and use the satellite motion effect to improve the estimate of the integer cycle ambiguity. Therefore, the covariance of the DGPS/INS behaves similar to that of the carrier phase algorithms and is marginally better than the carrier phase algorithms as shown in Fig. 3.10. However, the accuracy remains the same. The bottom plot of Fig. 3.10 displays the difference between the DGPS/INS and the carrier phase algorithms. When satellite geometry changes, the DGPS/INS can resist the change rather than changing with the satellite geometry like the carrier phase algorithms. This characteristic is the benefit of the DGPS/INS. Moreover, this benefit also implies that when less than four satellites are in view, none of the DGPS algorithms will work, but the DGPS/INS will keep working, improving continuity.

3.6 Summary

The key points of the comparison of the DGPS/INS and DGPS algorithms can be summarized as follows.

1. In terms of accuracy, the carrier phase algorithms are superior to the CSC. The cost is the extra data link bandwidth for the differential phase corrections.

2. CCU and CPR are essentially the same. They are equally accurate, but are different implementations. Although CCU is simpler, CPR provides further insight into the integration.

3. The main contribution of the INS is that it improves continuity. Notably, it does not provide significantly better accuracy than the DGPS carrier phase algorithms with the error models used in this analysis.

Chapter 4

PseudoLite-Based Precision Landing Backup System

The PL aided GPS-based precision approach and landing systems, such as the IBLS [Cohen, a], need to deal with the integer cycle ambiguity (ICA) when using the carrier phase measurements for high precision. Additionally, all the DGPS systems require a valid data link system to provide reference corrections and PL synchronization. The goal of this chapter is to explore a backup system that could survive GPS and/or data link failures.

This chapter introduces a system comprised of three PLs under the approach path and an onboard INS. The system can operate with no data link, no ICA problems and no PL synchronizations. It is called the 3-PLs/INS system. The core technique of the 3-PLs/INS system is the 3-PL's range rate-aiding method, which uses the Doppler information provided by 3 appropriately placed PLs to calibrate the onboard navigation grade INS to provide a RNP that allows the most stringent landing minimums (Category III). Since the 3-PLs/INS system is a backup for the local area system during the final phase of an approach, GPS still needs to be available long enough to guide the airplane into the service area of the backup system. If GPS services are lost prior to entering to the service area of the 3-PLs/INS system, the INS alone can be used to coast into the service area. The amount of time that the user can coast on the INS alone is analyzed in detail in this chapter. Another means for coasting into

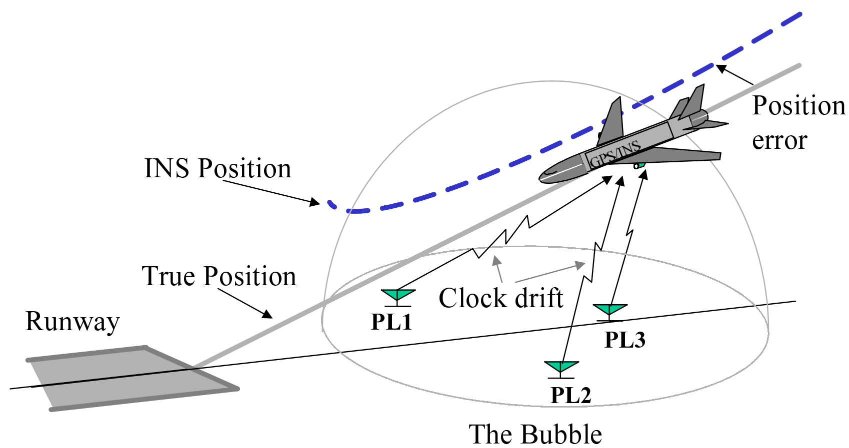

Figure 4.1: Operational Concept of the 3-PLs/INS System

the service area of the 3-PLs/INS system is a DME-aided INS [Boeing] or DME-aided dead reckoning system which are currently under study [Gebre-Egziabher].

The following describes the system structure, gives the theory of this method and its error equations, discusses the operating range and accuracy via Monte Carlo simulation. The performance of this PLs/INS system is evaluated with various RNP following the tunnel concept RNP [Kelly]. The performance is evaluated according to a 95% Total System Error (TSE) at the runway threshold. Herein, TSE is defined as the root-sum-square of the Flight Technical Error (FTE) and the Navigation Sensor Error (NSE). FTE is caused by autopilot control imperfection and NSE is caused by the position determination error.

4.1 The System Structure

Figure 4.1 illustrates the operational concept of the 3-PLs/INS system. A common question about this system is why it requires three PLs. However, with two PLs (located on either side of the approach), only the position of the aircraft's flight path at its closest approach to the PLs can be determined, and the descent angle of the flight path is unobservable. Thus, any descent angle of the approach line would yield the same range rate time history. Because of the above facts, the method requires three PLs arranged in a triangle.

When an airplane flies over the 3-PL bubble, the airplane's receiver uses the preselected PRN codes to receive three aiding phase rates from the PL-triad. This enables the INS to be updated at the exit of the bubble and the airplane to navigate on the updated INS to the approach and landing.

The total system includes both the airborne segment and ground segment.

- The airborne segment:

  The airborne segment considered herein is a CAT III Boeing 737 equipped with an INS and a DGPS system which has a ventral antenna for receiving PL signals. To evaluate the concept, the analysis utilizes related flight test data to represent the dynamics of the airplane. Therefore, the performance evaluation excludes the dynamic model of the 737, which contributes to the FTE, but includes the FTE effect acquired from related flight tests [Cohen, a].

  This analysis considers an open loop and loosely coupled PLs and INS integration structure for ease of integrating two existing systems. Figure 4.2 illustrates the integration block diagram of the DGPS/3PLs/INS system for reference.

- The ground segment:

  The ground segment includes three PLs placed equilaterally ahead of the runway at a distance that allows the airplane to fly for 60 seconds before touchdown (TD). The effective PL bubble considered herein is the space where the airplane can receive all three PL signals. The size of the PL bubble allows the approaching airplane to receive the PL signals for at least 20 seconds. Thus the bubble is a semi-sphere with a radius of approximately 650 meters.

Note, the requirement for the system is that prior navigation accuracy must be sufficiently accurate so the aircraft can find the bubble.

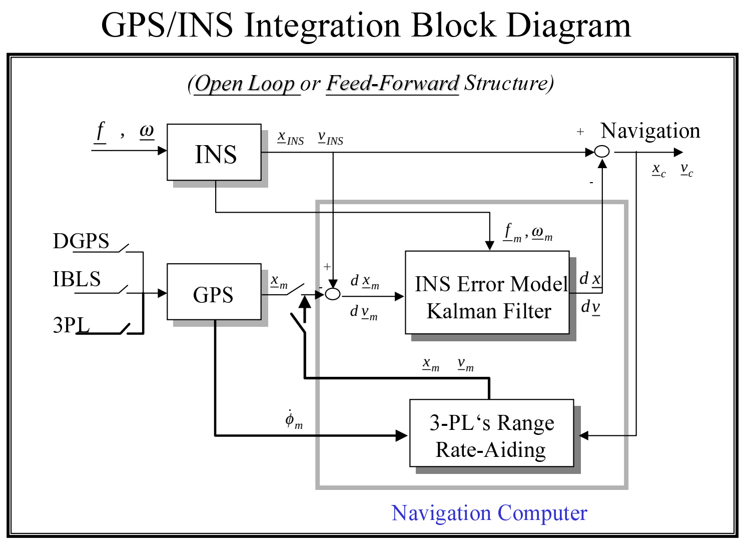

Figure 4.2: Block Diagram of the DGPS/3PLs/INS Integration

4.2 The 3-PL's Range Rate-Aiding Method

The 3-PL's range rate-aiding method, an application of the GPS ranging technology, is the core technique of the 3-PLs/INS system. The method provides position fixes at the bubble exit without satellite signals, a data link or PL synchronization. By properly placing 3 PLs before the runway and together with the onboard INS, the phase rate measurements (from a GPS receiver tracking PL signals) and the INS position and velocity can be used to compute the position and velocity errors of the aircraft at the bubble exit. This information can be used to update the INS for the ensuing flight to the runway. Below, the theory (including the important clock drifting effect), the error analysis equations, and the accuracy and operating range of this method are described.

4.2.1 The Theory

Herein, an aircraft's approach is considered to be at a constant velocity along a straight line. An aircraft that has reverted to using INS for navigation will have an error in its calculated position and velocity due to INS drift. Assume that the

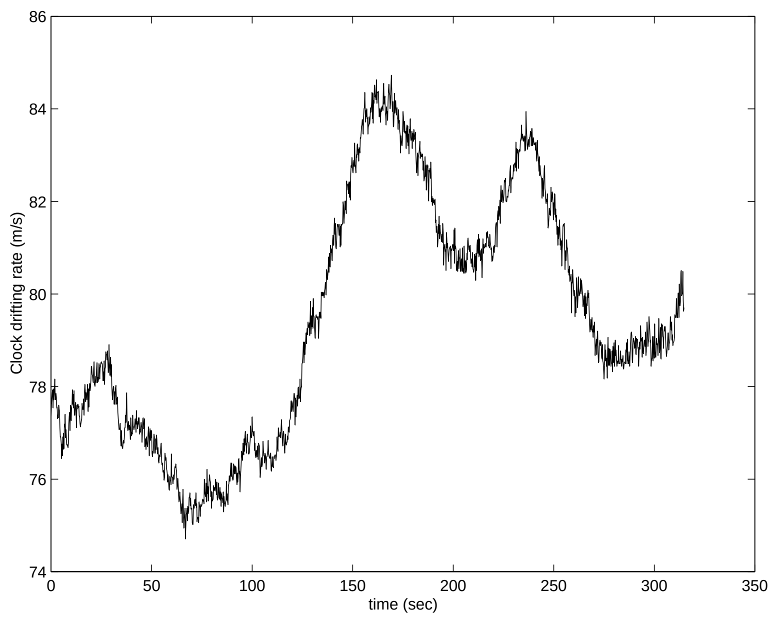

Figure 4.3: Example of the Measured Differential Clock Drift Rate Between Each PL and the Receiver.

drifted trajectory of the airplane is a straight line with an unknown initial position and an unknown initial velocity while the airplane flies through the bubble. The role of the PLs is to locate that drifted line, i.e., to reduce the drift error to a level that is acceptable for landing. When the aircraft is inside the bubble, the range rate, i.e. the Doppler, is available from the onboard GPS receiver via the PL signals. The variation of the Doppler shift contains position and velocity information about the aircraft with respect to the PL coordinate system. Thus, these measurements can be used to estimate the orientation and position of the line and the velocity of the aircraft.

An important issue of this method is the clock drifting effect inherent in the phase rate measurement because both the user clock and each PL clock drift. A proper model for the clock rate drift is necessary. A lesser clock drift rate implies a higher position accuracy. Thus, the following analysis considers and compares two grades of clock: a Quartz Oscillator (XO) and a Rubidium (Rb). XO data were measured from a PL using a Trimble nine-channel receiver through a fixed length cable. Figure 4.3 presents an example of the measured data. Rb data are simulated using van Dierendonck's 2-state clock model [van Dierendonck] with Rubidium clock parameters [Kee].

4.2.2 PL Range Rate Error Equation

The phase rate measurement equation is

$$\dot{\phi}_{jk} = \dot{R}_{jk} + c\left(\dot{t}_{uk} - \dot{t}_{jk}\right) + \upsilon_k^{\phi} \tag{4.1}$$

where $\dot{\phi}$ represents the received phase rate measurement of the aircraft with respect to the jth PL; $\dot{R}$ denotes the range rate between the aircraft and the PL; c is the speed of light; $\dot{t}$ represents the clock drifting rate. υ represents the phase rate measurement noise. Subscript j means that the measurement is with respect to the jth PL, in this case, j =1, 2, 3. Subscript k stands for the kth epoch and subscript u stands for the user.

Linearizing $\dot{R}_{jk}$ in Eqn. 4.1 with respect to the nominal trajectory $\mathbf{x}_c$ and the nominal velocity $\dot{\mathbf{x}}_c$, produces

$$\dot{R}_{jk} = \dot{R}_{jk,c} + A_{jk}\delta\mathbf{x}_k + B_{jk}\delta\dot{\mathbf{x}}_k \tag{4.2}$$

where $\dot{R}_{jk,c}$ represents the nominal range rate with respect to the nominal trajectory; $A_{jk} = \left[\mathbf{e}_{jk} + \mathbf{e}_{jk}\mathbf{e}_{jk}^{*}\frac{\dot{\mathbf{x}}_k}{R_{jk}}\right]^*$; $B_{jk} = \mathbf{e}_{jk}^*$, $\mathbf{e}_{jk}$ represents the unit vector with respect to the jth PL at epoch k. $\delta\mathbf{x}_k$ is the airplane's position variation vector at epoch k and $\delta\dot{\mathbf{x}}_k$ denotes the variation vector of the airplane velocity at epoch k. Meanwhile, subscript c represents the nominal value.

In a short period, e.g. 20 seconds while the airplane is inside the bubble, according to D. Wells [Wells] and observation of Fig. 4.3, the clock rate difference can be modeled as a first order polynomial to include effects of the differential frequency offset (α_{j0}) and frequency drift (α_{j1}). Therefore,

$$\begin{aligned} c\left(\dot{t}_{uk} - \dot{t}_{jk}\right) &= \left(\alpha_{j0} + \delta\alpha_{j0}\right) + \left(\alpha_{j1} + \delta\alpha_{j1}\right)\left(t_k - t_0\right) + v_k^t \\ &= D_{jk} + \delta\alpha_{j0} + \delta\alpha_{j1}\left(t_k - t_0\right) + v_k^t \end{aligned} \tag{4.3}$$

where D_{jk} is the a priori value of the clock drift rate, $\delta\alpha_{j0}$ and $\delta\alpha_{j1}$ are correction parameters, t_k represents the time epoch inside the bubble, t_0 is the time at the entrance of the bubble, and v_k^t denotes the higher order clock noise in meters.

For the airplane's position error, e.g. 20 seconds while it is inside the bubble, referring to the previously drifted straight line assumption, we assume the position and velocity errors have the following dynamics (to the first order approximation),

$$\begin{aligned} \delta\dot{\mathbf{x}}_k &= \delta\mathbf{v}_0 \\ \delta\mathbf{x}_k &= \delta\mathbf{x}_0 + \delta\mathbf{v}_0\left(t_k - t_0\right) \end{aligned} \tag{4.4}$$

where $\delta\mathbf{v}_0$ denotes the initial velocity error and $\delta\mathbf{x}_0$ represents the initial position error.

Let $t_k - t_0$ equal $k\Delta t$ where Δt represents the sampling time and k represents the number of epochs. Then substitute Eqns. 4.2, 4.3 and 4.4 into 4.1. After reorganizing the terms, the phase rate error equation can be obtained in terms of the initial position and velocity error, and clock drift rate parameters as

$$\begin{aligned} Z_{jk} &= \dot{\phi}_{jk} - \dot{R}_{jk,c} - D_{jk} \\ &= H_{jk}\delta\mathbf{X}_0 + v_k^t \end{aligned}$$

where

$$\begin{aligned} H_{jk} &= \left[\begin{array}{cccc} A_{jk} & A_{jk}\cdot k\Delta t + B_{jk} & 1 & k\Delta t \end{array}\right] \\ \delta\mathbf{X}_0 &= \left[\begin{array}{cccc} \delta\mathbf{x}_0^* & \delta\mathbf{v}_0^* & \delta\alpha_{j0} & \delta\alpha_{j1} \end{array}\right]. \end{aligned}$$

As the airplane flies through the bubble, measurements are obtained from the

GPS receiver and the INS, the error equation can then be stacked up and a Least Squares method can be used to solve the initial position error ($\delta\mathbf{x}_0^*$), the initial velocity error ($\delta\mathbf{v}_0^*$) , the differential frequency offset ($\delta\alpha_{j0}$) and the differential frequency drift ($\delta\alpha_{j1}$). In total, 12 states are estimated.

4.2.3 INS Error Model

To simplify the analysis, several assumptions are made to produce the INS error model. Concerning the final approach, the earth curvature and rotation rate are assumed to be negligible. Thus, the nominal flight path can be approximated by a straight line without rotation. However, this straight line assumption, made in subsection 4.2.1, is not required for the method to work but to simplify analysis. Error models of the gyro and the accelerometer include scale-factor, bias drift, and noise terms. Based on the flight path assumption made above, the scale-factor term is present in the accelerometer's vertical direction. A first order Gauss-Markov process is assumed for the accelerometer bias and gyro drift. The following sixteen-state INS error model can be derived.

$$
\begin{aligned}
\dot{\mathbf{x}} &= \mathbf{F}\mathbf{x} + \mathbf{G}\mathbf{w} \\
\mathbf{y} &= \mathbf{x}_{INS} - \mathbf{x}_m = \mathbf{H}\mathbf{x} + \mathbf{v}
\end{aligned}
$$

where

$$
\begin{aligned}
\mathbf{x} &= \begin{bmatrix} \varepsilon^* & d\mathbf{x}^* & d\mathbf{v}^* & \mathbf{b}^* & \mathbf{d}^* & K_z \end{bmatrix}^* \\
\mathbf{w} &= \begin{bmatrix} \omega^{a*} & \omega^{g*} & \upsilon^{b*} & \upsilon^{d*} \end{bmatrix}^* \\
\mathbf{F} &= \begin{bmatrix} \mathbf{0} & \mathbf{0} & \mathbf{0} & \mathbf{0} & \mathbf{C}_b^n & \mathbf{0}_1^* \\ \mathbf{0} & \mathbf{0} & \mathbf{I} & \mathbf{0} & \mathbf{0} & \mathbf{0}_1^* \\ \mathbf{F}_n & \mathbf{N} & \mathbf{0} & \mathbf{C}_b^n & \mathbf{0} & \mathbf{C}_k \\ \mathbf{0} & \mathbf{0} & \mathbf{0} & \frac{-\mathbf{I}}{\tau_b} & \mathbf{0} & \mathbf{0}_1^* \\ \mathbf{0} & \mathbf{0} & \mathbf{0} & \mathbf{0} & \frac{-\mathbf{I}}{\tau_d} & \mathbf{0}_1^* \\ \mathbf{0}_1 & \mathbf{0}_1 & \mathbf{0}_1 & \mathbf{0}_1 & \mathbf{0}_1 & 0 \end{bmatrix} \\
\mathbf{G} &= \begin{bmatrix} \mathbf{I} & \mathbf{0} & \mathbf{0} & \mathbf{0} \\ \mathbf{0} & \mathbf{0} & \mathbf{0} & \mathbf{0} \\ \mathbf{0} & \mathbf{I} & \mathbf{0} & \mathbf{0} \\ \mathbf{0} & \mathbf{0} & \frac{\mathbf{I}}{\tau_b} & \mathbf{0} \\ \mathbf{0} & \mathbf{0} & \mathbf{0} & \frac{\mathbf{I}}{\tau_d} \\ \mathbf{0}_1 & \mathbf{0}_1 & \mathbf{0}_1 & \mathbf{0}_1 \end{bmatrix} \\
\mathbf{H} &= \begin{bmatrix} \mathbf{0} & \mathbf{I} & \mathbf{0} & \mathbf{0} & \mathbf{0} & 0 \end{bmatrix}.
\end{aligned}
$$

The state $\mathbf{x}$ includes ε, the misalignment error; $d\mathbf{x}$, the position error; $d\mathbf{v}$, the velocity error; $\mathbf{b}$, the accelerometer bias; $\mathbf{d}$, the gyro drift; and K_z, the z direction accelerometer scale-factor error. In the system matrix $\mathbf{F}$, $\mathbf{F}_n$ denotes the skew symmetric matrix of the specific force in navigation frame; $\mathbf{N}$ represents the linearized gravity matrix; $\mathbf{C}_b^n$ is the transformation matrix from body frame to navigation frame, in this simplified straight line case, $\mathbf{C}_b^n$ is equal to $\mathbf{I}$ the unity matrix; τ_b represents the correlation time of the accelerometer bias; τ_d represents the correlation time of the gyro drift; $\mathbf{0}$ is a 3 by 3 zero matrix; $\mathbf{0}_1$ is a 1 by 3 zero vector; and $\mathbf{C}_k$ is a 3 by 1 vector, its third element is equal to $a_z - g$; a_z represents the z-direction acceleration and g represents the gravity. The process noise $\mathbf{w}$ includes ω^a and ω^g which are the measurement noise of the accelerometers and the gyros, respectively. Meanwhile, υ^b and υ^d are the driving noises of the accelerometer biases and the gyro drifts, respectively. Furthermore,

Table 4.1: Parameters of the Tactical Missile Grade IMU, LN-200

Parameter	**Accelerometer**	**Gyro**
Bias	50 μg	0.35 $°/hr$
Time Constant	60 sec	100 sec
Scale Factor	300 ppm	100 ppm
Noise	50 $\mu g/\sqrt{Hz}$	0.1 $°/\sqrt{Hz}$

$\mathbf{v}$ is the measurement noise of the aiding system. Additionally, $\mathbf{y}$ is the differential observation. Finally, $\mathbf{H}$ is the measurement matrix.

The following analysis considers two grades of the inertial system for comparison, namely the navigation grade and the tactical missile grade. Recall Table 2.3 for the parameters of the LN-100. Table 4.1 lists parameters of the tactical missile grade Inertial Measurement Unit (IMU), LN-200. Later, the INS position error will be generated using the above error equations with these parameters.

4.2.4 Accuracy and Operating Range

Theoretically, if the error equation has independent residuals then the Least Squares estimation uncertainty is the combined effect of the geometry of the PLs and the phase rate measurement error. This relationship increases the importance of the PLs geometric pattern. For three PLs, an equilateral triangle pattern provides the best geometry and is used herein. However, the non-white residual of the clock rate drift corrupts the Least Squares uncertainty estimation. Therefore, a Monte Carlo simulation is used to determine the accuracy and operating range of this method. Parameters of the simulation include the grades of INS, DGPS outage time (minutes before bubble entrance) and grades of clock.

Figure 4.4 illustrates the simulation scenario setup. Assuming that the INS was calibrated by the DGPS during the flight, then the DGPS is briefly lost before the aircraft enters the bubble. Meanwhile, the INS starts to drift. When the aircraft flies through the bubble, phase rate measurements are obtained from the GPS receiver. At the bubble exit, a batch process (as described in subsection 4.2.2) is run to solve the initial position and velocity errors, correct the drifted position, and calculate the

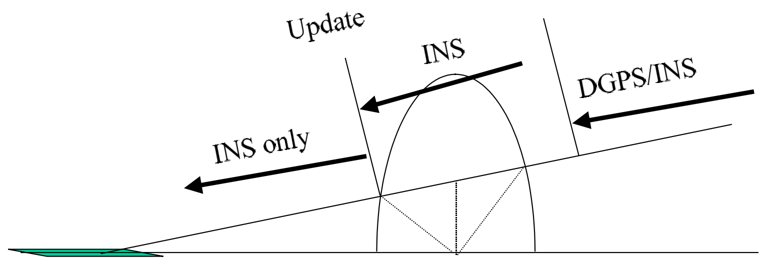

Figure 4.4: Simulation Scenario Setup.

corrected position error at the bubble exit point. In this scenario, the knowns are the inaccurate aircraft position and velocity, phase rate measurements from all 3 PLs, and the accurate position of all 3 PLs. The unknowns are the aircraft's position at the bubble exit and the differential clock drift of all 3 PLs.

The aircraft's position obtained from the INS includes two parts: the nominal trajectory and the INS drift. The nominal trajectory considered herein is the 3° glide slope. The INS drift is calculated using the INS error model described in subsection 4.2.3. Figure 4.5 shows the covariance computed via the standard Kalman filter of the pure inertial systems of the integrated DGPS/INS currently considered when GPS outage occurs. The DGPS system considered is the WAAS system which has an accuracy of [1.5m, 1.5m, 2.0m] [Walter] in the x, y and z directions, respectively. Herein, the WAAS error is considered as a random noise. For each run of the simulation, the INS drift is computed using randomly generated noises for the INS error model.

According to Eqn. 4.1, the phase rate measurement error and the clock drift rate (the quality of the clock) of both the GPS receiver and the PL are error sources that relate to the 3-PL's range rate-aiding method. The phase rate measurement error considered herein is 0.05 m/s, which is derived from the phase measurement error

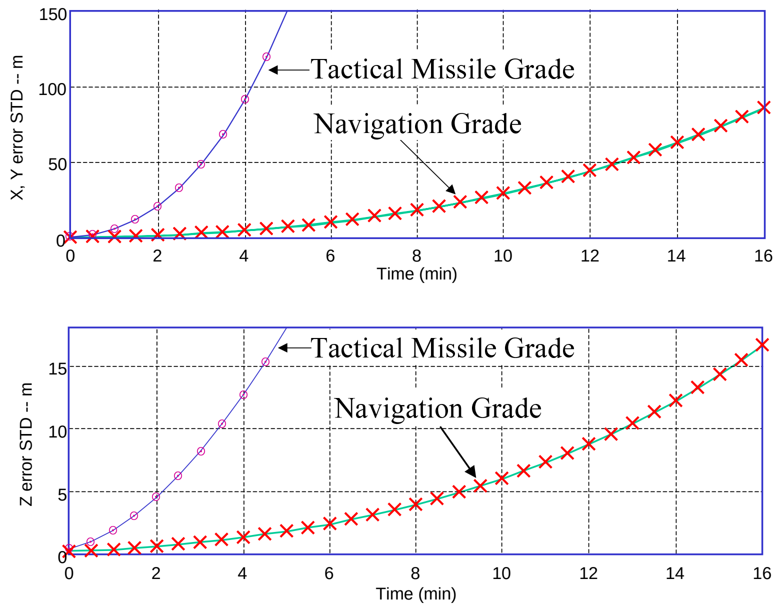

Figure 4.5: Covariance of the DGPS Corrected Inertial Systems. x represents the navigation grade INS and o represents the tactical missile grade IMU.

and amplified to consider the possible phase multipath rate error. The quality of a clock is characterized by its stability and Allan variance. The stability specifies the frequency offset of the clock and the Allan variance specifies its frequency variation. In terms of the phase rate variation, the Allan variance is used as a quality index [Allan]. The Allan variance of the XO (Trimble nine channel receiver) and simulated Rb sampled at 5 Hz are -9.4 Hz and -10.1 Hz in the log scale, respectively. Obviously, Rb is better than XO. For each Monte Carlo simulation, the differential clock drift of the XO is randomly selected from the measured data and of the Rb is simulated using van Dierendonck's 2-state clock model with Rubidium clock parameters.

To reduce the error of the estimate, the sampling rate of the phase rate measurement is set at 5 Hz. Monte Carlo simulations are conducted to obtain the corrected position error at the bubble exit for both inertial systems. Tables 4.2 and 4.3 summarize the Monte Carlo simulation results of the corrected position error at the bubble exit for the navigation grade and the tactical missile grade inertial systems, respectively.

Table 4.2: System Accuracy (Navigation Grade INS)

Clock	**Error**	**GPS Outage Time (min)**				**RMS**	**Mean**
	(m)	6	9	11	16	(m)	(m)
XO	y	1.28	1.39	1.29	1.31	1.32	-0.03
	z	1.87	2.08	2.01	2.27	2.05	-0.08
Rb	y	0.61	0.68	0.62	0.61	0.63	0.01
	z	1.24	1.05	1.32	1.28	1.21	0.05

Table 4.3: System Accuracy (Tactical Missile Grade IMU)

Clock	**Error**	**GPS Outage Time (min)**				**RMS**	**Mean**
	(m)	1	2	3	4	(m)	(m)
XO	y	1.10	1.41	1.37	1.33	1.31	0.01
	z	2.28	2.41	1.80	2.29	2.20	0.16
Rb	y	0.63	0.70	0.61	0.62	0.65	-0.02
	z	1.24	1.28	1.25	1.38	1.25	0.02

In Tables 4.2 and 4.3, y represents the cross track and z represents the vertical direction. For the navigation grade INS, refer to Table 4.2 and top plot of Fig. 4.5, the 3-PL's range rate-aiding method converges if the GPS outage time is less than 16 minutes, i.e. the initial position error covariance is less than $\sim$85 meters. For the tactical missile grade INS, the GPS outage time must be below 4 minutes, i.e. the initial position error covariance below $\sim$90 meters, for the 3-PL's range rate-aiding method to converge. Additionally, Tables 4.2 and 4.3 indicate that the system accuracy is insensitive to the DGPS outage time for each grade of INS and across grades. This means that the straight line assumption of the aircraft's trajectory when it is inside the bubble works very well for both grades of INS. Furthermore, the Root Mean Square (RMS) errors with respect to all outage times of both tables indicate that for the same grade of clock the system accuracy of both grades of INS remains the same, for the same grade of INS system accuracy varies with the grade of clock. This means that the system accuracy is dominated by the non-white clock drift rate residual. As the residual becomes smaller (the rubidium case), the position estimation error decreases dramatically.

Table 4.4: 3-PL's Range Rate-Aiding Accuracy

Accuracy	**X** (m)	**Y** (m)	**Z** (m)
Rb	0.62	0.67	1.27
XO	1.13	1.35	2.36

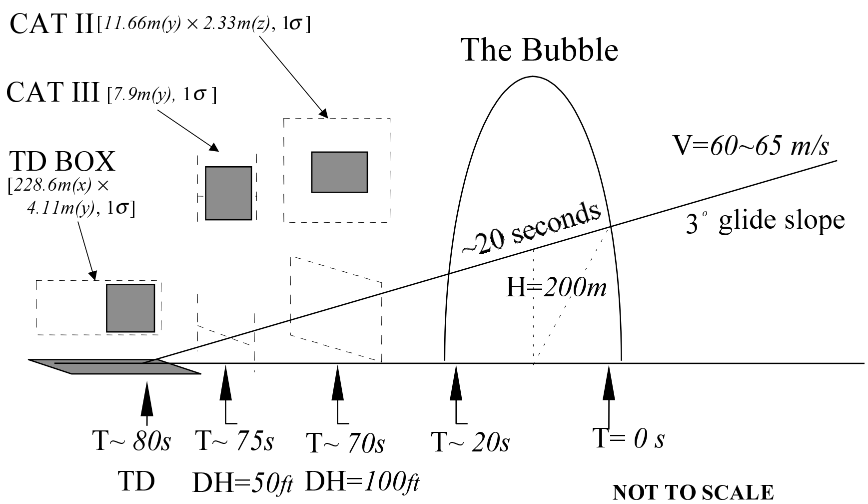

Figure 4.6: Landing Configuration of the 3-PLs/INS System.

Since the navigation grade INS and the tactical missile grade IMU do not significantly affect the accuracy of the 3-PL's range rate-aiding method and the only difference is the tolerable GPS outage time, the following uses the lumped accuracy of both grades as a measurement update in the covariance analysis. Table 4.4 summarizes the accuracy (1σ) of the 3-PL's range rate-aiding method.

4.3 Performance Evaluation

4.3.1 Simulation Setup

Figure 4.6. illustrates the landing configuration. Herein, the time that the aircraft

is inside the bubble is approximately 20 seconds as mentioned previously, while the time from the bubble exit to touchdown is within 60 seconds. Assume that the INS of the aircraft was calibrated by the DGPS during the flight. Several minutes before the aircraft enters the bubble, it loses GPS signals. Tables 4.2 and 4.3 summarize the allowable outage time for each INS grade. The longest outage time is used for the performance evaluation, i.e. 16 minutes for the navigation grade and 4 minutes for the tactical missile grade. Inside the bubble, the aircraft receives range rate measurements from the three non-synchronized PLs without a data link and satellite signals. At the bubble exit, after the aircraft obtains the position update from the 3-PL's range rate-aiding method, it navigates on the INS for 60 seconds until touchdown. This situation simulates the backup capability of the 3-PL's range rate-aiding method when either the differential system is down or the entire satellite GPS system is down. The INS performance is obtained using linear covariance method based on the error models derived in subsections 4.2.3 and 4.2.4.

Two cases, in terms of the clock quality, are considered below to demonstrate the influence of the clock quality on the performance of the 3-PL's range rate-aiding method. In each case, both the navigation grade and the tactical missile grade inertial systems are considered for comparison.

- Case 1: both the GPS receiver and the 3 PLs are assumed to be equipped with a rubidium clock.
- Case 2: both the GPS receiver and the 3 PLs are assumed to contain a quartz clock (typically used by current receivers.)

4.3.2 Evaluation Criteria

Two requirements are used to evaluate the performance of the integrated DGPS/INS system. First, the inner tunnel RNP [Kelly] specifies the 95% TSE for the landing system, which is shown in Fig. 4.6. Second, the NSE is used to specify the navigation sensor error of the Instrumental Landing System (ILS). Since the linear covariance analysis provides the position error due to the integrated navigation system, which is

Table 4.5: One Sigma **TSE** Requirements [Kelly]

TSE	**Along-track**(m)	**Cross-track**(m)	**Vertical**(m)
CAT I @200 ft	-	17.11	4.97
CAT II @100 ft	-	11.66	2.33
CAT III @50 ft	-	7.9	NA
Touchdown	228.6	4.11	-

Table 4.6: Experimental One Sigma **FTE** [Cohen, c]

FTE	**Along-track**(m)	**Cross-track**(m)	**Vertical**(m)
CAT I @200 ft	-	2.3**	1.15**
CAT II @100 ft	-	2.3	1.15
CAT III @50 ft	-	2.15	1.05
Touchdown	67.5	2.1	-

categorized as the NSE, therefore a derived NSE (NSE*, based on the TSE) is needed. Following, the derivation of the NSE* is given and both criteria are listed.

The Derived NSE (NSE*) criterion

The TSE is defined as

$$\sigma_{TSE}^2 = \sigma_{FTE}^2 + \sigma_{NSE}^2. \tag{4.5}$$

Table 4.5 specifies the required TSE for the precision approach and landing. In Table 4.5, "NA" means not available and "-" means not applicable. Since the covariance analysis only provides the error caused by the navigation sensor, the NSE must be derived to be a reference for the performance evaluation.

To specify the NSE criterion, the FTE of the airplane must first be specified, which is the CAT III 737 considered in the system. The FTE of a CAT III 737 is assumed to be the TSE of the 737 when using the IBLS to perform landings. Since the NSE of the IBLS system is within the sub-meter level [Cohen, c], it can be neglected from the TSE of the 737. Table 4.6 lists the FTE of a CAT III 737 [Cohen, b]. In Table 4.6, "-" means not applicable. "$**$" means that the CAT I FTE was not specified in [Cohen, c], therefore it is assumed to be identical to the CAT II FTE herein.

Table 4.7: One Sigma NSE* (TSE-Based) of a CAT III 737

NSE	**Along-track**(m)	**Cross-track**(m)	**Vertical**(m)
CAT I @200 ft	-	16.95	4.84
CAT II @100 ft	-	11.2	2
CAT III @50 ft	-	7.5	2**
Touchdown	92.2	3.5	-

Table 4.8: One Sigma NSE for the Instrumental Landing System

NSE	**Cross-track**(m)	**Vertical**(m)
CAT I @200 ft	10.2	2.2
CAT II @100 ft	3.69	0.93
CAT III @50 ft	2.67	0.32

Referring to Eqn. 4.5, the TSE-based NSE (NSE*) criteria for the integration filter can be obtained by subtracting the FTE (as shown in Table 4.6) from the TSE (as shown in Table 4.5) and is summarized in Table 4.7. "$**$" indicates that because no vertical TSE is specified at the decision height of 50 ft, it is impossible to compute the NSE based on this criterion. Therefore, the $2m$ NSE* at the decision height of 100 ft is also assumed to be valid at the decision height of 50 ft.

Table 4.7 provides the NSE* (a TSE-based NSE) criterion for the following performance evaluation.

The NSE criterion

Table 4.8 lists the NSE specified by the ICAO Annex 10 which is used to evaluate the angular ILS system with a center located around the threshold. Therefore, the accuracy requirement becomes stringent as the airplane approaches the runway. Any inertial based system has difficulty in meeting this requirement, because the inertial system drifts over time. The reason the NSE specifications are so tight is because it is assumed that the FTE of a human pilot or an autopilot is large. Nowadays, the FTE of the autopilot is fairly small (as the example shown in Table 4.6.) Therefore, relaxing NSE is a possible system trade-off as presented in the previous subsection.

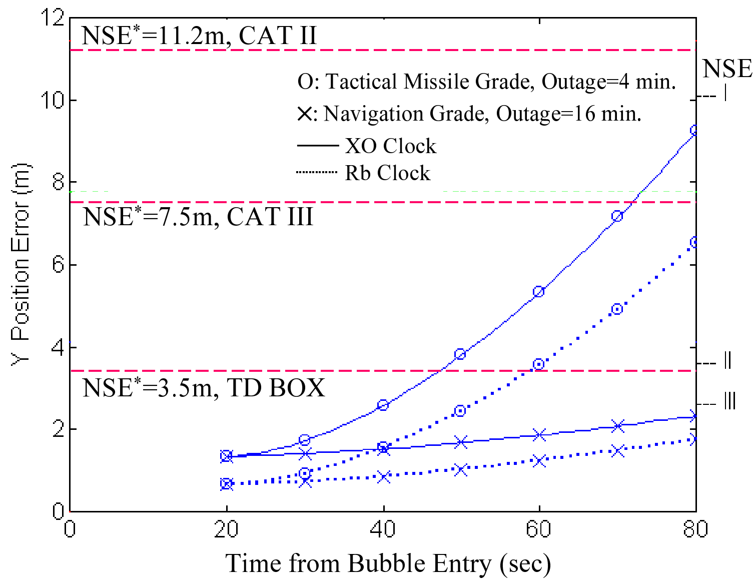

Figure 4.7: Cross-Track Position Error of Case 1 and 2.

4.3.3 Evaluation Results

Following the scenario setup described in subsection 4.3.1, the DGPS/INS performance of both grades before brief DGPS outages is calculated using the standard Kalman filter with the INS error model defined in subsection 4.2.3 and the WAAS position update specified in subsection 4.2.4. When DGPS outages occur, the INS alone performance is calculated via the propagation equation of the Kalman filter, as shown in Fig. 4.5. At the bubble exit, where the INS is updated by the 3-PL's range rate-aiding method, a measurement update of the Kalman filter is performed with the measurement quality specified in Table 4.4. Then, the INS alone performance is calculated again for 60 seconds. Figures 4.7 and 4.8 present the INS position errors (cross-track and vertical) for both Case 1 and Case 2 where the horizontal axis is the time from the bubble entry, the solid line denotes the results of the XO clock case and the dotted line represents those of the Rb clock case. Meanwhile, the symbol "$\times$" denotes the navigation grade INS and the symbol "o" denotes the tactical missile grade inertial system. Also, On the right-hand-side, I, II and III represent the required NSE of CAT I, II and III.

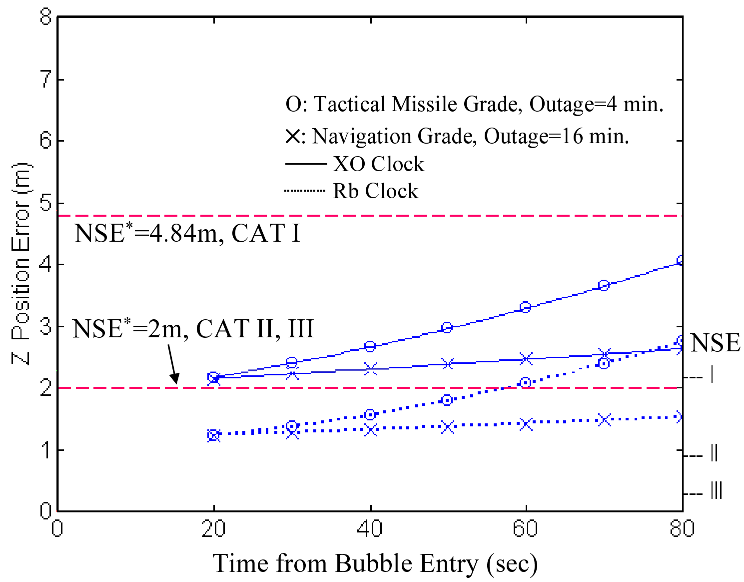

Figure 4.8: Vertical Position Error of Case 1 and 2.

Four levels of accuracy, i.e. CAT I, II, III and TD box, are evaluated herein. To land an aircraft, the TD box TSE is the dominant requirement that must be satisfied. When evaluating the INS performance, as shown in Figs. 4.7 and 4.8, with respect to the NSE* and NSE criteria, the 3-PLs/INS system satisfies the accuracy requirement only when the INS performance satisfies criterions in both directions. However, for the TD case, only the cross track satisfaction is needed since the vertical is no longer an issue. If the INS performance satisfies the NSE*, which means the airplane satisfies the required TSE, a "Yes" is filled in a blank under the TSE of the performance evaluation tables listed below. If the INS performance satisfies the NSE, a "Yes" is filled in a blank under the NSE of the performance evaluation tables.

- For the Case 1 (Rb clock):

  Comparing the results with the above NSE criteria, the performance in Table 4.9 can be summarized.

  When the aircraft loses GPS signals 16 minutes from touchdown, the navigation grade INS can satisfy the TD box TSE when updated by the 3-PLs/INS system with a rubidium clock. The tactical missile grade INS cannot satisfy the TD

Table 4.9: Case 1 (Rb clock) Performance Evaluation

INS Grade	**Meet Accuracy Requirements?**						
	CAT I		CAT II		CAT III		TD
	TSE	NSE	TSE	NSE	TSE	NSE	TSE
Tactical	Yes	No	No	No	No	No	No
Navigation	Yes	Yes	Yes	No	Yes	No	Yes

Table 4.10: Case 2 (XO clock) Performance Evaluation

INS Grade	**Meet Accuracy Requirements?**						
	CAT I		CAT II		CAT III		TD
	TSE	NSE	TSE	NSE	TSE	NSE	TSE
Tactical	Yes	No	No	No	No	No	No
Navigation	Yes	No	Yes	No	Yes	No	Yes

box TSE under the previously defined condition. However, when combined with the radar altimeter, which is currently used on all CAT III aircraft to provide accurate altitude, Fig. 4.7 (cross track) reveals that the tactical missile grade INS can satisfy the TD box TSE if the pure inertial navigation time is no more than 35 seconds from the update at the PL bubble exit.

- For the Case 2 (XO clock):

  Comparing the results with the above NSE criteria allows us to summarize the performance in Table 4.10.

  When using a quartz clock, with the same discontinuity condition as in Case 1, the navigation grade INS can satisfy the TD box when updated by the 3-PLs/INS system. Meanwhile, the tactical missile grade INS cannot satisfy the TD box TSE under the condition defined above. However, when combined with the radar altimeter, which is currently used on all CAT III aircraft to provide accurate altitude, Fig. 4.7 reveals that the tactical missile grade INS can satisfy the TD box TSE if the INS navigation time does not last more than 25 seconds from the update at the bubble exit.

Comparing the results of Case 1 and Case 2 (Figures 4.7 and 4.8) reveal that the clock quality influences the performance of the 3-PLs/INS system. However, in terms of the evaluation criteria, the effect of clock quality on the system performance evaluation results (Table 4.9 and Table 4.10) becomes insignificant when the system is equipped with a navigation grade INS. For the tactical missile grade system, the clock quality does influence the system capability to endure GPS outages.

4.4 Summary

This chapter introduces the 3-PLs/INS system. The knowns of this system include the inaccurate aircraft position and velocity, phase rate measurements from all 3 PLs, and the accurate position of all 3 PLs. The unknowns are the initial position and velocity errors of the aircraft, and the frequency offset and drift errors of the differential clock between the airborne receiver and all 3 PLs. In total, 12 unknowns. After the aircraft passes through the bubble, one can use the Doppler signals between the aircraft and 3 PLs to solve for the unknowns. Then one can calculate the aircraft's position at the bubble exit and update the INS for the ensuring motion. Combined with a navigation grade INS, this system can provide the accuracy required for precision landing without a data link and pseudolite synchronization, while satisfying the touchdown box TSE requirement. A situation when this system might be applied may be when total loss of GPS signals occurs during the final approach, when the standard GPS user wants to perform a precision landing, or when the 3-PLs/INS system is used as a backup.

Chapter 5

Differential Carrier Smoothed Ionosphere Delay

In LAAS applications, differential ionosphere delay has been ignored by assuming the local spatial decorrelation of the ionosphere delay is negligible, which is the foundation of the local area differential GPS. However, due to the recent developments of antenna technology for the reference station, the LAAS error budget has changed significantly. Therefore, this research aims to clarify the effect of the differential ionosphere delay on LAAS. It shows when the differential ionosphere delay is negligible and when it is not. When not negligible, it characterizes the differential ionosphere delay and investigates solutions.

5.1 Overview

Figure 5.1 illustrates four error sources included in the LAAS system: multipath, differential ionosphere, differential troposphere and receiver thermal noise. Below, both error source and processing method are discussed.

Multipath is the delayed satellite signal reflected from the ground or surroundings. For LAAS, both the ground reference station (the ground) multipath and the aircraft (the air) multipath must be considered. The ground multipath was the most significant error source (more than 1 meter at low elevation) [Dai]. The ground multipath

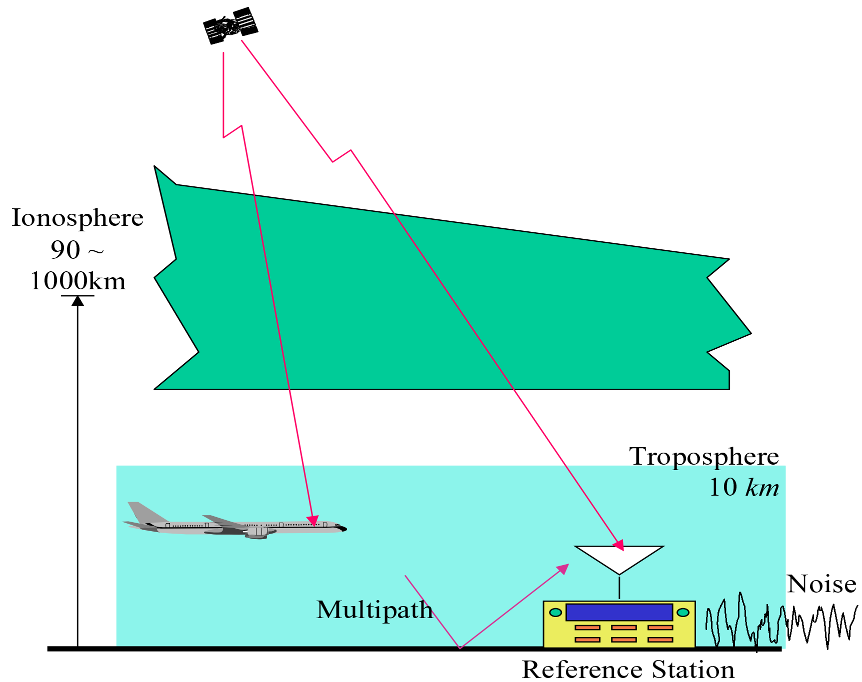

Figure 5.1: Error Sources of the LAAS System

is processed by hardware limiting (new antenna technology) and software filtering. The newly developed Multipath Limiting Antenna (MLA) provides high gains for low elevation satellites to increase the Signal to Noise Ratio (SNR) and a sharp gain cutoff at 5 degrees, rejecting all the reflected signals below 5 degrees [Hsiao], [van Graas, a]. These features allow MLA to significantly reduce the multipath error. Combining the MLA with software filtering, the current official algorithm is the CSC [Swider], the high frequency noise can be further reduced and a smoother signal provided. Thus, the current multipath error is considered to be 10-15 centimeters [van Graas, a].

Differential ionosphere is the path length difference between the ground and the air when the satellite signal penetrates through the ionosphere. This error source has been ignored by assuming that the ionosphere spatial decorrelation for the LAAS is negligible.

Differential troposphere is the path length difference between the ground and the air when the satellite signal penetrates through the troposphere. Differential troposphere is processed using a simplified homogeneous model to correct the index

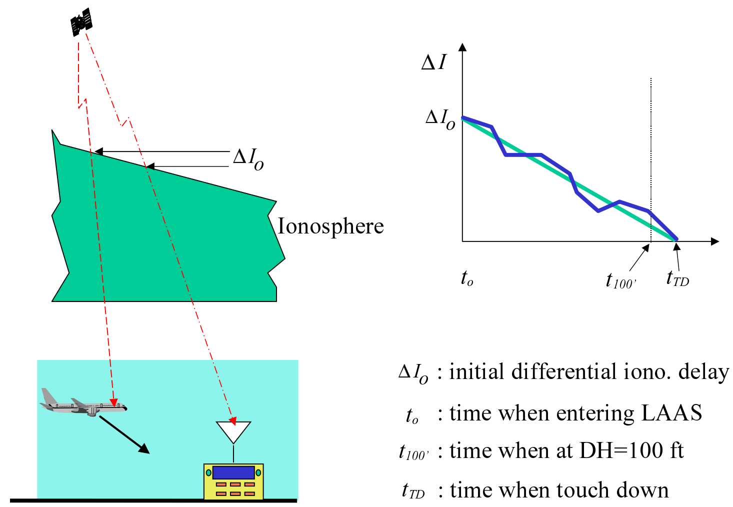

Figure 5.2: Illustration of the Differential Ionosphere Delay

of reflection [Lawrence]. Further improvement can be achieved if weather information is incorporated. Receiver thermal noise originates from the receiver hardware. This error resembles white noise and can be ignored if software filtering is applied.

In the following, the influence of the differential ionosphere error on the LAAS is investigated.

5.2 Effect of Carrier Smoothed Code on Differential Ionosphere Delay and Multipath

5.2.1 Differential Ionosphere Delay

The differential ionosphere delay is attributed to the spatial decorrelation of the ionosphere between the ground and the air as the ΔI_o illustrated in Fig. 5.2 .

For an approach, the Initial Approach Fix (IAF) is within 30 nm [WAASMOPS]. As the airplane approaches the runway, the spatial decorrelation of the ionosphere diminishes. At the touch down point which is typically within 1 mile of the reference station there is essentially no spatial decorrelation. Within 1 mile, the spatial decorrelation derived from the worst known case is less than 9 cm and is a constant.

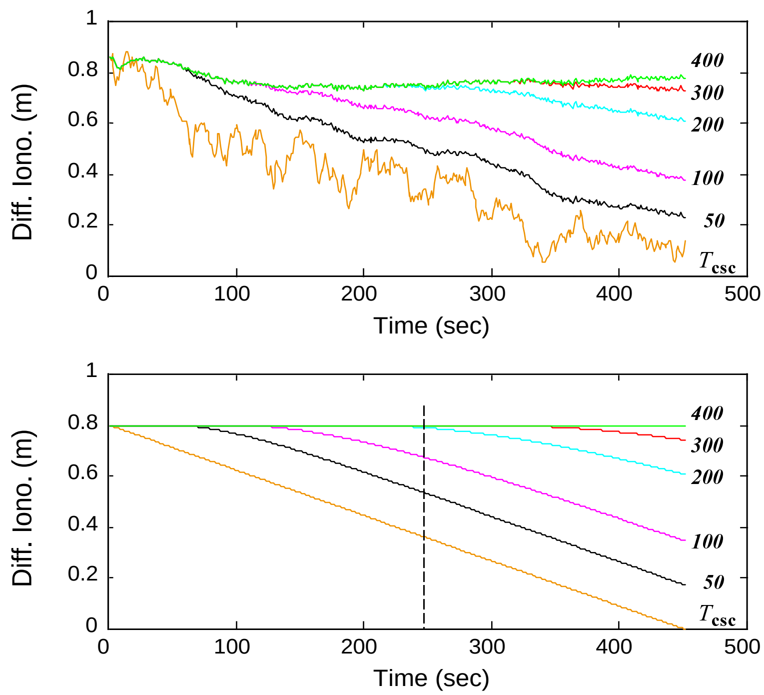

Figure 5.3: The Differential Carrier Smoothed Ionosphere Delay

Therefore, for the first order approximation, the spatial decorrelation between the reference station and the touchdown point can be neglected and the time histogram of ΔI resembles a triangle as depicted on the right portion of Fig. 5.2.

For CAT III landings, it is necessary to check the CAT III availability at the DH of 100 ft, which is approximately 600 m from TD, where the spatial decorrelation should not be a serious problem, say 3 centimeters, derived from the worst known case. Based on this analysis, the differential ionosphere error has assumed to be negligible for LAAS.

The influence of the CSC on the differential ionosphere delay and multipath is investigated below.

5.2.2 Effect of CSC on Differential Ionosphere Delay

Both the ground and the air receivers employ CSC to obtain a smoother pseudorange. Within the LAAS service area, the air receiver subtracts the carrier smoothed pseudorange correction broadcast from the ground to form a corrected pseudorange. Therefore, the differential ionosphere delay discussed in the previous section now becomes the differential carrier smoothed ionosphere delay. Figure 5.3 displays an example of the differential carrier smoothed ionosphere delay. The top figure in Fig. 5.3 presents the differential carrier smoothed ionosphere delay versus time with different carrier smoothing time constants, τ_{csc}, (from 0 to 400 seconds.) The initial differential ionosphere delay of 0.8 m over a 30nm baseline (14.4ppm) is not the worst case, but is worse than the average. The line with a zero time constant is the unsmoothed differential ionosphere delay with multipath. The figure shows how the CSC *delays* the differential ionosphere effect on LAAS. A longer time constant implies a more obvious delay. For the most popular carrier smoothing time constant of 100 seconds, at the DH of 100 ft, the differential ionosphere error has been increased from 1 centimeter to about 40 centimeters in this example. It is a **large** value when compared with the one sigma value of 10 to 15 centimeters of the carrier smoothed multipath. Therefore, a shorter carrier smoothing time constant is favored herein to prevent this delayed ionosphere error.

Another important issue is the length of the time delay due to the CSC. The bottom figure in Fig. 5.3 presents the differential carrier smoothed ionosphere error without multipath. A time delay of about twice the carrier smoothing time constant clearly exists, $2\tau_{\text{csc}}$. This delayed effect is derived in detail in Section 5.4.

As a result of this time delay, the equivalent spatial separation is the distance at the DH of 100 ft plus $2\tau_{\text{csc}}$ times the airplane velocity, i.e. approximately 15km.

The effect of the CSC on the multipath is now considered.

5.2.3 Effect of CSC on Multipath

CSC is originally used to reduce multipath error. Figure 5.4 displays an example of the effect of CSC on multipath.

The top figure in Fig. 5.4 presents the airborne multipath versus time collected from Moffett flight test. The bottom figure in Fig. 5.4 presents the carrier smoothed multipath versus time with different time constants. The figure clearly reveals that

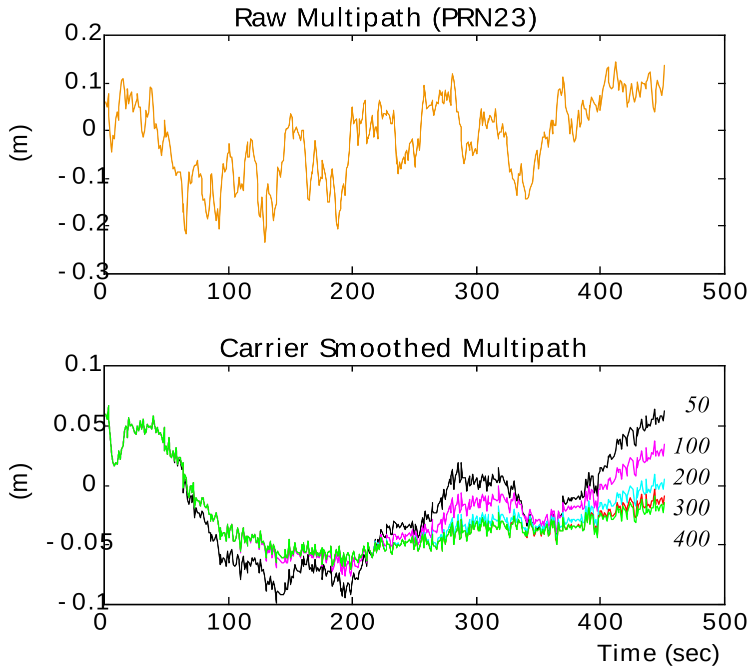

Figure 5.4: Example of the Carrier Smoothed Multipath

CSC significantly reduces the multipath as the carrier smoothing time constant increases. Therefore, a longer carrier smoothing time constant is preferred to reduce the multipath.

5.2.4 Summary

Comparing the results of the differential carrier smoothed ionosphere delay and the carrier smoothed multipath reveals opposite requirements on the carrier smoothing time constant. A longer carrier smoothing time constant is preferred to reduce the multipath error. Meanwhile, a shorter carrier smoothing time constant is preferred to reduce the differential carrier smoothed ionosphere delay. In terms of the system error, a method is necessary to balance the requirements on the carrier smoothing time constant. However, before examining the details of the solution, Sections 5.3 and 5.4 provides further insights into the differential carrier smoothed ionosphere delay.

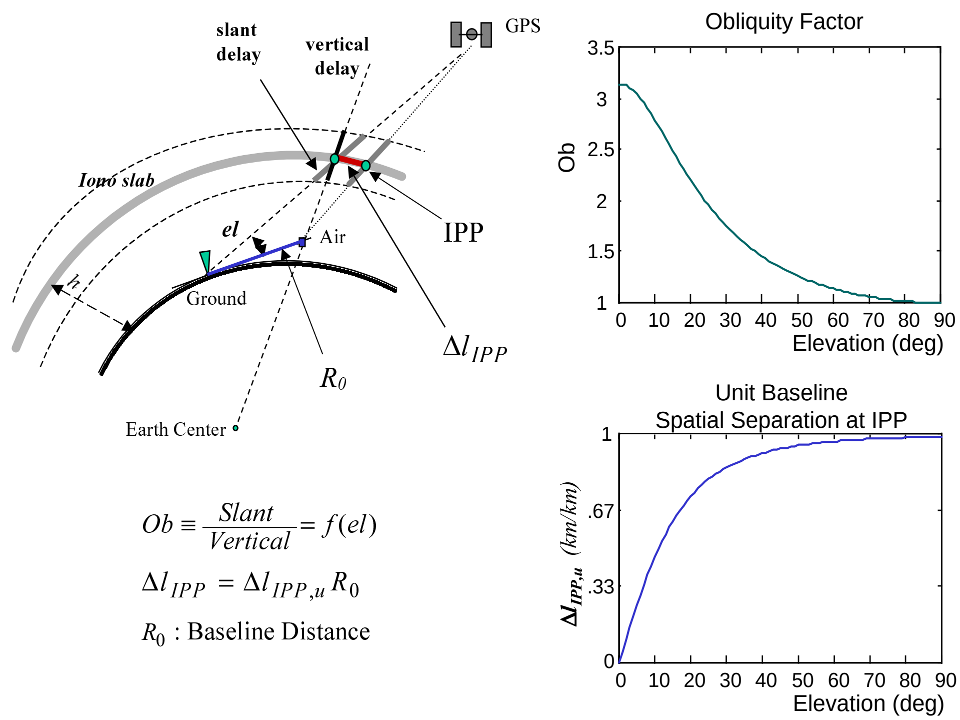

Figure 5.5: Illustration of the Ionosphere Model

5.3 Differential Ionosphere Delay Modeling

The ionosphere can be modeled as a thin slab with vertical delays at a height of 350km above the reference geoid as illustrated in Fig. 5.5 [Chao]. Since the measured ionosphere delay is the slant delay, a relationship between the slant delay and the vertical delay is necessary and this relation is defined as the obliquity factor, Ob, which can be expressed as

$$Ob(el) = \frac{I_{slant}}{I_{vertical}}. \tag{5.1}$$

From the left figure in Fig. 5.5, Ob obviously varies with elevation, el. At low elevations, Ob is larger than 1, and at high elevations, Ob is approximately 1. The calculated value of Ob, as displayed in the right top figure of Fig. 5.5, ranges between 3 and 1 as the elevation increases.

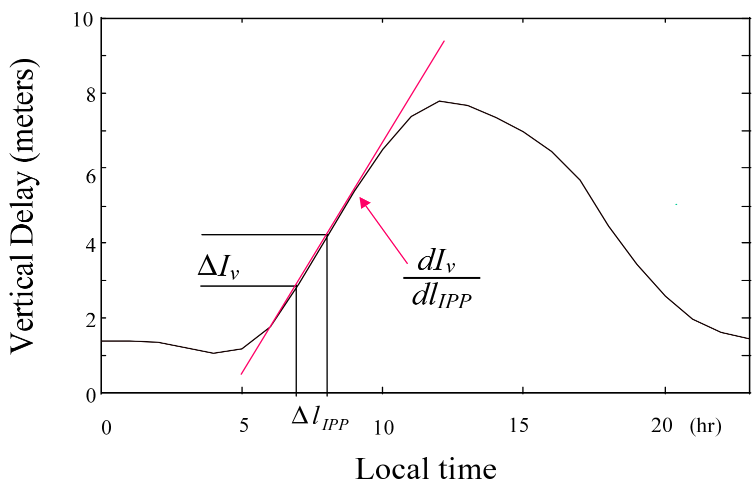

Figure 5.6: Example of Diurnal Variation of Ionosphere Vertical Delay

For the differential ionosphere, two features are worth mentioning: the Ionosphere Pierce Point (IPP) distance and the vertical spatial gradient. The IPP is defined as the intersection of the ionosphere slab and the line between the user receiver and a GPS satellite. The IPP distance, displayed as Δl_{IPP} in the left figure of Fig. 5.5, is defined as the distance between the IPPs of the ground and the air .

For a 2-D case, the IPP distance is a function of satellite elevation and is proportional to the baseline distance (shown as R_0). Meanwhile, for a unit baseline (subscript u), the variation of the unit IPP distance, $\Delta l_{IPP,u}$, versus elevation is illustrated in the right bottom figure of Fig. 5.5. The variation ranges from 0, when the satellite is at zero elevation, to almost 1, when the satellite reaches its zenith.

For the spatial gradient, both the longitudinal and the lateral gradients are included. Figure 5.6 illustrates an example of diurnal variation of the ionosphere vertical delay. Since it is assumed herein that the ionosphere changes slowly, the longitudinal spatial gradient could be approximated by the slope of the measured vertical ionosphere delay, as shown in Fig. 5.6. This figure shows that the peak rate of change occurs in the late morning. For the lateral spatial gradient, aligned lateral reference stations are needed to take measurements.

Following the definition of the obliquity factor, as defined in Eqn. 5.1, and the idea of the vertical spatial gradient, as shown in Fig. 5.6, the 2-D differential (slant) ionosphere delay, ΔI, can be expressed as

$$\Delta I = I_a - I_g \approx \underbrace{\frac{dI_v}{dx_{IPP}}}_{\text{Spatial gradient}} \underbrace{Ob\Delta l_{IPP,u}}_{\text{Geometry factor}} \underbrace{R_0}_{\text{Baseline}} \tag{5.2}$$

where $\frac{dI_v}{dx_{IPP}}$ represents the vertical spatial gradient and $Ob\Delta l_{IPP,u}$ is defined as the geometry factor. In short, the differential slant ionosphere delay can be modeled as the product of the vertical spatial gradient, the geometry factor and the baseline.

5.4 Derivation of Differential Carrier Smoothed Ionosphere Decorrelation and Divergence on LAAS

GPS code phase and carrier phase measurement equations for both the ground and the air can be written as follows.

The ground measurements:

$$\rho^j_{g,k} = S^j_{g,k} + b_{g,k} - B^j_k + I^j_{g,k} + T^j_{g,k} + m^j_{g,k} + \nu^j_{g,k} \tag{5.3}$$

$$\phi^j_{g,k} = S^j_{g,k} + b_{g,k} - B^j_k - I^j_{g,k} + T^j_{g,k} + N^j_j + m^{j,\phi}_{g,k} + \nu^{j,\phi}_{g,k}. \tag{5.4}$$

The air measurements:

$$\rho^j_{a,k} = S^j_{a,k} + b_{a,k} - B^j_k + I^j_{a,k} + T^j_{a,k} + m^j_{a,k} + \nu^j_{a,k} \tag{5.5}$$

$$\phi^j_{a,k} = S^j_{a,k} + b_{a,k} - B^j_k - I^j_{a,k} + T^j_{a,k} + N^j_j + m^{j,\phi}_{a,k} + \nu^{j,\phi}_{a,k}. \tag{5.6}$$

Consider the error of the code phase as a linear combination of the ionosphere

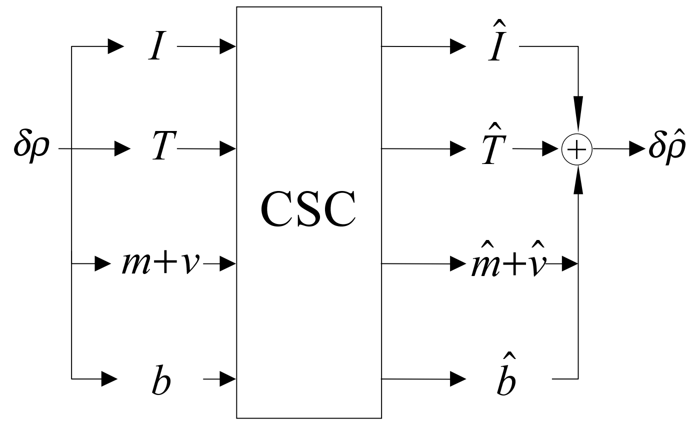

Figure 5.7: Error Components of the Code Phase Error

delay I, troposphere delay T, multipath m, user clock b and receiver noise ν. This is presented in Fig. 5.7 where the ephemeris error and the satellite clock error B are not included due to the common view of satellites between the airborne user and the reference station in the local differential consideration.

The carrier smoothed code can be formulated as

$$\widehat{\rho}_k = \frac{L-1}{L}\left(\widehat{\rho}_{k-1} + \phi_k - \phi_{k-1}\right) + \frac{1}{L}\rho_k \tag{5.7}$$

where $\widehat{\rho}_k$ is the carrier smoothed pseudorange at epoch k; $LT_s = \tau$, the carrier smoothing time constant; and T_s is the sampling time.

For the ionosphere delay I, ρ_k with I_k and ϕ_k can be replaced with $-I_k$, producing

$$\widehat{I}_k = \frac{L-1}{L}\left(\widehat{I}_{k-1} - I_k + I_{k-1}\right) + \frac{1}{L}I_k \tag{5.8}$$

where $\widehat{I}_k$ represents the carrier smoothed ionosphere delay at epoch k.

Linearizing I_k with respect to time step $k-1$ and position $\mathbf{x}_{k-1}$, after rearrangement, produces

$$I_{k-1} = I_k - \frac{\partial I}{\partial t}T_s - \frac{\partial I}{\partial \mathbf{x}}\Delta\mathbf{x}_{k-1} - H.O.T. \tag{5.9}$$

where $\Delta\mathbf{x}_{k-1} = \mathbf{v}_{k-1}T_s$.

Substituting Eqn. 5.9 into Eqn. 5.8 for both I_{k-1} and $\widehat{I}_{k-1}$, after rearrangement, we have

$$\widehat{I}_k = I_k - (L-1)\,T_s\left[\left(\frac{\partial \widehat{I}}{\partial t} + \frac{\partial I}{\partial t}\right) + \left(\frac{\partial \widehat{I}}{\partial \mathbf{x}} + \frac{\partial I}{\partial \mathbf{x}}\right)\mathbf{v}_{k-1}\right] \tag{5.10}$$

where $(L-1)\,T_s = \tau - T_s$.

For a very slow signal like the ionosphere delay, the following approximation is valid,

$$\frac{\partial \widehat{I}}{\partial t} = \frac{\partial I}{\partial t} \qquad \text{and} \qquad \frac{\partial \widehat{I}}{\partial \mathbf{x}} = \frac{\partial I}{\partial \mathbf{x}}. \tag{5.11}$$

Therefore, Eqn. 5.10 can be rewritten and the carrier smoothed ionosphere delay can be obtained as

$$\widehat{I}_k = I_k - 2\,(\tau - T_s)\left[\frac{\partial I}{\partial t} + \frac{\partial I}{\partial \mathbf{x}}\mathbf{v}_{k-1}\right]. \tag{5.12}$$

For the ground reference station, the velocity $\mathbf{v}_{k-1}$ is zero, therefore, the ground carrier smoothed ionosphere delay, $\widehat{I}_{g,k}$, is

$$\widehat{I}_{g,k} = I_{g,k} - 2\,(\tau_g - T_s)\,\frac{\partial I_g}{\partial t}. \tag{5.13}$$

Meanwhile, for the airborne user, the airborne carrier smoothed ionosphere delay,

$\widehat{I}_{a,k}$, is

$$\widehat{I}_{a,k} = I_{a,k} - 2\left(\tau_a - T_s\right)\frac{\partial I_a}{\partial t} - 2\left(\tau_a - T_s\right)\frac{\partial I_a}{\partial \mathbf{x}}\mathbf{v}_{a,k-1}. \tag{5.14}$$

In the local area, $I_{a,k}$ can be linearized with respect to $I_{g,k}$, hence

$$I_{a,k} = I_{g,k} + \frac{\partial I}{\partial \mathbf{x}}\mathbf{x}_{a,k} + H.O.T.. \tag{5.15}$$

where $\mathbf{x}_{a,k}$ represents the user position vector with respect to the reference station. Furthermore, it can be assumed that

$$\begin{aligned} \frac{\partial I_a}{\partial t} &= \frac{\partial I_g}{\partial t} = \frac{\partial I}{\partial t} \\ \frac{\partial I_a}{\partial \mathbf{x}} &= \frac{\partial I}{\partial \mathbf{x}}. \end{aligned} \tag{5.16}$$

Plugging Eqn. 5.15 and Eqn. 5.16 into Eqn. 5.14 gives the carrier smoothed ionosphere delay of the airborne user with respect to the ground station as

$$\widehat{I}_{a,k} = I_{g,k} + \frac{\partial I}{\partial \mathbf{x}}\mathbf{x}_{a,k} + 2\left(\tau_a - T_s\right)\frac{\partial I}{\partial t} + 2\left(\tau_a - T_s\right)\frac{\partial I}{\partial \mathbf{x}}\mathbf{v}_{a,k}. \tag{5.17}$$

Subtracting Eqn. 5.13 from Eqn. 5.17, the differential carrier smoothed ionosphere delay can be written as

$$\begin{aligned} \Delta\widehat{I}_k &\triangleq \widehat{I}_{a,k} - \widehat{I}_{g,k} \\ \Delta\widehat{I}_k &= 2\left(\tau_g - \tau_a\right)\frac{\partial I}{\partial t} + \frac{\partial I}{\partial \mathbf{x}}\left[\mathbf{x}_{a,k} - 2\left(\tau_a - T_s\right)\mathbf{v}_{a,k-1}\right] \\ \Delta\widehat{I}_k &= 2\left(\tau_g - \tau_a\right)\frac{\partial I}{\partial t} + \frac{\partial I}{\partial \mathbf{x}_{IPP}}\frac{\partial \mathbf{x}_{IPP}}{\partial \mathbf{x}}\left[\mathbf{x}_{a,k} - 2\left(\tau_a - T_s\right)\mathbf{v}_{a,k-1}\right]. \end{aligned}$$

When combined with Eqn. 5.1, we can also obtain

$$\Delta\widehat{I}_k = Ob\ 2\left(\tau_g - \tau_a\right)\frac{\partial I_v}{\partial t} + \underbrace{\frac{\partial I_v}{\partial \mathbf{x}_{IPP}}}_{\text{Spatial gradient}} \underbrace{Ob\frac{\partial \mathbf{x}_{IPP}}{\partial \mathbf{x}} \underbrace{\left[\mathbf{x}_{a,k} - \mathbf{2}\left(\tau_a - T_s\right)\mathbf{v}_{a,k-1}\right]}_{\text{Lengthened baseline vector}}}_{\text{Geometry factor} \times \text{Baseline}} \tag{5.18}$$

where

$$\frac{\partial I_v}{\partial t} = \text{the vertical ionospheric temporal gradient.} \tag{5.19}$$

$$\frac{\partial I_v}{\partial \mathbf{x}_{IPP}} = \text{the vertical ionospheric spatial gradient.} \tag{5.20}$$

$$\frac{\partial \mathbf{x}_{IPP}}{\partial \mathbf{x}} = \text{the Jacobian between the user baseline } \mathbf{x}_k \text{ and the IPP baseline } \mathbf{x}_{IPP,k}. \tag{5.21}$$

Equation 5.18 reveals that the differential carrier smoothed ionosphere delay includes two parts:

- The ionosphere time variation:

  The time variation effect will appear if the ground and the air use different carrier smoothing time constants. This fact provides an additional trade-off when considering different time constants for the air and the ground.

- The ionosphere spatial variation:

  The spatial gradient effect, has a delayed effect, or a lengthened baseline, after the CSC is applied. The lengthened baseline is twice the carrier smoothing time constant, times the aircraft velocity, plus the airplane position. This is the essence of the problem. Compared to the 2-D case, Eqn. 5.2, the last curled bracket is equivalent to the Geometry Factor times the baseline.

The following summarizes the assumptions made in the above derivation.

- Assume that the ionosphere varies slowly in time and space. Therefore, the time and the spatial gradients of the carrier smoothed ionosphere delay have the same gradients as the unsmoothed ionosphere, i.e., $\frac{\partial \widehat{I}}{\partial t} = \frac{\partial I}{\partial t}$ and $\frac{\partial \widehat{I}}{\partial \mathbf{x}} = \frac{\partial I}{\partial \mathbf{x}}$.

- Assume that the time variation of the ionosphere delay in a local area is the same for both the ground and the air, $\frac{\partial I_a}{\partial t} = \frac{\partial I_g}{\partial t}$. Restated, the time variation of the differential ionosphere delay is zero.

5.5 Frequency Domain Description of the CSC

This section describes the frequency domain characteristics of the CSC for both the ionosphere and multipath delays.

5.5.1 Ionosphere Delay

Rearranging Eqn. 5.8, the transfer function between the carrier smoothed ionosphere delay $\widehat{I_k}$ and the ionosphere delay I_k can be written as follows,

$$\frac{\widehat{I_k}}{I_k} = \frac{-\frac{L-2}{L} + \frac{L-1}{L}z^{-1}}{1 - \frac{L-1}{L}z^{-1}}. \tag{5.22}$$

For the very low frequency response, where $z^{-1} \sim 1$, $\frac{\widehat{I_k}}{I_k} \sim 1$, i.e., the magnitude and phase of the output is the same as the input. Meanwhile, for the high frequency response, where $z^{-1} \sim 0$ and therefore $\frac{\widehat{I_k}}{I_k} \sim -1 + \frac{2}{L}$, the magnitude of the output is approximately the same as the input (since L is large in general) but out of phase. For frequencies in between, the frequency response can be found in the example Bode plot of Eqn. 5.22 with a carrier smoothing time constant of 100 seconds as displayed in Fig. 5.8 . Figure 5.8 reveals that the CSC on the ionosphere delay is basically an all-pass filter with different time delays on different frequencies.

In the LAAS application, ionospheric delay can be treated as a signal with a constant bias plus a triangular signal (as illustrated in Fig. 5.2.) When applying the CSC to the ionosphere signal, the constant bias responds corresponding to the low frequency portion of Fig. 5.8. The triangle signal, in the LAAS service area (about 10 to 15 minutes before touchdown), corresponds to the middle frequency (around 10^{-3} Hz) response of Fig. 5.8, and thus will have a similar magnitude to the

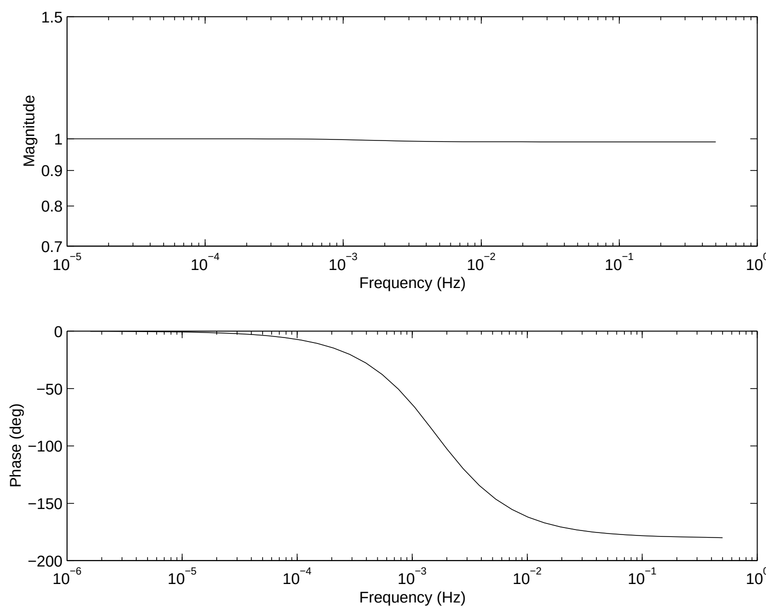

Figure 5.8: Example Bode Plot of the CSC on the Ionosphere Delay with a Carrier Smoothing Time Constant of 100 Seconds.

unsmoothed ionosphere delay, but with time delay. This relationship validates the assumption made in Section 5.4. Besides, some high frequency components exist in the ionosphere delay, generally known as scintillation. These components are small in terms of amplitude and change sign (phase=180^o as shown in Fig. 5.8) when CSC is applied. Therefore, scintillation is not a major concern in a code phase-based positioning system.

5.5.2 Multipath Delay

Since the carrier phase multipath is considerably smaller than the code phase multipath, the following derivation ignores the carrier phase multipath. Rearranging Eqn. 5.7, and replacing ρ with m, the equation of the CSC on the multipath can be rewritten as

$$\widehat{m}_k = \frac{L-1}{L}\widehat{m}_{k-1} + \frac{1}{L}m_k \tag{5.23}$$

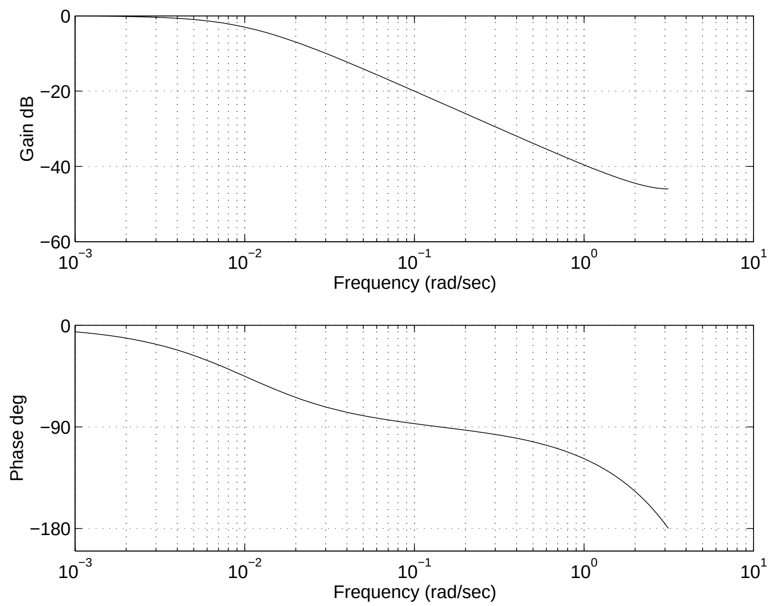

Figure 5.9: Example Bode Plot of the CSC on the Multipath Delay with a Carrier Smoothing Time Constant of 100 Seconds

and the transfer function can be expressed as

$$\frac{\widehat{m}_k}{m_k} = \frac{\frac{1}{L}}{1 - \frac{L-1}{L} z^{-1}}. \tag{5.24}$$

Equation 5.23 is essentially the discrete-time counterpart of a continuous-time low-pass filter,

$$L\dot{\hat{m}} + \hat{m} = m,$$

sampled at 1 Hz. Therefore, the effect of the CSC on the multipath retains all the characteristics of a low pass filter and the carrier smoothing time constant is the same as the time constant of the low pass filter. Figure 5.9. presents an example Bode plot of the CSC with a carrier smoothing time constant of 100 seconds. The cutoff frequency clearly corresponds to the inverse of the carrier smoothing time constant. Thus, a larger carrier smoothing time constant implies a smoother pseudorange.

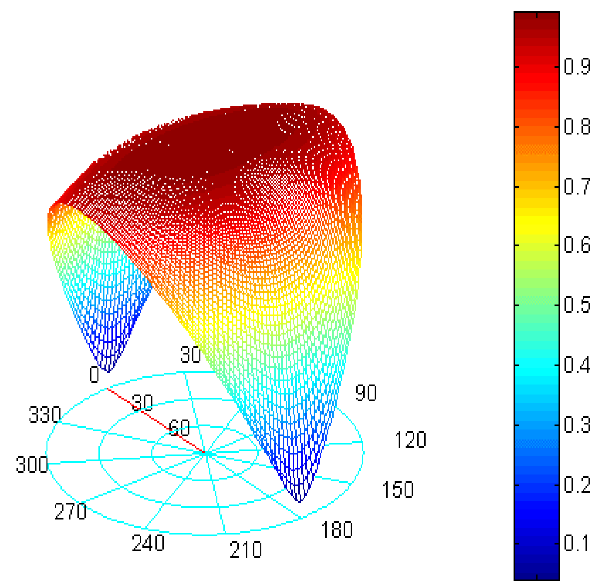

Figure 5.10: Unit Baseline IPP distance: Normalized IPP distance as a function of satellite azimuth and elevation.

5.6 IPP Distance & Geometry Factor

Based on the previous 2-D analysis and the analytical solution, Eqn. 5.18, the idea of the unit IPP distance and the geometry factor can be extended to the real (3-D) world for further investigation.

Figure 5.10 displays calculations of the 3-D unit IPP distance versus the azimuth and the elevation angles of a satellite. The baseline is along the zero degree line. When the satellite is along the baseline, the unit IPP distance varies from 0 to almost 1, agreeing with the 2-D's result. Meanwhile, when the satellite is across the baseline, the unit IPP distance is almost one for all elevation angles.

Following the previously defined geometry factor, the product of the obliquity factor and the unit IPP distance as presented in Eqn. 5.2, the 3-D geometry factor is calculated and presented in Fig. 5.11 . The geometry factor represents the sensitivity to spatial gradients in the ionosphere. As can be seen from the figure, the magnification due to the geometry factor can be as much as 2.8, which is significant. This fact

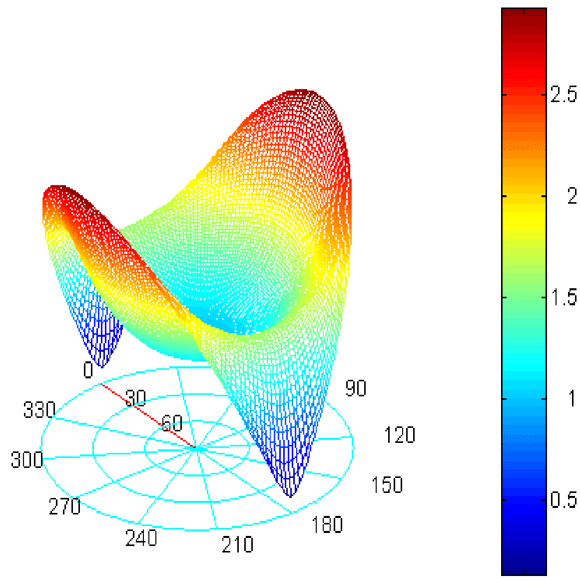

Figure 5.11: Geometry Factor versus Azimuth and Elevation.

means if the ionosphere gradient is along the baseline vector and the satellite is across the baseline at low elevation, then the differential carrier smoothed ionosphere delay will be 2.8 times the ionosphere gradient times the baseline. For the Wanninger case, the ionosphere gradient is about 0.05m/km, the baseline is about 15km, as mentioned above, and the differential carrier smoothed ionosphere delay can reach 2.1 meters in the range domain. Notably, this is attributed to the carrier smoothing time constant of one hundred seconds. For longer time constants, as widely discussed in the LAAS community, the effect of the differential carrier smoothed ionosphere delay would be more severe. The differential carrier smoothed ionosphere delay can not be ignored compared to the carrier smoothed multipath error of around 10 to 15 centimeters.

5.7 Effect on CAT III Availability

Since the preceding sections have revealed how the carrier smoothed code affects the differential ionosphere delay, this section investigates how the Differential Carrier Smoothed Ionosphere Delay (DCSID) affects the CAT III availability of the

LAAS. The LAAS is considered available when the predicted Vertical Protection Limit (VPL) is less than the required CAT III Vertical Alarm Limit (VAL).

The following subsections defines the availability, the predicted VPL, ionosphere gradients and the threat illustration case, then investigate the impact of the DCSID on the LAAS availability.

5.7.1 Availability

The CAT III Availability considered herein is the probability of the computed VPL that satisfies the required CAT III VAL for all space vehicle (SV) operational states (number of working SVs) of a given GPS constellation. The computation methodology is adopted from the availability defined by Phlong [Phlong] to account for both poor satellite geometries and satellite outages, and can be expressed as

$$\begin{aligned} A(VAL) &= \Pr(VPL \leq VAL) \\ &= \sum_{i=0}^{24} P_i^{GPS} A_i(VAL) \\ &= 1 - \sum_{i=0}^{24} P_i^{GPS} U_i(VAL) \end{aligned} \tag{5.25}$$

where

$$\begin{aligned} A_i(VAL) &= \Pr[VPL \leq VAL | (24-i) \text{ GPS})] \text{ (conditional availability)} \\ P_i^{GPS} &= \Pr(24-i \ \text{ usable GPS SVs}) \text{ (GPS operational probability)} \\ U_i(VAL) &= 1 - A_i(VAL) \text{ (conditional unavailability)}. \end{aligned}$$

Notably, in Phlong's definition, availability is also a function of the number and states of the ground segment (GS). Since the GS is a minor influence on the availability and LAAS will have redundant GSs, the subsequent analysis neglects the effect of the GS.

The GPS operational probability, P_i^{GPS}, including three types of outage mechanisms: long-term failures, short-term failures and maneuvers and can be found in [Phlong]. Table 5.1 lists several major GPS operational probability values for reference.

Table 5.1: GPS Operational Probabilities

No. of GPS SVs Operational	No. of GPS SVs Failed (i)	Probabilities $\left(P_i^{GPS}\right)$
24	0	7.00547e-01
23	1	2.36891e-01
22	2	5.03927e-02
21	3	1.00046e-02

The CAT III availability requirement is .999. To demonstrate the availability threat, the problem is demonstrated using the unavailability. The time of unavailability during a day is defined as when the computed VPL, which includes the differential carrier smoothed ionosphere delay effect, exceeds the required VAL. According to the CAT III requirement, the permitted unavailable time should be less than 86.4 seconds or 1.44 minutes.

5.7.2 Vertical Protection Limit

VPL, a computed position error upper bound of the airborne user, is used to indicate whether the LAAS is available for precision approach and landing within the integrity and the continuity requirements or not. This bound can be determined using the estimated error parameters provided by the ground and the estimates of fault-free airborne receiver performance.

The VPL equation applied in the following analysis is the predicted VPL, $VPL_{predict}$, which is one of the VPL equations of the LAAS integrity monitoring system selected by RTCA SC-159. $VPL_{predict}$ is calculated before each approach to predict whether the LAAS system with that user's geometry satisfies the continuity requirements based on the assumption that a fault exists in one or more of the measurements made by one of the reference receivers. $VPL_{predict}$ is listed as [Liu]:

$$\begin{aligned} VPL_{predict} &= \frac{k_{FFD/M}}{\sqrt{M(M-1)}}\sqrt{\sum_{i=1}^{N} S_{zi}^2 \sigma_{gnd}^2(i)} \\ &\quad + k_{MD}\sqrt{\sum_{i=1}^{N} S_{zi}^2 \left(\frac{\sigma_{gnd}^2(i)}{M-1} + \sigma_{air}^2(i)\right)} \end{aligned} \tag{5.26}$$

where M denotes the number of the reference receivers; $\sigma_{gnd}(i)$ represents the estimated noise level of the i^{th} satellite from the reference receiver measurement and $\sigma_{air}(i)$ represents the estimated noise level of the i^{th} satellite from the airborne receiver measurement; N denotes the number of in-view satellites; $k_{FFD/M}$ represents the multiplier which determines the probability of fault-free detection given M reference receivers; k_{MD} is the multiplier which determines the probability of missed detection given one reference receiver is faulted; and S_{zi} is described below.

S is a matrix relation between the pseudorange domain (ρ) and the position domain ($\mathbf{X}$), i.e. $\mathbf{X} = S\rho$, and is listed as

$$S = \left(H^* W H\right)^{-1} H^* W. \tag{5.27}$$

S_{zi} is the i^{th} element of the third row (vertical) of S.

The weighting matrix W is a diagonal matrix according to the estimated total pseudorange noise (σ_{pr}) seen by the airborne user. W is given by

$$W = diag[\sigma_{pr}^{-2}(1) \cdots \sigma_{pr}^{-2}(i) \cdots \sigma_{pr}^{-2}(N)]. \tag{5.28}$$

where σ_{pr} is composed of the pseudorange correction error from the M ground receivers and the pseudorange measurement error from the airborne receiver. Hence, it is expressed by

$$\sigma_{pr}^2(i) = \frac{1}{M}\sigma_{gnd}^2(i) + \sigma_{air}^2(i). \tag{5.29}$$

Table 5.2: Severe Ionospheric Gradients

Source	**Place**	**Observation**	**Gradient**
Goad	The Arctic	0.5 m over a 9 km latitudinal baseline	0.0556 m/km
Wanninger	Brazil	March 1993, SSN=69.8, observed 5 m over a 100 km latitudinal baseline	0.05 m/km
	Hamilton, MA	April 1979, SSN=101.5, observed anomaly is 0.11 $m/\min$ (read from chart)	0.11 $m/\min$
Doherty	Fairbanks, AK	0.2% of observed temporal gradients are over 0.7 $m/\min$	0.7 $m/\min$

For the case of three reference receivers considered herein, i.e. $M = 3$, the probability multipliers for CAT III are $k_{FFD/M}$ is 5.104 and k_{MD} is 4.315 [Liu].

To investigate the effect of DCSID on CAT III availability, $\sigma^2_{air}(i)$ is modified to incorporate the uncertainty caused by the DCSID in the analysis below.

5.7.3 Numerical Value of the Ionospheric Gradients

The ionospheric gradient depends on the solar cycle, geomagnetic activity of the earth, and location and time of a day of the observation. The solar cycle is measured by the Sun Spot Number (SSN). The ionosphere is assumed to vary slowly within 15 minutes. For the LAAS application, the approach time is approximately 8 to 10 minutes. Therefore, the ionosphere remains static during an approach. For a static ionosphere, the time variation of the ionosphere is equivalent to the spatial variation. Namely, the longitudinal spatial gradient can be approximated by the time variation of the ionosphere. Table 5.2 lists several severe vertical ionospheric gradients shown in previous literature.

In Table 5.2, all studies except Doherty were single-valued observations. For a statistical analysis, Doherty's statistical data are used in the following.

For the averaged nominal vertical gradient, refer to [Doherty], Table 5.3 can be obtained by chart reading. In Table 5.3, cdf represents the cumulative probability density function. Averaging the data listed in Table 5.3, a nominal ionospheric gradient of 0.04 $m/\min$ can be obtained, bounding the probability between 1% and

Table 5.3: Nominal Temporal Gradients at Various Locations

Place	**Observation**	$\vert$**@1%cdf**$\vert$	**@99%cdf**
Westford, MA	March 1993, SSN=69.8	0.06 $m/\min$	0.05 $m/\min$
Hamilton, MA	March 1983, SSN=66.5	0.04 $m/\min$	0.03 $m/\min$
	March 1989, SSN=131.4	0.04 $m/\min$	0.05 $m/\min$
Albert Head, BC	March 1993, SSN=69.8	0.03 $m/\min$	0.04 $m/\min$
	March 1993, SSN=69.8, Magnetically quiet	0.03 $m/\min$	0.04 $m/\min$

99%.

The above severe and the nominal gradients can be converted to the spatial gradient unit via the following relation:

$$1\min = \frac{2\pi}{24(hr)\times 60(\min)} \times R_e(km) \times \cos(L) \tag{5.30}$$

where R_e represents the radius of the earth, and L represents the latitude of the ionosphere observation location. When at the equator, $1\min = 27.83\ km$.

To obtain the sigma value of the DCSID effect to calculate the $VPL_{predict}$ as mentioned in the previous section, the statistical characteristics of the ionospheric gradients are assumed to be a normal distribution. For a normal distribution with a zero mean and a sigma value of one, the multiplier ($k_{nominal}$) that bounds the probability level between 1% and 99% is 2.3263, and the multiplier (k_{severe}) that bounds the probability level between 0.1% and 99.9% is 3.0902. Therefore, the corresponding sigma values of the ionospheric gradient that bound the severe and the nominal probability levels can be obtained for the availability analysis.

The Severe Ionospheric Gradient

The severe ionospheric gradient in Table 5.2 presented by Doherty is 0.7 m/min observed at Fairbanks, AK (its latitude is around 66^o North.) Referring to Eqn. 5.30 and k_{severe} in the last section, the sigma value of the severe vertical ionospheric gradient ($\sigma_{severe/km}$) can be obtained as 0.02 m/km. as Fairbanks is known to be in the sub-aurora area where the ionosphere has strong gradients. To obtain $\sigma_{severe/km}$

for all CAT III airports across the US, the severe gradient is converted to the equator, thus, $\sigma_{severe/km}$ is equal to 0.0081 m/km. The severe gradient is used uniformly for one hour in the sun rise and the sun set periods.

The Nominal Ionospheric Gradient

The converted sigma value of the nominal vertical ionospheric gradient ($\sigma_{nominal/km}$) based on the equatorial radius and $k_{nominal}$ is 0.00062 m/km. The nominal gradient is used uniformly for the rest of the day in the availability analysis.

5.7.4 Single-Frequency User CAT III Availability Threat Illustration

A case description of the threat illustration is given below:

- Ionospheric gradient: the worst situation is assumed that the gradient is aligned with each satellite direction.
- Satellite availability: the first order approximation of the satellite availability is assumed, thus, only twenty four and twenty three satellites are considered (results in an optimistic outcome.)
- VPL calculation:
  - Noise model of the GPS signals considered herein is that the sigma value of the ground noise (multipath dominant) is 0.15 m while the sigma value of the airborne noise (multipath dominant) is 0.06 m for all elevation angles [Hsiao].
  - Referring to Eqn. 5.18, the DCSID baseline is obtained by assuming that the time constant of the CSC is 100 seconds and the airplane's approach velocity is 70m/s. Therefore, the lengthened baseline at the DH of 100 feet is about 15 km.

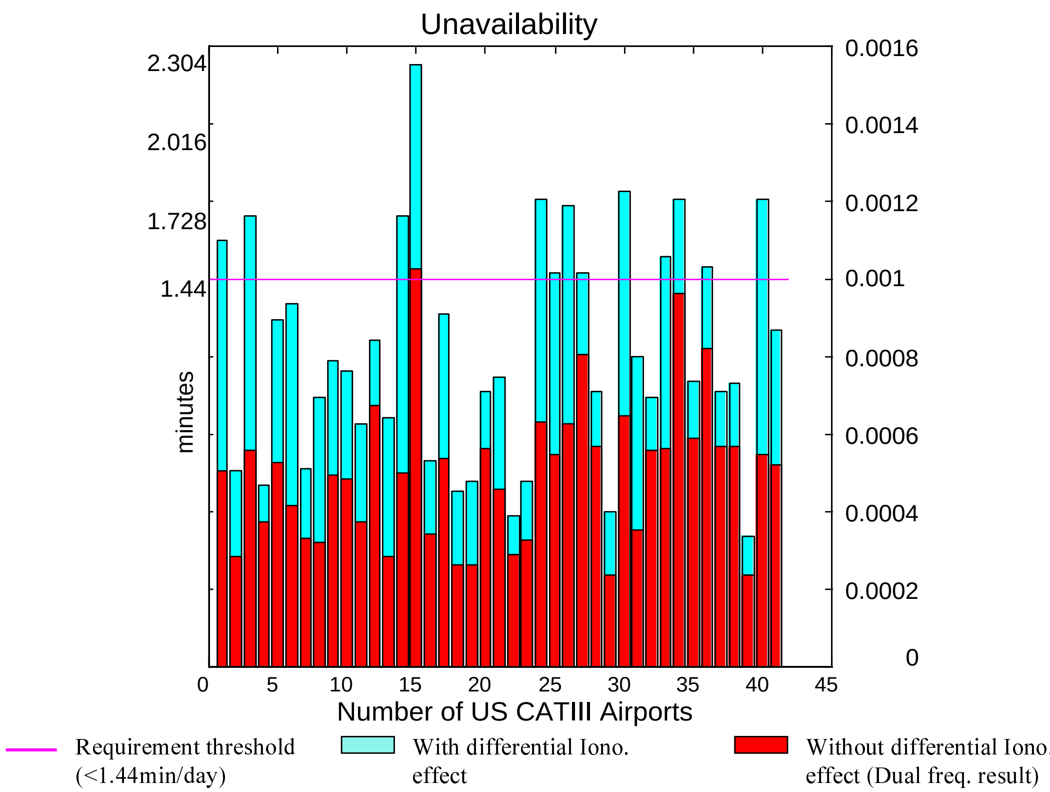

Figure 5.12: DCSID Impact on CAT III Availability.

– The sigma values of the lengthened baseline of the severe (σ_{severe}) and the nominal ($\sigma_{nominal}$) ionospheric gradient are 0.1215 m and 0.0093 m, respectively. The DCSID effect is obtained by multiplying the previous sigma values with the geometry factor of each satellite. Meanwhile, the profile of the DCSID is assumed to have the severe sigma for one hour in the morning and in the evening and the nominal sigma for the rest of the day.

Figure 5.12 summarizes how the DCSID affects the availability of 41 U.S. CAT III airports. Red bars denote the unavailability without considering the DCSID effect and will be the baseline for the following comparison. One airport exists which can not satisfy the CAT III availability based on the current almanac. This airport is excluded from the following comparison. Cyan bars represent the unavailability with the DCSID effect.

According to Fig. 5.12, twelve of the forty airports cannot fulfill the CAT III availability requirement, implying that these twelve airports lose their availability of the required VPL. Therefore, it is concluded that the DCSID effect must be considered.

5.8 Solutions, Benefits and Costs

This section discusses two solutions for the DCSID: solution 1 is dual frequency receiver, and solution 2 is single frequency ionosphere monitoring and correction. The benefits and costs of both solutions are discussed below.

5.8.1 Solution 1: Dual Frequency Receiver

An onboard dual frequency receiver can be used to physically measure the ionosphere, therefore, to the LAAS, the benefits and costs can be summarized as below.

Benefits

Without the ionosphere delay, a much longer carrier smoothing time constant can be used to smooth the multipath (the multipath free pseudorange technique). Therefore, accuracy can be improved, and it is even possible to monitor any potential multipath that slipped in from the Multipath Limiting Antenna (MLA).

Costs

The cost of this solution is the requirement that the L2 frequency be made available to civilian users or a third frequency (L5) be required. Additionally, a dual frequency receiver is more expensive than the single frequency receiver.

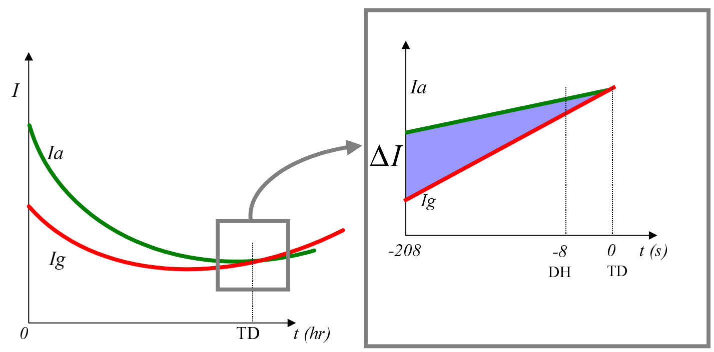

Figure 5.13: Illustration of the Single Frequency Ionosphere Monitoring and Correction.

5.8.2 Solution 2: Single Frequency Ionosphere Monitoring & Correction

For a single frequency user, the idea of the ionosphere monitoring and correction can be described as shown in Fig. 5.13 . The left hand portion of the figure illustrates the time history of the ionosphere delay of both the ground and the air. When the aircraft touches down, the ionosphere delay for both the ground and the air receivers are identical. Following the previous assumption that the ionosphere changes slowly within 15 minutes, then the ionosphere delay before touchdown (TD) can be examined closely, as shown in the right hand portion of the figure. The ionosphere delay in this time frame can be approximated as a linear function of time. The focus herein is on the differential ionosphere delay at the DH of 100 feet which is at -8 seconds. However, as a result of $2(\tau_{CSC} - T_s)$ time delay, say the τ_{CSC} is 100 seconds, the equivalent differential ionosphere delay is now at -206 seconds from TD. If the slope of the ionosphere of both the ground and air can be estimated, and if the ground's slope can be transmitted to the air, then the differential ionosphere delay at -206 seconds from TD can be estimated and corrected from the differential carrier smoothed pseudorange.

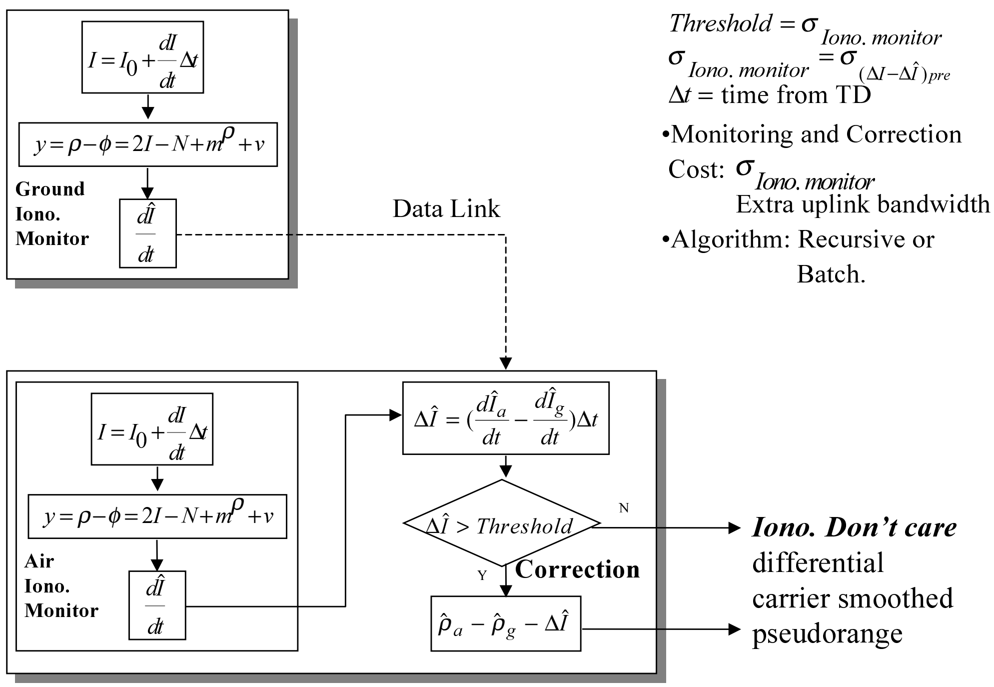

Figure 5.14: Conceptual Implementation of the Ionosphere Monitoring and Correction.

5.8.3 Single Frequency Ionosphere Monitoring & Correction: Conceptual Implementation

Figure 5.14 presents the block diagram of the conceptual implementation of the ionosphere monitoring and correction. Assuming a linear ionosphere model in the local area for both of the ground and the air, the single frequency ionosphere observables can be formed based on the code and carrier divergence and linear regression can be used to estimate the slopes of the ionosphere for both the ground and the air. Uplink the ground ionosphere slopes (multiple ground receivers) to the air. Then, the air forms the estimate of the differential ionosphere delay $\Delta\widehat{I}$. If the estimate of the differential ionosphere delay is greater than the predetermined threshold (estimation noise floor), then it is corrected from the differential carrier smoothed pseudorange.

The noise floor, $\sigma_{iono.\ monitor}$, is predetermined based on the ground and the air multipath observations. The determination process is discussed below.

Assuming the ionosphere delay with respect to the reference station within the time frame of 500 seconds can be approximated as

$$I = I_0 + \frac{dI}{dt}\Delta t \tag{5.31}$$

where $\Delta t = l\Delta T$ is the time to touchdown; ΔT is the sampling interval; and l is the epoch, its range is from -500 to -1.

The ionosphere observable can be expressed as

$$y_l = \rho_l - \phi_l = 2I_l - N + m_l^{\rho} + \nu_l. \tag{5.32}$$

Plugging Eqn. 5.31 into Eqn. 5.32, produces

$$y_l = (2I_0 - N) + \frac{dI}{dt}2l + \left(m_l^{\rho} + \nu_l\right). \tag{5.33}$$

Which can be simplified as

$$y_l = a + b2l + \left(m_l^{\rho} + \nu_l\right)$$

where $a = 2I_0 - N$ and $b = \frac{dI}{dt}$.

To estimate the ionospheric gradient b, either Least Squares (LS) or Kalman filtering can be used. For simplicity, the LS is used. The estimation error $\left(\tilde{a} \text{ and } \tilde{b}\right)$ can be determined by

$$\begin{bmatrix} \tilde{a} \\ \tilde{b} \end{bmatrix} = \left(H^* H\right)^{-1} H^* \left(\mathbf{m}^{\rho} + \nu\right) \tag{5.34}$$

where

$$
\begin{aligned}
H &= \begin{bmatrix} 1 & -2 \\ \vdots & \vdots \\ 1 & 2l \end{bmatrix}_{l=-1\cdots-300} \\
\mathbf{m}^{\rho} &= \begin{bmatrix} m^{\rho}_{-1} & \cdots & m^{\rho}_{-300} \end{bmatrix}^{*} \\
\nu &= \begin{bmatrix} \nu_{-1} & \cdots & \nu_{-300} \end{bmatrix}.
\end{aligned}
\tag{5.35}
$$

The error covariance can be expressed as:

$$
E\begin{bmatrix} \tilde{a} \\ \tilde{b} \end{bmatrix}\begin{bmatrix} \tilde{a} & \tilde{b} \end{bmatrix} = \left(H^{*}H\right)^{-1} H^{*}\left[E\left(\mathbf{m}^{\rho}\mathbf{m}^{\rho *}\right) + E\left(\nu\nu^{*}\right)\right] H\left(H^{*}H\right)^{-1}. \tag{5.36}
$$

For linear regression, the estimation error is dominated by the correlated noise rather than random noise, such as the receiver noise. In the following analysis, the multipath is considered the dominant source of error and is assumed to be a first order GMP with a time constant (τ_m) of 150 seconds. The driving noise is considered that $\sigma_{m,g}$ is 0.15m and $\sigma_{m,a}$ is 0.06 m, respectively. For a first order GMP,

$$
m_k = \alpha m_{k-1} + w_k,
$$

where $k = 1 \cdots K$, the covariance matrix can be expressed as

$$
E\left(\mathbf{m}^{\rho}\mathbf{m}^{\rho *}\right) = \begin{bmatrix} 1 & \alpha & \cdots & \alpha^{K-1} \\ \alpha & 1 & \ddots & \vdots \\ \vdots & \ddots & \ddots & \alpha \\ \alpha^{K-1} & \cdots & \alpha & 1 \end{bmatrix} \sigma_m^2. \tag{5.37}
$$

Based on the above assumptions the estimation error covariance of the $\frac{d\widehat{I_a}}{dt}$ and $\frac{d\widehat{I_g}}{dt}$ can be obtained as 0.0002354 and 0.0000942, respectively.

Referring to Fig. 5.14, the estimate of the differential ionosphere is

$$\Delta\widehat{I} = \left(\frac{d\widehat{I}_a}{dt} - \frac{d\widehat{I}_g}{dt}\right)\Delta t.$$

Therefore, the correction threshold for M reference stations can be determined as

$$\sigma_{\Delta I}^2 = \left(\frac{\sigma^2_{\frac{d\widehat{I}_a}{dt}}}{M-1} + \sigma^2_{\frac{d\widehat{I}_g}{dt}}\right)\Delta t^2.$$

At DH of 100 feet, for τ_{CSC} is 100 seconds, the estimation time (Δt) is -206 seconds from TD, and the threshold (error covariance) of the estimate of the differential ionosphere can be calculated as

$$\sigma_{iono.monitor} = \sigma_{\Delta I} = \sqrt{\frac{0.0485^2}{3-1} + 0.0194^2} = 0.0394m.$$

If the estimate of the differential ionosphere exceeds $\sigma_{iono.monitor}$, then it can be corrected from the differential carrier smoothed pseudorange for better positioning.

Figure 5.15 illustrates the ground ionosphere monitoring that validates the above assumption. The lower left plot shows the fitted ionosphere observable (darker line) for 500 seconds and validates that the linear model is adequate. The lower right plot shows the noise of the ionosphere observable that validates the assumption of τ_m and $\sigma_{m,g}$.

5.8.4 Single Frequency Ionosphere Monitoring & Correction: Benefit and Cost

Comparing $\sigma_{iono.monitor}$ with σ_{severe}, confirms that the ionosphere monitor can detect and correct the severe ionospheric gradient. However, the cost of monitoring and correction is to incorporate the estimation noise floor into the VPL calculation. Additionally, the bandwidth of the data link must be increased to broadcast the ground monitored ionosphere slope of each satellite from the ground. A rough estimate of

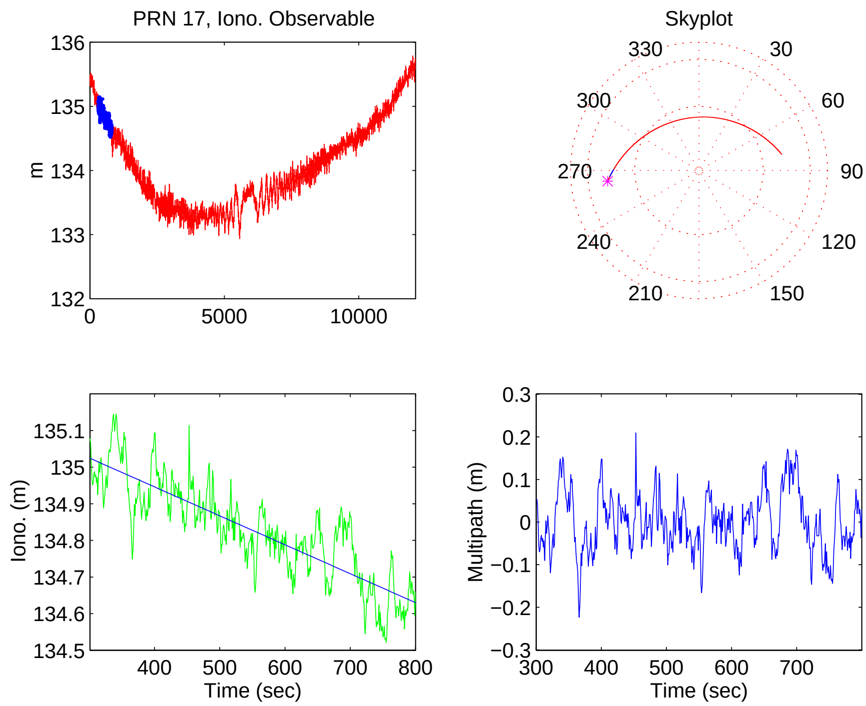

Figure 5.15: Illustration of the Ground Ionosphere Monitoring.

the increased bandwidth is 160 bits/sec for ten 16-bit ionospheric slopes.

To investigate the effect of the ionosphere monitoring and correction, the same availability calculation is applied but includes the ionosphere monitoring threshold. The results are presented as the green bars in Fig. 5.16 . Figure 5.16 indicates that the benefit of the ionosphere monitoring and correction is the reduction of unavailable airports from twelve to four which is significant. Additionally, the ionosphere monitoring and correction eliminates the divergence of the differential ionosphere delay and the multipath on the carrier smoothing time constant, thus allowing a longer carrier smoothing time constant for a better position.

The cost, in terms of performance, is that four out of forty airports continue to exceed the CAT III availability requirement. For these four airports, detailed examination of the ionosphere gradient should be considered instead of assuming the worst situation or using other means of geometry augmentation.

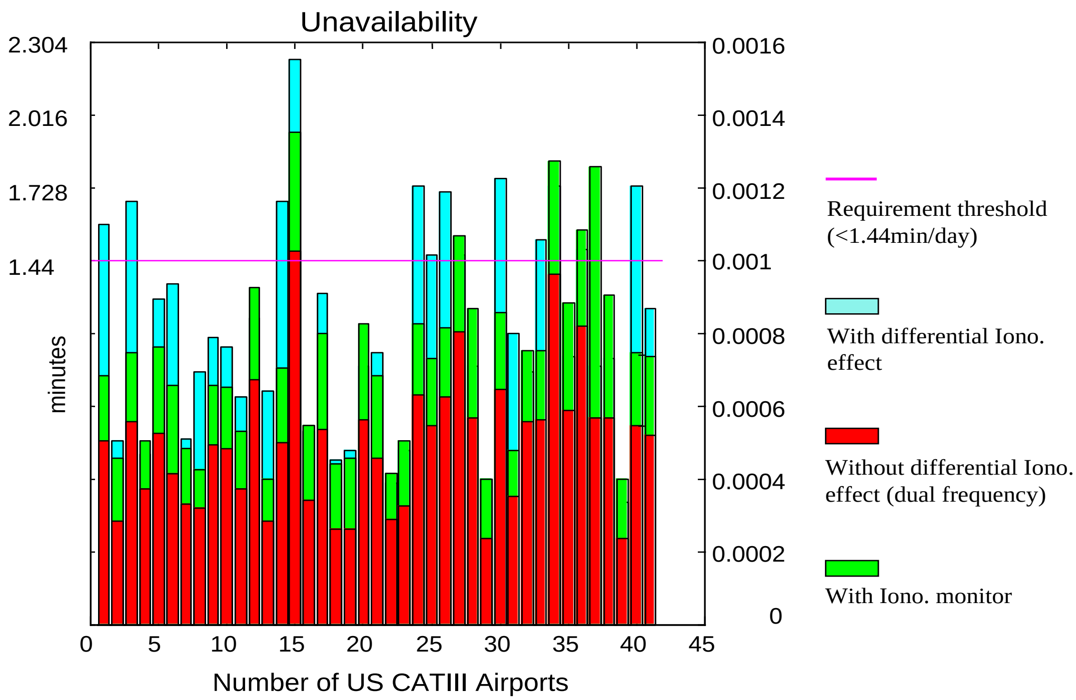

Figure 5.16: Benefits and Costs of the Ionosphere Monitoring and Correction.

5.9 Summary

This chapter first examines the effect of the differential carrier smoothed ionosphere delay on the CAT III availability of the LAAS. The threat illustration based on the carrier smoothing time constant of 100 seconds is given. The availability analysis results demonstrate that the DCSID is a key factor when a larger carrier smoothing time constant, say 200 to 400 seconds, is applied. Additionally, a tool for further detail availability analysis, Eqn. 5.18, is also derived and the influence of the CSC on the ionosphere delay is discussed.

Chapter 6

Conclusions

A goal of the FAA is to provide GPS-based navigation, precision approach and landing for civil aviation. Correspondingly, WAAS is being developed under the direction of the FAA to serve the enroute, terminal area, and CAT I precision approaches, while LAAS is being developed to serve low visibility precision approaches and landings (up to CAT III.) To ensure the dependability of the WAAS and LAAS, further augmentation systems, both GPS-dependent and GPS-independent, are under development.

The first part of this dissertation addresses a GPS-independent augmentation, namely an inertial backup, of the WAAS and the LAAS. Performance limits of the inertial augmentation are explored and a new Pseudolite/INS backup concept is developed. Meanwhile, the second part of this dissertation deals with the algorithm enhancement of the LAAS on the Differential Carrier Smoothed Ionosphere Delay (DCSID), thus enhancing the CAT III availability. An analytical tool and an algorithm for enhancing the CAT III availability of the LAAS due to the DCSID effect are also developed.

The contributions of this dissertation in these two areas can be summarized as follows:

Inertial Backup of DGPS-Based Precision Approach and Landing Systems

- WAAS/INS

For WAAS/INS integration, the integration provides continuity but insignificant improvement in accuracy. Due to the slow variation characteristic of the WAAS position error, the accuracy of the integrated system is shown to be dominated by the WAAS error. Therefore, potential for improving the accuracy of the integrated system to meet CAT II 95% accuracy requirements would exist only if the WAAS error was sufficient to satisfy the CAT II requirements.

- LAAS/INS

  The first accuracy comparison between LAAS carrier phase algorithms, the Code and Carrier Update (CCU) and the Carrier Phase Riding (CPR), has been provided. The accuracy of LAAS carrier phase algorithms was compared with the integrated LAAS/INS system. Results in Chapter 3 indicate that the LAAS carrier phase algorithms provide the same level of accuracy and differ only in their implementation structure. The derivation of the CPR provides insight into the similarities of the algorithm structure between the CPR and the LAAS/INS systems. For the LAAS/INS, with code and carrier phase updates to the integrated system, LAAS/INS performs comparably to the LAAS system using a carrier phase algorithm.

- PLs/INS

  An ultimate inertial backup, the 3-PLs/INS system, has been developed that can operate independently without data link, pseudolite synchronization or GPS. Based on the Total System Error (TSE) criterion, the 3-PLs/INS system using a navigation grade INS can meet the touchdown box requirement. The influence of the clock grade within the PLs and airborne receiver on landing performance has been examined. In terms of the touchdown box TSE, both the rubidium clock and quartz oscillator clock together with a navigation grade INS can provide the required touchdown performance. Performance differs when comparing the system performance of the 3-PLs/INS to the Navigation Sensor Error (NSE) requirements. However, NSE requirements are too stringent for the inertial system to fulfill. Therefore, NSE is not a major concern in accessing the performance. The 3-PLs/INS backup system is a new alternative backup concept developed in this research.

Differential Carrier Smoothed Ionosphere Effect on LAAS

An error source was discovered due to the CSC filtering of the ionosphere that had previously been considered negligible. This error could significantly influence the availability of a LAAS-based landing system. Therefore, the differential carrier smoothed ionosphere delay is not negligible and must be dealt with. The divergence on the carrier smoothing time constant of the differential ionosphere delay and multipath was also discovered herein. This discovery provided a new optimization factor when choosing the carrier smoothing time constant.

Furthermore, an analytical expression of the differential carrier smoothed ionosphere delay was derived. The analytical expression explains the internal structure of the DCSID and is an ideal tool for further analyzing the DCSID influence on the LAAS. The implications of this novel analytical expression include: 1) using different carrier smoothing time constants for the ground and the air degrades performance, and 2) using a larger carrier smoothing time constant for the airborne users degrades the LAAS performance. Both these insights are mentioned for the first time herein.

The DCSID effect on the CAT III availability of the LAAS has been characterized in a worst case scenario, demonstrating that the impact of the DCSID is significant. Therefore, a single frequency ionosphere monitoring and correction algorithm was developed herein to solve the DCSID effect on the LAAS. Simultaneously, the divergence on the carrier smoothing time constant of the differential ionosphere delay and the multipath has also been solved. Hence, larger carrier smoothing time constants can be used freely. However, the cost of applying the ionosphere monitoring and correction is the increased data link bandwidth for transmitting the ground ionosphere information, and also adding the estimation noise threshold to the VPL calculation for the availability analysis. Availability analysis results confirm that the benefits are significant.

Recommendations for Future Research

The following are suggestions for future research.

- Inertial backup

  In addition to demonstrating that the WAAS/INS, and the LAAS/INS provide comparable accuracy to the WAAS and the LAAS, this dissertation has shown that the inertial backup improves continuity. However, the integrity of the integrated system when the GPS part is incomplete remains unaddressed. Therefore, a trade-off between redundancy and the cost necessary to fulfill the integrity requirement requires further study to make the inertial backup feasible.

- DCSID

  With its increasingly global acceptance, LAAS must serve more airports that are located in either the sub-aurora area or the equatorial region, where the ionosphere is more active and the ionospheric gradient is more severe. Therefore, the assumption made in Chapter 5 that the ionosphere is static during the final approach may need to be reconsidered. The optimization of the ionosphere monitoring model and the estimation algorithm require further study to make the ionosphere monitoring and correction algorithm suitable for each individual airport.

Appendix A

Introduction to the Inertial Navigation System

A.1 Introduction

Inertial Navigation System (INS) senses the motion of a vehicle and provides the position and the attitude of this vehicle with respect to a proper coordinate frame. It comprises two parts: an inertial measurement unit (IMU) and a computer unit (CU). IMU includes inertial sensors, i.e. accelerometers and gyros, and electronics. IMU measures accelerations and angular rates of the vehicle it is carried in and then digitalis these measurements. CU uses the measured accelerations and angular rates to compute three-dimensional position and velocity of the vehicle.

The following briefly describes some important concepts of the INS.

- Simple thought: INS is simply a series of integration processes.

  Figure A.1 is a simplified system which provides the basic concept of the INS. Figure A.1 depicts that if the acceleration a and the angular rate ω are available and the initial condition of the velocity, position and the attitude are known, then position and attitude can be gained by simple integration. However, actual systems are more complicated than Fig. A.1 displays and are described later.

- Coordinate systems:

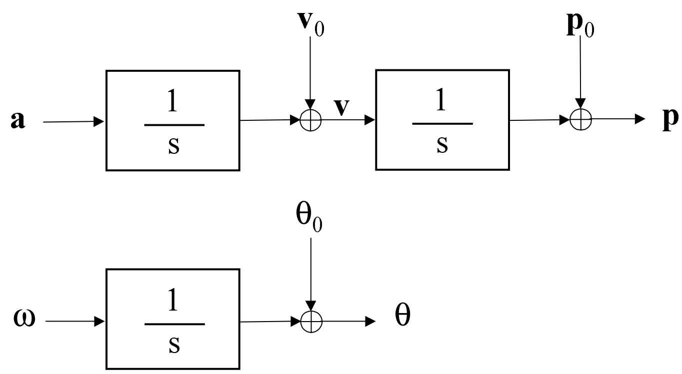

Figure A.1: Simplified INS Block Diagram

To locate and orient a vehicle, a common coordinate system must be specified as a reference. Several conventionally used coordinate systems in the INS application include:

– the Flat Earth frame for the car navigation,

– the Tangent Plane frame for missile guidance,

– the Earth-Centered Earth-fixed (ECEF) frame, (use e for abbreviation), for satellite navigation and

– the Local-level (LL) frame (use l for abbreviation) usually use East-North-UP (ENU) or North-East-Down(NED), for transcontinental flight.

When the INS is coordinatized, it is called a "mechanization."

Other important coordinate frames include the inertial frame (use i for abbreviation) and the body frame (use b for abbreviation), where inertial sensors are mounted.

- Gimbal versus strapdown:

Gimbal type INS places its inertial sensors on a platform. Gimbal's platform is always leveled with respect to the LL frame by torquing gimbals. Strapdown type INS, fixes its platform to the body of the vehicle, and a numerical gimbal is required to transform the body fixed measurements to local-level referenced measurements for further processing.

- Gravity model:

$$\mathbf{f} = \mathbf{a} - \mathbf{G} \tag{A.1}$$

Equation A.1 lists the measurement equation of an accelerometer, where $\mathbf{f}$, the specific force, is the output of an accelerometer. The specific force is the total force acting on the proof mass of the accelerometer, thus, it contains the acceleration $\mathbf{a}$ due to the motion of its carrying vehicle and the gravitation $\mathbf{G}$ due to the gravitational field. To calculate the acceleration $\mathbf{a}$, a gravitation model is needed to account for $\mathbf{G}$.

The next section defines the gravity model, a combination of the gravitation model and the centripetal force due to the earth rotation, which is location dependent. Therefore, the gravity model varies with different mechanizations.

A.2 Derivation of the ECEF Mechanization

Definition:

$$
\begin{aligned}
\mathbf{r} &= \text{a position vector in space} \\
\overset{e}{\mathbf{r}} &= \text{time derivative of } \mathbf{r} \text{ with respect to } e \text{ frame} \\
\omega_{ab}^{c} &= \text{angular velocity vector of the } b \text{ frame with respect to the } a \text{ frame} \\
&\qquad \text{and coordinatized in the } c \text{ frame} \\
\mathbf{C}_{a}^{b} &= \text{coordinate transformation matrix from } a \text{ frame to } b \text{ frame} \\
\omega_{ib}^{b} &= \text{angular velocity measured by the strapdown } (b \text{ frame) gyro} \\
&= \omega_{ie}^{b} + \omega_{eb}^{b} \\
\mathbf{f}^{b} &= \text{specific force measured by the strapdown } (b \text{ frame) accelerometer}
\end{aligned}
$$

Translational equation:

$$
\begin{aligned}
\dot{\mathbf{r}} &= \overset{e}{\mathbf{r}} + \omega_{ie} \times \mathbf{r} && \text{(A.2)} \\
\dot{\mathbf{v}} &= \overset{ee}{\mathbf{r}} + 2\omega_{ie} \times \overset{e}{\mathbf{r}} + \omega_{ie} \times \omega_{ie} \times \mathbf{r} && \text{(A.3)}
\end{aligned}
$$

Combine Eqn. A.3 with Eqn. A.1, we obtain

$$
\overset{ee}{\mathbf{r}} = \mathbf{f} - 2\omega_{ie} \times \overset{e}{\mathbf{r}} + \mathbf{G} - \omega_{ie} \times \omega_{ie} \times \mathbf{r}. \tag{A.4}
$$

Define gravity $\mathbf{g}$

$$
\mathbf{g} = \mathbf{G} - \omega_{ie} \times \omega_{ie} \times \mathbf{r}. \tag{A.5}
$$

Combining Eqn. A.4 and Eqn. A.5, we obtain

$$
\overset{ee}{\mathbf{r}} = \mathbf{f} - 2\omega_{ie} \times \overset{e}{\mathbf{r}} + \mathbf{g}.
$$

Coordinatize in the ECEF frame (e), we obtain

$$\overset{eee}{\mathbf{r}} = \mathbf{f}^e - 2\omega_{ie}^e \times \overset{ee}{\mathbf{r}} + \mathbf{g}^{\mathbf{e}}. \tag{A.6}$$

For strapdown INS, the specific force measurement is in the body frame (b). The specific force in the e frame can be obtained by coordinate transformation. Define $\mathbf{C}_b^e$ is the coordinate transformation matrix from the b frame to the e frame. Then,

$$\mathbf{f}^e = \mathbf{C}_b^e \mathbf{f}^b. \tag{A.7}$$

Substituting Eqn. A.7 into Eqn. A.6, we obtain the ECEF mechanization of the translational equation

$$\ddot{\mathbf{r}}^e = \mathbf{C}_b^e \mathbf{f}^b - 2\omega_{ie}^e \times \dot{\mathbf{r}}^e + \mathbf{g}^e. \tag{A.8}$$

Rotational equation:

$$\begin{aligned}
\dot{\mathbf{C}}_b^e &= \lim_{\Delta t \to 0} \frac{\mathbf{C}_b^e(t+\Delta t) - \mathbf{C}_b^e(t)}{\Delta t} \\
\mathbf{C}_b^e(t+\Delta t) &= \mathbf{C}_b^e(t)\left(\mathbf{I} + \Delta\theta^b \times\right) \\
\dot{\mathbf{C}}_b^e &= \lim_{\Delta t \to 0} \mathbf{C}_b^e(t) \frac{\Delta\theta^b \times}{\Delta t} && \text{(A.9)} \\
&= \mathbf{C}_b^e(t)\,\omega_{eb}^b \times && \text{(A.10)}
\end{aligned}$$

Since $\omega_{eb}^b = \omega_{ib}^b - \omega_{ie}^b = \omega_{ib}^b - \mathbf{C}_e^b \omega_{ie}^e$, therefore Eqn. A.10 can be rewritten as

$$\dot{\mathbf{C}}_b^e = \mathbf{C}_b^e \omega_{ib}^b \times - \omega_{ie}^e \times . \tag{A.11}$$

Rewriting Eqns. A.8 and A.11, the ECEF mechanization governing equation is obtained

$$\begin{bmatrix} \dot{\mathbf{r}}^e \\ \dot{\mathbf{v}}^e \\ \dot{\mathbf{C}}_b^e \end{bmatrix} = \begin{bmatrix} \mathbf{v}^e \\ \mathbf{C}_b^e \mathbf{f}^b - 2\omega_{ie}^e \times \dot{\mathbf{r}}^e + \mathbf{g}^e \\ \mathbf{C}_b^e \omega_{ib}^b \times - \omega_{ie}^e \times \end{bmatrix}. \tag{A.12}$$

A.3 IMU Sensor Error Models

For navigation grade INS, laser gyros and pendulous accelerometers are usually used. The following are the general models for these sensors [Savage], [Stieler].

A.3.1 Model of the Laser Gyro

$$w_{output} = (1+\epsilon)(w_x + \alpha_z w_y - \alpha_y w_z) + w_d \tag{A.13}$$

$$\epsilon = K + K_1 \frac{w_x}{|w_x|} \tag{A.14}$$

$$w_d = d_0 + d_t + n^g \tag{A.15}$$

$$\dot{d}_t = \frac{-1}{\tau_d} d_t + \frac{1}{\tau_d} w^d \tag{A.16}$$

where α_z, α_y, K, K_1 and d_0 are random constants; d_t is a first order Gauss-Markov Process (GMP), and n^g and w^d are random variables. The expected values of the above random constants and the power spectrum density of the above random variables are listed below.

$$E(KK^*) = \sigma_K^2, \quad E(K_1 K_1^*) = \sigma_{K_1}^2 \tag{A.17}$$

$$E(\alpha_z \alpha_z^*) = \sigma_{\alpha_z}^2, \quad E(\alpha_y \alpha_y^*) = \sigma_{\alpha_y}^2 \tag{A.18}$$

$$E(nn^*) = Q\delta(t), \; E(w^d w^{d*}) = 2\tau_d \sigma_{d_t}^2 \tag{A.19}$$

These parameters are defined as follows.

$$
\begin{aligned}
w_{output} &= \text{gyro output rate} \\
\epsilon &= \text{gyro scale-factor error} \\
w_x, w_y, w_z &= \text{angular rate in the input } (x)\text{, axes normal to the input axis} \\
& (y,\ z) \text{ axis respectively} \\
\alpha_z,\ \alpha_y &= \text{misalignments of the gyro plane relative to the nominal gyro} \\
& \text{input axis} \\
K &= \text{fixed scale-factor error} \\
K_1 &= \text{asymmetry of scale-factor error} \\
d_0 &= \text{fixed gyro drift error} \\
d_t &= \text{gyro drift stability, usually is modeled as a first order GMP} \\
n^g &= \text{measurement noise (white)} \\
w_d &= \text{driving noise of the gyro drift stability}
\end{aligned}
$$

Therefore, the error model for the laser gyro is obtained as below.

$$\delta w_{output} = \left(K + K_1 \frac{w_x}{|w_x|}\right) w_x + \alpha_z w_y - \alpha_y w_z + d_0 + d_t + n^g \tag{A.20}$$

A.3.2 Model of the Pendulous Type Accelerometer

$$
\begin{aligned}
f_{output} &= (1+\epsilon)\left(a_I + \alpha_P a_H - \alpha_H a_P\right) + a_b && \text{(A.21)} \\
\epsilon &= K + K_1 \frac{a_I}{|a_I|} + K_2 a_I + K_3 a_I^2 && \text{(A.22)} \\
a_b &= b_0 + b_t + c a_I a_P + n^a && \text{(A.23)} \\
\dot{b_t} &= \frac{-1}{\tau_b} b_t + \frac{1}{\tau_b} w^b && \text{(A.24)}
\end{aligned}
$$

where $\alpha_P,\ \alpha_H,\ K,\ K_1,\ K_2,\ K_3,\ b_0$ and c are random constants; b_t represents a first order Gauss-Markov Process (GMP); n^a and w^b are random variables. The expected values of the above random constants and the power spectrum density of the above random variables are listed below.

$$E\left(KK^*\right) = \sigma_K^2, \quad E\left(K_iK_i^*\right) = \sigma_{K_i}^2,\ i = 1,2,3 \tag{A.25}$$

$$E\left(\alpha_P\alpha_P^*\right) = \sigma_{\alpha_{Pz}}^2, \quad E\left(\alpha_H\alpha_H^*\right) = \sigma_{\alpha_H}^2 \tag{A.26}$$

$$E\left(b_0b_0^*\right) = \sigma_{b_0}^2, \quad E\left(cc^*\right) = \sigma_c^2 \tag{A.27}$$

$$E\left(n^an^{a*}\right) = Q^a\delta\left(t\right),\ E\left(w^bw^{b*}\right) = 2\tau_b\sigma_{b_t}^2 \tag{A.28}$$

These parameters are defined as follows.

f_{output} = accelerometer output

ϵ = scale-factor error

a_I, a_H, a_P = specific force along the input (I), hinge (H) and pendulum (P) axis respectively

α_z, α_y = misalignments of the accelerometer

K = fixed scale-factor error

K_1 = asymmetry of scale-factor error

K_2, K_3 = higher order asymmetry of scale-factor error

b_0 = fixed accelerometer bias error

b_t = accelerometer bias stability, usually is modeled as a first order GMP

n^a = measurement noise (white)

w_b = driving noise of the accelerometer bias stability

Therefore, the error model for the pendulous accelerometer is obtained as follows.

$$\delta f_{output} = \left(K + K_1\frac{w_x}{|w_x|} + K_2a_I + K_3a_I^2\right)a_I + \alpha_Pa_H - \alpha_Ha_P + b_0 + b_t + n^a \tag{A.29}$$

A.4 INS Error Equation of the ECEF Mechanization

The INS error equation can be obtained by using the small perturbation method summarized below.

1. Perturbing Eqn. A.12-1, obtains

$$\dot{\mathbf{r}}^e + \delta\dot{\mathbf{r}}^e = \mathbf{v}^e + \delta\mathbf{v}^e.$$

Eliminating the nominal terms, we obtain

$$\delta\dot{\mathbf{r}}^e = \delta\mathbf{v}^e. \tag{A.30}$$

2. Perturbing A.12-2 obtains

$$\dot{\mathbf{v}}^e + \delta\dot{\mathbf{v}}^e = \left(\mathbf{C}_b^e + \delta\mathbf{C}_b^e\right)\left(\mathbf{f}^b + \delta\mathbf{f}^b\right) - 2\omega_{ie}^e \times \left(\dot{\mathbf{r}}^e + \delta\dot{\mathbf{r}}^e\right) + \left(\mathbf{g}^e + \delta\mathbf{g}^e\right).$$

Rearranging and neglecting the second order terms, yield

$$\delta\dot{\mathbf{v}}^e = \mathbf{C}_b^e\delta\mathbf{f}^b + \delta\mathbf{C}_b^e\mathbf{f}^b - 2\omega_{ie}^e \times \delta\dot{\mathbf{r}}^e + \delta\mathbf{g}^e. \tag{A.31}$$

where

(a) $\delta\mathbf{f}^b$ represents the error in the measurement of the specific force in the b frame;

(b) $\delta\mathbf{C}_b^e = \varepsilon \times \mathbf{C}_b^e$, since $\left(\mathbf{I} + \varepsilon\times\right)\mathbf{C}_b^e = \mathbf{C}_b^e + \delta\mathbf{C}_b^e$. $\varepsilon = [\varepsilon_x\ \varepsilon_y\ \varepsilon_z]^* =$ the misalignment angle between the computed frame and the truth frame. Therefore,

$$\delta\mathbf{C}_b^e\mathbf{f}^b = \varepsilon \times \mathbf{f}^e = -\mathbf{f}^e\times\varepsilon; \tag{A.32}$$

(c) gravity perturbation can be derived as below.

$$\delta \mathbf{g}^e = \frac{\partial \mathbf{g}^e}{\partial \mathbf{r}^e}\delta \mathbf{r}^e = \mathbf{N}\delta \mathbf{r}^e \tag{A.33}$$

where $\mathbf{N}$ is the Jacobian matrix of the gravity.

Plugging Eqns. A.32 and A.33 into Eqn. A.31, obtains

$$\delta \dot{\mathbf{v}}^e = \mathbf{C}_b^e \delta \mathbf{f}^b - \mathbf{f}^e \times \varepsilon - 2\omega_{ie}^e \times \delta \mathbf{v}^e + \mathbf{N}\delta \mathbf{r}^e. \tag{A.34}$$

3. Perturbing A.12-3 yields

$$[(\mathbf{I} + \varepsilon \times) \mathbf{C}_b^e]^{\cdot} = (\mathbf{I} + \varepsilon \times) \mathbf{C}_b^e \left(\omega_{ib}^b \times + \delta\omega_{ib}^b \times\right) - \ \omega_{ie}^e \times .$$

By expending and canceling the nominal and the second order terms, we can produce

$$\dot{\varepsilon} \times \mathbf{C}_b^e + \varepsilon \times \dot{\mathbf{C}}_b^e = \mathbf{C}_b^e \delta\omega_{ib}^b \times + \varepsilon \times \mathbf{C}_b^e \omega_{ib}^b \times .$$

Plugging Eqn. A.12-3 into the above equation and canceling out the common terms lead to

$$\dot{\varepsilon} \times \mathbf{C}_b^e = \mathbf{C}_b^e \delta\omega_{ib}^b \times - \omega_{ie}^e \times \varepsilon \times .$$

Rearranging the above equation, the error equation of the rotational equation in terms of the misalignment is obtained as

$$\dot{\varepsilon} = \mathbf{C}_b^e \delta\omega_{ib}^b - \omega_{ie}^e \times \varepsilon. \tag{A.35}$$

4. Reorganizing Eqns. A.30, A.34 and A.35 in terms of the navigation error states,

the error equation of the ECEF mechanization is obtained as follows

$$\begin{bmatrix} \dot{\varepsilon} \\ \delta\dot{\mathbf{r}}^e \\ \delta\dot{\mathbf{v}}^e \end{bmatrix} = \begin{bmatrix} -\omega_{ie}^e\times & \mathbf{0} & \mathbf{0} \\ \mathbf{0} & \mathbf{0} & \mathbf{I} \\ -\mathbf{f}^e & \mathbf{N} & -2\omega_{ie}^e\times \end{bmatrix} \begin{bmatrix} \varepsilon \\ \delta\mathbf{r}^e \\ \delta\mathbf{v}^e \end{bmatrix} + \begin{bmatrix} \mathbf{C}_b^e & \mathbf{0} \\ \mathbf{0} & \mathbf{C}_b^e \\ \mathbf{0} & \mathbf{0} \end{bmatrix} \begin{bmatrix} \delta\omega_{ib}^b \\ \delta\mathbf{f}^b \end{bmatrix}. \tag{A.36}$$

When considering the sensor error states, as referred to in Eqns. A.20 and A.29, the considered sensor error states can be augmented into the state equation for further parameter estimation.

Reference: [Wei]

Appendix B

Sensitivity Analysis

Given a truth model (subscript t)

$$\mathbf{x}_{t,k+1} = \mathbf{F}_{t,k}\mathbf{x}_{t,k} + \mathbf{G}_{t,k}\mathbf{w}_{t,k} \tag{B.1}$$

$$\mathbf{y}_{t,k} = \mathbf{H}_{t,k}\mathbf{x}_{t,k} + \mathbf{v}_{t,k} \tag{B.2}$$

$$\mathbf{z}_{t,k} = \mathbf{C}_{t,k}\mathbf{x}_{t,k} \tag{B.3}$$

where subscript k represents the k^{th} time epoch, $\mathbf{y}_{t,k}$ is the measurement and $\mathbf{z}_{t,k}$ is the output parameter, which is a linear combination of the state.

The initial covariance ($\mathbf{P}_{t,0}$), process noise ($\mathbf{Q}_t$) and measurement noise ($\mathbf{R}_t$) is defined below.

$$\mathbf{P}_{t,0} = E\left(\mathbf{x}_{t,0}\mathbf{x}_{t,0}^*\right) \tag{B.4}$$

$$\mathbf{Q}_t = E\left(\mathbf{w}_t\mathbf{w}_t^*\right) \tag{B.5}$$

$$\mathbf{R}_t = E\left(\mathbf{v}_t\mathbf{v}_t^*\right) \tag{B.6}$$

Select a filter model (subscript f)

$$\mathbf{x}_{f,k+1} = \mathbf{F}_{f,k}\mathbf{x}_{f,k} + \mathbf{G}_{f,k}\mathbf{w}_{f,k} \tag{B.7}$$

$$\mathbf{y}_{f,k} = \mathbf{H}_{f,k}\mathbf{x}_{f,k} + \mathbf{v}_{f,k} \tag{B.8}$$

$$\mathbf{z}_{f,k} = \mathbf{C}_{f,k}\mathbf{x}_{f,k} \tag{B.9}$$

where $\mathbf{y}_{f,k}$ is the measurement and $\mathbf{z}_{f,k}$ is the output parameter which is a linear combination of the state.

The initial covariance ($\mathbf{P}_{f,0}$), process noise ($\mathbf{Q}_f$) and measurement noise ($\mathbf{R}_f$) is defined below.

$$\begin{aligned} \mathbf{P}_{f,0} &= E\left(\mathbf{x}_{f,0}\mathbf{x}_{f,0}^*\right) && \text{(B.10)} \\ \mathbf{Q}_f &= E\left(\mathbf{w}_f\mathbf{w}_f^*\right) && \text{(B.11)} \\ \mathbf{R}_f &= E\left(\mathbf{v}_f\mathbf{v}_f^*\right) && \text{(B.12)} \end{aligned}$$

Based on the above filter model, a Kalman filter with a Kalman gain $\mathbf{K}_f$ can be designed, providing the best estimate of the filter state, $\widehat{\mathbf{x}}_f$. Meanwhile, the estimate of the filter state can be expressed as

$$\begin{aligned} \widehat{\mathbf{x}}_{f,k}^+ &= \widehat{\mathbf{x}}_{f,k}^- + \mathbf{K}_{f,k}\left(\mathbf{y}_{t,k} - \mathbf{H}_{f,k}\widehat{\mathbf{x}}_{f,k}^-\right) && \text{(B.13)} \\ &= \left(\mathbf{I} - \mathbf{K}_{f,k}\mathbf{H}_{f,k}\right)\widehat{\mathbf{x}}_{f,k}^- + \mathbf{K}_{f,k}\mathbf{H}_{t,k}\mathbf{x}_{t,k} + \mathbf{K}_{f,k}\mathbf{v}_{t,k} && \text{(B.14)} \end{aligned}$$

The above equation uses the real world measurement $\mathbf{y}_{t,k}$ to update the estimate of the filter state.

To calculate the actual estimation error of the output parameters ($\widetilde{\mathbf{z}}_k$), the difference between the output parameter ($\mathbf{z}_{t,k}$) of the truth model and the best estimate of the output parameter ($\widehat{\mathbf{z}}_{f,k}$) of the filter model can be calculated, as below.

$$\begin{aligned} \widetilde{\mathbf{z}}_k &= \mathbf{z}_{t,k} - \widehat{\mathbf{z}}_{f,k} && \text{(B.15)} \\ &= \mathbf{C}_{t,k}\mathbf{x}_{t,k} - \mathbf{C}_{f,k}\widehat{\mathbf{x}}_{f,k}^+ && \text{(B.16)} \end{aligned}$$

The covariance of $\widehat{\mathbf{z}}_{f,k}$ then can be calculated as

$$\begin{aligned} E\left(\widetilde{\mathbf{z}}_k\widetilde{\mathbf{z}}_k^*\right) &= \mathbf{C}_{t,k}E\left(\mathbf{x}_{t,k}\mathbf{x}_{t,k}^*\right)\mathbf{C}_{t,k}^* - \mathbf{C}_{f,k}E\left(\widehat{\mathbf{x}}_{f,k}^+\mathbf{x}_{t,k}^*\right)\mathbf{C}_{t,k}^* \\ &\quad -\mathbf{C}_{t,k}E\left(\mathbf{x}_{t,k}\widehat{\mathbf{x}}_{f,k}^{+*}\right)\mathbf{C}_{f,k}^* + \mathbf{C}_{f,k}E\left(\widehat{\mathbf{x}}_{f,k}^+\widehat{\mathbf{x}}_{f,k}^{+*}\right)\mathbf{C}_{f,k}^*. && \text{(B.17)} \end{aligned}$$

Define

$$\begin{aligned}
\mathbf{R}_{tt,k} &= E\left(\mathbf{x}_{t,k}\mathbf{x}_{t,k}^{*}\right) &\text{(B.18)}\\
\mathbf{R}_{te,k}^{+} &= E\left(\mathbf{x}_{t,k}\widehat{\mathbf{x}}_{f,k}^{+*}\right) &\text{(B.19)}\\
\mathbf{R}_{ee,k}^{+} &= E\left(\widehat{\mathbf{x}}_{f,k}^{+}\widehat{\mathbf{x}}_{f,k}^{+*}\right) &\text{(B.20)}
\end{aligned}$$

Eqn. B.17 can be rewritten as

$$E\left(\widetilde{\mathbf{z}}_{k}\widetilde{\mathbf{z}}_{k}^{*}\right) = \mathbf{C}_{t,k}\mathbf{R}_{tt,k}\mathbf{C}_{t,k}^{*} - \mathbf{C}_{f,k}\mathbf{R}_{te,k}^{+*}\mathbf{C}_{t,k}^{*} - \mathbf{C}_{t,k}\mathbf{R}_{te,k}^{+}\mathbf{C}_{f,k}^{*} + \mathbf{C}_{f,k}\mathbf{R}_{ee,k}^{+}\mathbf{C}_{f,k}^{*}. \quad \text{(B.21)}$$

Equations for calculating $\mathbf{R}_{tt,k}$, $\mathbf{R}_{te,k}^{+}$ and $\mathbf{R}_{ee,k}^{+}$ are derived as follows.

- $\mathbf{R}_{tt,k}$: plugging Eqn. B.1 into Eqn. B.18 we can obtain,

$$\mathbf{R}_{tt,k+1} = \mathbf{F}_{t,k}\mathbf{R}_{tt,k}\mathbf{F}_{t,k}^{*} + \mathbf{G}_{t,k}\mathbf{Q}_{t,k}\mathbf{G}_{t,k}^{*} \quad \text{(B.22)}$$

- $\mathbf{R}_{te,k}^{+}$: plugging Eqn. B.14 into Eqn. B.19 we can obtain,

$$\begin{aligned}
\mathbf{R}_{te,k}^{+} &= E\left(\mathbf{x}_{t,k}\widehat{\mathbf{x}}_{f,k}^{+*}\right)\\
&= E\left[\mathbf{x}_{t,k}\widehat{\mathbf{x}}_{f,k}^{-*}\left(\mathbf{I}-\mathbf{K}_{f,k}\mathbf{H}_{f,k}\right)^{*} + \mathbf{x}_{t,k}\mathbf{x}_{t,k}^{*}\left(\mathbf{K}_{f,k}\mathbf{H}_{t,k}\right)^{*}\right]\\
&= \mathbf{R}_{te,k}^{-}\left(\mathbf{I}-\mathbf{K}_{f,k}\mathbf{H}_{f,k}\right)^{*} + \mathbf{R}_{tt,k}\left(\mathbf{K}_{f,k}\mathbf{H}_{t,k}\right)^{*} \qquad \text{(B.23)}
\end{aligned}$$

- $\mathbf{R}_{ee,k}^{+}$: plugging Eqn. B.14 into Eqn. B.20 we can obtain,

$$
\begin{aligned}
\mathbf{R}^{+}_{ee,k} &= E\left(\widehat{\mathbf{x}}^{+}_{f,k}\widehat{\mathbf{x}}^{+*}_{f,k}\right) \\
&= E\begin{bmatrix}
\left(\mathbf{I}-\mathbf{K}_{f,k}\mathbf{H}_{f,k}\right)\widehat{\mathbf{x}}^{-}_{f,k}\widehat{\mathbf{x}}^{-*}_{f,k}\left(\mathbf{I}-\mathbf{K}_{f,k}\mathbf{H}_{f,k}\right)^{*} \\
+\left(\mathbf{K}_{f,k}\mathbf{H}_{t,k}\right)\mathbf{x}_{t,k}\mathbf{x}^{*}_{t,k}\left(\mathbf{K}_{f,k}\mathbf{H}_{t,k}\right)^{*} \\
+\left(\mathbf{I}-\mathbf{K}_{f,k}\mathbf{H}_{f,k}\right)\widehat{\mathbf{x}}^{-}_{f,k}\mathbf{x}^{*}_{t,k}\left(\mathbf{K}_{f,k}\mathbf{H}_{t,k}\right)^{*} \\
+\left(\mathbf{K}_{f,k}\mathbf{H}_{t,k}\right)\mathbf{x}_{t,k}\widehat{\mathbf{x}}^{-*}_{f,k}\left(\mathbf{I}-\mathbf{K}_{f,k}\mathbf{H}_{f,k}\right)^{*} \\
+\mathbf{K}_{f,k}\mathbf{v}_{t,k}\mathbf{v}^{*}_{t,k}\mathbf{K}^{*}_{f,k}
\end{bmatrix} \\
\mathbf{R}^{+}_{ee,k} &= \left(\mathbf{I}-\mathbf{K}_{f,k}\mathbf{H}_{f,k}\right)\mathbf{R}^{-}_{ee,k}\left(\mathbf{I}-\mathbf{K}_{f,k}\mathbf{H}_{f,k}\right)^{*}+\mathbf{K}_{f,k}\mathbf{H}_{t,k}\mathbf{R}_{tt,k}\left(\mathbf{K}_{f,k}\mathbf{H}_{t,k}\right)^{*} \\
&\quad+\left(\mathbf{I}-\mathbf{K}_{f,k}\mathbf{H}_{f,k}\right)\mathbf{R}^{-}_{et,k}\left(\mathbf{K}_{f,k}\mathbf{H}_{t,k}\right)^{*} \\
&\quad+\mathbf{K}_{f,k}\mathbf{H}_{t,k}\mathbf{x}_{t,k}\widehat{\mathbf{x}}^{-*}_{f,k}\left(\mathbf{I}-\mathbf{K}_{f,k}\mathbf{H}_{f,k}\right)^{*}+\mathbf{K}_{f,k}\mathbf{R}_{t,k}\mathbf{K}^{*}_{f,k} \qquad \text{(B.24)}
\end{aligned}
$$

Initial conditions for the above three covariances are:

$$\mathbf{R}_{tt,0} = \mathbf{P}_{t,0} \qquad \text{(B.25)}$$

$$\mathbf{R}_{te,0} = \mathbf{0} \qquad \text{(B.26)}$$

$$\mathbf{R}_{ee,0} = \mathbf{0} \qquad \text{(B.27)}$$

The propagation of $\mathbf{R}^{-}_{te,k}$ and $\mathbf{R}^{-}_{ee,k}$ is given below.

- $\mathbf{R}^{-}_{te,k}$

  Define:

$$\mathbf{R}^{-}_{te,k+1} = E\left(\mathbf{x}_{t,k+1}\widehat{\mathbf{x}}^{-*}_{f,k+1}\right) \qquad \text{(B.28)}$$

  where, according to Eq.B.7,

$$\widehat{\mathbf{x}}^{-}_{f,k+1} = \mathbf{F}_{f,k}\hat{\mathbf{x}}^{+}_{f,k}. \qquad \text{(B.29)}$$

  Plugging Eqns. B.1 and B.29 into Eqn. B.28 obtains

$$\mathbf{R}^{-}_{te,k+1} = \mathbf{F}_{t,k}E\left(\mathbf{x}_{t,k}\hat{\mathbf{x}}^{+*}_{f,k}\right)\mathbf{F}^{*}_{f,k}+\mathbf{G}_{t,k}E\left(\mathbf{w}_{t,k}\hat{\mathbf{x}}^{+*}_{f,k}\right)\mathbf{F}^{*}_{f,k}. \qquad \text{(B.30)}$$

Since $\mathbf{w}_{t,k}$ and $\hat{\mathbf{x}}_{f,k}^{+*}$ are independent, $E\left(\mathbf{w}_{t,k}\hat{\mathbf{x}}_{f,k}^{+*}\right) = 0$, therefore Eqn.B.30 can be rewritten as

$$\mathbf{R}_{te,k+1}^{-} = \mathbf{F}_{t,k} E\left(\mathbf{x}_{t,k}\hat{\mathbf{x}}_{f,k}^{+*}\right)\mathbf{F}_{f,k}^{*} = \mathbf{F}_{t,k}\mathbf{R}_{te,k}^{+}\mathbf{F}_{f,k}^{*}. \tag{B.31}$$

- $\mathbf{R}_{ee,k}^{-}$

  Define:

$$\mathbf{R}_{ee,k+1}^{-} = E\left(\widehat{\mathbf{x}}_{f,k+1}^{-}\widehat{\mathbf{x}}_{f,k+1}^{-*}\right). \tag{B.32}$$

  Plugging Eqn.B.29 into Eqn. B.32 obtains

$$\mathbf{R}_{ee,k+1}^{-} = \mathbf{F}_{f,k} E\left(\hat{\mathbf{x}}_{f,k}^{+}\hat{\mathbf{x}}_{f,k}^{+*}\right)\mathbf{F}_{f,k}^{*} = \mathbf{F}_{f,k}\mathbf{R}_{ee,k}^{+}\mathbf{F}_{f,k}^{*}. \tag{B.33}$$

When measurement update stops, one can simply set

$$\begin{aligned}
\mathbf{R}_{ee,k+1}^{+} &= \mathbf{R}_{ee,k+1}^{-} \\
\mathbf{R}_{te,k+1}^{+} &= \mathbf{R}_{te,k+1}^{-}
\end{aligned}$$

and keep propagating.

Appendix C

U.S. CAT III Airports

The CAT III airports considered in this dissertation are listed in the following table. Contents are downloaded from http://www.faa.gov/Avr/afs/afs410/catbbs.htm.

Table of the U.S. CAT III Airports

Item No.	Airport Location	Position		Runway Heading (deg)
		Latitude (deg)	Longtitude (deg)	
1	Anchorage, AK	N61.2	W150	60
2	Atlanta, GA	N33.8	W84.2	80
3	Baltimore, MD	N39.2	W77.0	100
4	Bangor, ME	N44.8	W68.8	150
5	Boston,MA	N42.3	W71.3	40
6	Charlotte, NC	N35.2	W80.8	0
7	Chicago, IL	N42.0	W87.8	140
8	Covington, KY	N44.0	W84.5	0
9	Dallas/Fort Worth, TX	N32.7	W97.0	170
10	Dayton, OH	N32.6	W97.5	180
11	Denver, CO	N39.6	W84.2	60
12	Detroit, MI	N39.6	W105.0	340
13	Fairbanks, AK	N42.3	W83.0	30
14	Fort Worth, TX	N64.8	W147.5	10

Table of the U.S. CAT III Airports (Continued)

Item No.	Airport Location	Position		Runway Heading (deg)
		Latitude (deg)	Longtitude (deg)	
15	Houston, TX	N29.8	W95.2	260
16	Indianapolis, IN	N39.9	W86.25	50
17	Jackson, MS	N32.3	W90.1	150
18	Jacksonville, FL	N30.2	W82.2	70
19	Kansas City, MO	N39.0	W94.6	190
20	Los Angeles, CA	N33.9	W118.0	240
21	Memphis, TN	N35.0	W90.0	0
22	Milwaukee, WI	N42.7	W89.5	10
23	Nashville, TN	N36.2	W87.2	20
24	Newark, NJ	N40.8	W74.2	40
25	New Orleans, LA	N30.0	W90.0	10
26	New York, NY	N40.8	W74.0	40
27	Oakland, CA	N37.6	W122.0	290
28	Ontario, CA	N34.0	W117.0	260
29	Orlando, FL	N28.7	W81.6	350
30	Philadelphia, PA	N40.0	W75.0	90
31	Pittsburgh, PA	N40.4	W80.0	100
32	Portland, OR	N45.4	W122.7	100
33	Richmond, VA	N42.7	W77.5	340
34	Sacramento, CA	N38.3	W121.5	160
35	Salt Lake City, UT	N40.8	W112.3	160
36	San Francisco, CA	N37.5	W122.1	280
37	Seattle, WA	N47.5	W122.6	160
38	Spokane, WA	N47.5	W117.5	30
39	Tampa, FL	N27.7	W82.5	0
40	Washington, DC Dulles	N38.8	W77.0	10
41	Windsor Locks, CT	N42.1	W71	60

Bibliography

[AC120-28C] Federal Aviation Administration, Advisory Circular 120-28C: , *Criteria for Approval of Category III Landing Weather Minima*, Washington, D.C., 9 March 1984.

[Allan] David W. Allan and James A. Barnes, *A Modified "Allan Variance" with Increased Oscillator Characterization Ability*, Proc. 35th Ann. Freq. Control Symposium, USAERADCOM, Ft. Monmouth, NJ 07703, May 1981.

[Boeing] The Boeing Company, *777-200 Operations Manual*, The Boeing Company, 1994.

[Bose] S. C. Bose, *Integrated Navigation Systems (INS/GPS)*, Technalytics, 1996.

[Braasch] M. S. Braasch, *Multipath Effects*, contribution to The Global Positioning System: Theory and Applications, B.W. Parkinson and J.J. Spilker Jr., P. Axelrad, P. Enge, editors, AIAA Series, 1996.

[Britting] K. R. Britting, *Inertial Navigation Systems Analysis*, John Wiley, New York 1971.

[Brown] R. G. Brown, *Introduction to Random Signal Analysis and Kalman Filtering*, John Wiley, New York 1983.

[Cohen] C. Cohen, B. Pervan, H. S. Cobb, D. Lawrence, J. D. Powell, and B. Parkinson, *Precision Landing of Aircraft Using Integrity Beacons*, contribution to Global Positioning System: Theory and Applications, B. W. Parkinson and J. J. Spilker Jr., P. Axelrad, P. Enge, editors, AIAA Series, 1996.

[Cohen, a] C. Cohen, D. Lawrence, B. Pervan, S. Cobb, A. Barrows, D. Powell, B. Parkinson, V. Wullschleger, and S. Kalinowski, *Flight Test Results of Autocoupled Approaches Using GPS Integrity Beacons*, ION GPS-94, Salt Lake City, September 1994.

[Cohen, b] Clark E. Cohen, et al., *Autolanding A 737 Using GPS Integrity Beacons*, NAVIGATION, Vol. 42, No. 3, pp.467-486, Fall 1995.

[Cohen, c] Clark E. Cohen, et al., *Real-Time Flight Testing Using Integrity Beacons for GPS Category III Precision Landing*, NAVIGATION, Vol. 41, No. 2, Summer 1994.

[Dai] D. Dai, *WAAS Reference Station Multipath Envelope*, Project Report, Stanford University, 1997.

[Diesel] J. Diesel and J. R. Huddle, *Advantages of Autonomous Integrity Monitored Extrapolation for Precision Approach*, ION GPS-97, Kansas City, Missouri, September 1997.

[Doherty] P. H. Doherty, P. J. Gendron, R. Loh, and D. N. Anderson, *The Spatial and Temporal Variations in Ionospheric Range Delay*, ION GPS-97, pp231-240, Kansas City, Missouri, Sep 16-19, 1997.

[Eissfeler] B. Eissfeler and P. Spietz, *Basic Filter Concepts for the Integration of GPS and an Inertial Ring Laser Gyro Strapdown System*, Manuscripta Geodaetica, vol. 14, 1989, pp.166-182.

[Enge] Per Enge, *Local Area Augmentation of GPS for the Precision Approach of Aircraft*, Proceedings of the IEEE, January 1999.

[Enge, a] Per Enge, et al., *Wide Area Augmentation of the Global Positioning System*, Proceedings of the IEEE Vol. 84, No. 8, August 1996.

[Eykhoff] Pieter Eykhoff, *System Identification Parameter and State Estimation*, A Wiley-Interscience Publication, 1974.

[Gazit] R. Gazit, *Carrier Smoothing and Kalman Filter*, research report, 1996.

[Gebre-Egziabher] D. Gebre-Egziabher, J. D. Powell and P. Enge, *A DME Based Area Navigation System for GPS/WAAS Interference Mitigation In General Aviation Applications*, IEEE PLANS 2000, San Diego, CA, March 2000.

[Goad] C. C. Goad, *Optimal Filtering of Pseudoranges and Phases from Single-Frequency GPS Receivers*, NAVIGATION, Vol. 37, No. 3, pp249-262, Fall 1990.

[Green] G. B. Green, P. D. Massatt, and N. W. Thodus, *The GPS 21 Primary Satellite Constellation*, NAVIGATION, Vol. 36, No. 1, Spring 1989.

[Hatch] R. R. Hatch, *The Synergism of GPS Code and Carrier Measurements*, Proceedings of the Third International Geodetic Symposium on Satellite Doppler Positioning, Las Cruces, NM, February 1982.

[Hegarty] C. J. Hegarty, *Analytical Derivation of Maximum Tolerable In-Band Interference Levels for Aviation Applications of GNSS*, NAVIGATION, Vol. 44, No. 1, Spring 1997.

[Hsiao] T. Hsiao and C. Shively, *Availability of LAAS for CAT III Estimation vs. Detection*, MITRE Presentation, February 1998.

[Hundley] W. Hundley, S. Rowson, G. Courtney, V. Wullschleger, R. Velez, R. Benoist, and P. O'Donnel, *FAA-Wilcox Electric Category IIIb Feasibility Demonstration Program Flight Results*, ION GPS-95, Palm Springs, California, September 1995.

[Hwang] P. Y. C. Hwang, Kinematic GPS for Differential Positioning: Resolving Integer Ambiguity on the Fly, Navigation, Vol. 38, No. 1, Spring 1991.

[Johnson] M. Johnson and R. Erlandson, *GNSS Receiver Interference: Susceptibility and Civil Aviation Impact*, ION GPS-95, Palm Springs, CA, September 1995.

[Kailath] T. Kailath, *Linear Estimation*, EE378A Classnotes, Stanford University, January 1994.

[Kee] C. Kee, *Wide Area Differential GPS (WADGPS)*, Ph.D. Thesis, Stanford University, Aero/Astro Dept.,1993, p60.

[Kelly] R. J. Kelly and J. M. Davis, *Required Navigation Performance (RNP) for Precision Approach and Landing with GNSS Application*, NAVIGATION, Vol. 41, No. 1, Spring 1994.

[Klein] D. Klein, B. W. Parkinson, *The Use of Pseudo-Satellites for Improving GPS Performance*, NAVIGATION, Vol. 31, No. 4, Winter 1985.

[Klobuchar] J. A. Klobuchar, *Ionospheric Effects on GPS*, contribution to The Global Positioning System: Theory and Applications , B. W. Parkinson and J. J. Spilker Jr., P. Axelrad, P. Enge, editors, AIAA Series, 1996.

[Klobuchar, a] J. A. Klobuchar, *Ionospheric Time-Delay Algorithm for Single-Frequency GPS Users*, IEEE Transactions on Aerospace and Electronic Systems, Vol. AES-23, No. 3, May 1987.

[Lawrence] D. Lawrence, S. Cobb, B. Pervan, G. Opshaug, P. Enge, J. D. Powell, and B. W. Parkinson, *Performance Evaluation of On-Airport Local Area Augmentation System Architectures*, ION GPS-96, Kansas City, MO., September 1996.

[Lawrence, a] D. G. Lawrence, *Aircraft Landing Using GPS: Development and Evaluation of a Real Time System for Kinematic Positioning Using the Global Positioning System*, Ph.D. dissertation, Stanford University, Aero/Astro Dept., September 1996.

[Levine] S. A. Levine and A, Gelb, *Effect of Deflection of the Vertical on the Performance of a Terrestrial Inertial Navigation System*, Journal of Spacecraft, Vol. 6, No. 9, September 1969.

[Liu] F. Liu, T. Murphy and T. A. Skidmore, *LAAS Signal-in-Space integrity Monitoring Description and Verification Plan*, in Proceedings of the ION-GPS 97, Kansas City, Missouri, September 16-19, 1997.

[Meyer] J. Meyer-Hilburg and H. Harder, *Application of INS/GPS Systems Integration to Increase Performance of Automatic Landing Systems*, ION GPS-95, Palm Springs, California, September 1995.

[Nash] R. A. Nash, J. A. D'Appolito, K. J. Roy, *Error Analysis of Hybrid Aircraft Inertial Navigation Systems*, AIAA Guidance and Control Conference, Stanford, CA, August 1972.

[Nisner] P. Nisner and J. Owen, *Practical Measurements of Radio Frequency Interference to GPS Receivers and an Assessment of Interference Levels by Flight Trials in the European Regions*, ION GPS-95, Palm Springs, CA, September 1995.

[Paielli] R. Paielli, R. Bach, B McNally, R. Simmons, D. Warner, T. Forsyth, G. Kanning, C. Ahtye, D. Kaufmann, J. Walton, *Carrier Phase Differential GPS Integrated With an Inertial Navigation System: Flight Test Evaluation with Auto-Coupled Precision Landing Guidance*, ION National Technical Meeting-95, Anaheim, CA, January 1995.

[Pandit] S. M. Pandit and S. M. Wu, *Time Series and System Analysis with Applications*, John Wiley and Sons, 1983.

[Parkinson] B. W. Parkinson, *Introduction and Heritage of NAVSTAE*, contribution to The Global Positioning System: Theory and Applications , B. W. Parkinson and J. J. Spilker Jr., P. Axelrad, P. Enge, editors, AIAA Series, 1996.

[Parkinson, a] B. W. Parkinson and P. K. Enge, *Differential GPS*, table 9, p26, contribution to The Global Positioning System: Theory and Applications, B. W. Parkinson and J. J. Spilker Jr., P. Axelrad, P. Enge, editors, AIAA Series, 1996.

[Pervan] B. Pervan, C. Cohen, and B. W. Parkinson, *Autonomous Integrity Monitoring for Precision Approach Using DGPS and a Ground-Based Pseudolite*, ION GPS-93, Salt Lake City, September 1993.

[Pervan, a] B. Pervan, D. Lawrence, K. Gromov, G. Opshaug, J. Christie, P. Y. Ko, A. Mitelman, S. Pullen, P. Enge, and B. Parkinson, *Flight Test Evaluation of a*

Prototype Local Area Augmentation System Architecture, ION GPS-97, Kansas City, MO, September 1997.

[Pervan, b] B. Pervan, *Navigation Integrity for Aircraft Precision Landing Using the Global Positioning System*, Ph.D. Thesis, Stanford University, Aero/Astro Dept., March 1996.

[Phlong] W. S. Phlong and B. D. Elrod, *Availability Characteristics of GPS and Augmentation Alternatives*, NAVIGATION, Vol. 40, No.4, Winter 1993-94.

[Savage] P. G. Savage, *Strapdown Sensors*, AGARD-LS-95.

[Schnaufer] B. A. Schnaufer and G. A. McGraw, *WAAS Receiver Carrier Tracking Loop and Data Demodulation Performance in the Presence of Wideband Interference*, NAVIGATION, Vol. 44, No. 1, Spring 1997.

[Sherman] Sherman G. Francisco, *GPS Operational Control Segment*, contribution to Global Positioning System: Theory and Applications, B. W. Parkinson and J. J. Spilker Jr., P. Axelrad, P. Enge, editors, AIAA Series, 1996.

[Spilker] J. J. Spilker, Jr., *GPS Signal Structure and Performance Characteristics*, NAVIGATION, Vol. I 1980.

[SPS] SPS, *Global Positioning System Standard Positioning Service Signal Specification (Second Edition)*, June 2, 1995.

[Stieler] B. Stieler and H. Winter, *Gyroscopic Instruments and Their Application to Flight Testing,*, AGARD-AG-160-VOL.15, September 1982.

[Swider] R. Swider, R. Braff, J. Warburton and V. Wullschleger, *Local Area Augmentation System (LAAS) Update,* from FAA, 1997.

[Tsai] Y. J. Tsai, *Wide Area Differential Operation of the Global Positioning System : Ephemeris and Clock Algorithms*, Ph.D. dissertation, Stanford University, Aero/Astro Dept., 1999.

[van Dierendonck] A. J. Van Dierendonck and M. B. McGraw, *Relationship Between Allan Variances and Kalman Filter Parameters*, N85-29238.

[van Graas] F. van Graas, D. Diggle, M. Uijt, V. Wullschleger, R. Velez, D. Lamb, M. Dimeo, G. Kuehl, and R. Hilb, *FAA/Ohio University/United Parcel Service DGPS Autoland Flight Test Demonstration*, ION GPS-95, Palm Springs, CA, September 1995.

[van Graas, a] F. van Graas, D. Diggle, M. Uijt, T. Skidmore, M. DiBenedetto, V. Wullschleger, R. Velez, *Ohio University/FAA Flight Test Demonstration Results of the Local Area Augmentation System (LAAS)*, ION GPS-97, Kansas City, Missouri, September 1997.

[Vieweg] G. Schänzer, S. Vieweg, *Inflight Calibration of Inertial Sensors with the Help of Global Navigation Satellite Systems*, Symposium Gyro Technology 1992, Stuttgart, Germany.

[WAASMOPS] RTCA, *Minimum Operational Performance Standards (MOPS) for WAAS Avionics*, RTCA, 1997.

[Walter] T. Walter, C. Kee, Y. C. Chao, Y. J. Tsai, et al., *Flight Trials of the Wide Area Augmentation System (WAAS)*, in Proceedings of the ION-GPS 94, Salt Lake City, UT, September 22-24, 1994, pp. 1537-46.

[Wanninger] L. Wanninger, G. Seeber, and M. A. Campos, *Limitations of GPS in Central and South America Due to The Ionosphere*, presented at the Int. Conference "Cartography - Geodesy", Maracaibo, Venezuela, Nov 24 - Dec 4, 1992.

[Warnant] R. Warnant, Influence of the Ionospheric Refraction on the Repeatability of Distances Computed by GPS, ION GPS-97, Kansas City, MO, 1997.

[Wei] M. Wei and K. P. Schwarz, *A Strapdown Inertial Algorithm Using an Earth-Fixed Cartesian Frame*, NAVIGATION, Vol. 37, No. 2, Summer 1990.

[Wells] David Wells, *Guide to GPS Positioning*, Canadian GPS Associates, p9.2.